Thesis Title

A DISSERTATION
SUBMITTED TO THE FACULTY OF THE GRADUATE SCHOOL
OF THE UNIVERSITY OF MINNESOTA
BY

Andy Jarod Julin

IN PARTIAL FULFILLMENT OF THE REQUIREMENTS
FOR THE DEGREE OF
DOCTOR OF PHILOSOPHY

Prof. Ron Poling

March, 2017

Acknowledgements

This is where the Acknowledgements go!

Dedication

This is where the Dedications go!

Abstract

We measure the production cross section of $e^+e^- \to \psi(3770) \to D\overline{D}$ around the nominal mass of the $\psi(3770)$. The $(69.80 \pm 0.03)\,\mathrm{pb}^{-1}$ of e^+e^- annihilation data used were collected in 2010 over an energy range of $3.735\,\mathrm{GeV}$ to $3.870\,\mathrm{GeV}$. Since the previously observed $e^+e^- \to D\overline{D}$ cross section cannot be explained by a single Breit-Wigner shape, this study investigates if interference effects from non-resonant $D\overline{D}$ production can account for the $D\overline{D}$ cross section shape.

Contents

List of Tables

List of Figures

Chapter 1

Introduction

Chapter 2

Theoretical Background

2.1 Standard Model

Developed throughout the 1960s and 1970s, the Standard Model provides the most complete description of observable matter in the universe to date. It is a classification of all confirmed subatomic particles currently known, and predicts the most accurate results of any scientific theory ever measured. Each of the electromagnetic, weak, and strong fundamental forces are well described by this formulation. These three are described by an $SU(3) \times SU(2) \times U(1)$ group, where the $SU(3)$ corresponds to the strong force, the $SU(2)$ corresponds to the weak force, and the $U(1)$ corresponds to the electromagnetic force. The remaining fundamental force, gravity, is negligible on the scale of the masses of fundamental particles, and will be ignored in the discussions that follow.

2.1.1 Electromagnetic Force

The electromagnetic force is responsible for attracting and repelling objects, most notably binding together electrons and protons to form atomic structures. The most prominent theory of electromagnetic interactions is known as Quantum Electrodynamics (QED). The mediator of this force is the photon, a massless vector boson. As there is only a single mediator, and a single conserved quantity (electric charge), the formulation of QED is relatively simple compared to the other forces. Still, the predictions it makes show astounding consistency with experiment, such as correctly calculating the anomalous magnetic dipole moment of the electron to more than 10 significant figures.

Much of this success is due to QED being expandable through perturbation theory, where corrections are applied in terms of higher order factors of the coupling constant, α. This is possible due to a relatively small coupling constant ($\alpha \approx 1/137$), as the terms are convergent below very high orders of α.

2.1.2 Weak Force

The weak force is responsible for the decays of various particles into other forms. This is distinct from the electromagnetic and strong interactions, where the constituent particles cannot change their types (or flavors). The mediators of this force are the W and Z, which are massive vector bosons. Not only are each of these masses non-zero, they are considerably heavy particles at $80.4\,\text{GeV}$ and $90.2\,\text{GeV}$, respectively [1]. These large masses not only inhibit the interaction distance of the weak force, but also minimize the interaction strength (which is inversely proportion to mass). Furthermore, this mass excess also leads to much slower interaction times, further reducing the effects of the weak force in comparison to the strong and electromagnetic forces.

In addition to transforming particle flavor, the weak force is also unique in its violation of various symmetries. The first discovery of symmetry violation came in 1957, when Wu and others [3] discovered the weak force did not behave identically under parity (P) transformations (i.e., mirror reflection). To account for this, a new theory conserving a compound symmetry was proposed. This combined charge conjugation (C), the swapping of particles with their antiparticles, with parity to form CP parity. However, in 1964, evidence of CP violation was also discovered by Cronin and Fitch [4]. The resolution to this symmetry conservation involves yet a third symmetry, time reversal (T), in which time is replaced with its negative ($t \rightarrow -t$). While the weak force violates these symmetries individually, the application of all three (CPT) is conserved across all known processes, and is known as the CPT Theorem.

At higher energy scales, the electromagnetic and weak forces unify into the electroweak force. In this theory, there are initially four massless gauge bosons mediating the interactions. As a result of the Higgs mechanism, the initial gauge symmetry is broken at lower energies, and three of these bosons acquire a mass. These three bosons are the $W^{\pm}$ and Z, while the remaining massless boson is the γ. The energies scales required for this unification were only present in the early universe. Before this, it is

also believed there was an epoch of even higher energy, in which the electroweak force merged with the strong force.

2.1.3   Strong Force

The strong force is responsible for binding together particles known as hadrons. The most prominent theory of strong interactions is known as Quantum Chromodynamics (QCD). Like the electromagnetic force, the mediator of the strong force is also a massless vector boson, the gluon. However, while massless particles typically correspond to an infinite interaction range, the strong potential becomes very large at higher separations. This prevents particles which interact through the strong force from existing as isolated entities, and is known as confinement. The typical interaction range is on the order of the proton radius, around 10^{-15} m. QCD provides additional challenges, however, as the coupling constant is not small ($\alpha_S \gtrsim 1$). This excludes the use of perturbation theory for most cases, as the higher order terms do not converge.

Strong interactions are associated with a corresponding conserved quantity known as color charge. There are three colors associated with this charge, red (r), green (g), and blue (b). For anti-particles, there are oppositely charged values ($\bar{r}, \bar{g}$, and $\bar{b}$). In order for hadrons to be formed, the total color values of the constituents must be colorless. This means the total sum must involve all three colors (rgb or $\bar{r}\bar{g}\bar{b}$) or pairs of opposite colors ($r\bar{r}, g\bar{g}$, or $b\bar{b}$). However, these individual colors are not observable in nature. This effectively triples the number of possible particle combinations, due to combinatorics.

Unlike the photon, which is neutral to the electromagnetic force, the gluon also carries color charge. There are eight possible color combinations which a gluon may possess, which are typically expressed using the Gell-Mann representation of $SU(3)$. With this basis, each gluon is linearly independent, and no combination of gluons can be used to form a color singlet state. This inclusion of color by the force carrier makes QCD significantly more complex than QED. In fact, carrying color charge means gluons can also interact with each other directly, leading to certain theoretical states such as glueballs.

2.1.4   Elementary Particles

There are two primary groups contained in the Standard Model, fermions and bosons. This division is based off the Spin Statistics theorem, where fermions have half-integer spins, and bosons have integer values. Because of these values, the Pauli Exclusion principle restricts fermions from occupying the same spatial state, and thus there are restrictions on their spatial density. Bosons, however, do not have this restriction, and can have any number occupying the same space. Thus, fermions are typically more tangible matter (such as electrons), while bosons typically represent the forces interacting between them (such as photons).
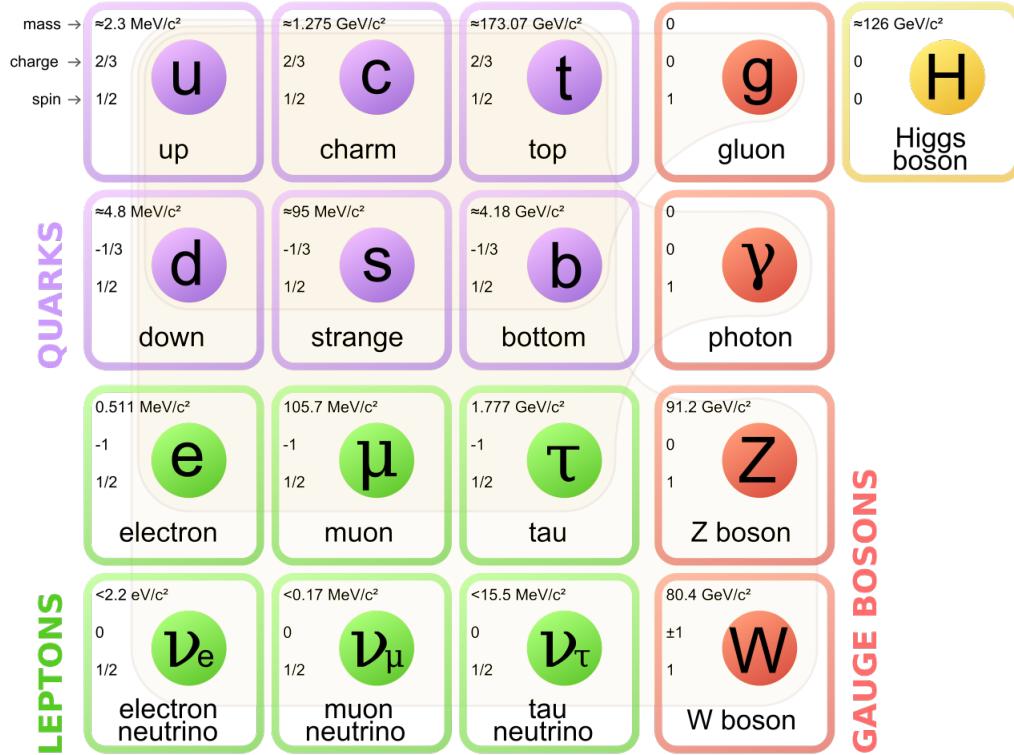
Figure 2.1: The standard model of particle physics.
It is comprised of two main groups: fermions, which includes the quarks and leptons, and bosons, which includes the gauge bosons and the Higgs boson. Image reproduced courtesy of [2].

Fermions

The fermions are divided by their interaction types into two major groups, quarks (q) and leptons (l). Each of these groups contains six particles with their corresponding antiparticle. These can also be categorized into three generations, which aligns particles with the same electric charges, but greatly differing masses. As an example, the up (u), charm (c), and top (t) quarks all have an electric charge of $+2/3$ (in terms of the electron charge, e), but t is approximately five orders of magnitude more massive than u. For the quarks and fermions in Figure 2.1, rows indicate particles with the same electric charge, while columns represent each generation of particles.

Although all fermions interact both electromagnetically and weakly, only the quarks interact strongly. Because of confinement, quarks cannot exist as isolated particles, and are only found in nature as groups of particles called hadrons. The most common types of hadrons exist as quark-antiquark pairs, known as mesons, or as groups of three quarks (or antiquarks), known as baryons. There are, however, indications of more exotic combinations of quarks, such as tetra- ($qq\bar{q}\bar{q}$) or penta-quark ($qqqq\bar{q}$) states seen by recent experiments [5, 6, 7].

While the negatively charged quarks (d, s, and b) are labeled as definite states, each of the quarks are actually mixed states. Through weak interactions, each of these quarks can transform into other states. The probabilities for these transformations are given by the Cabibbo-Kobayashi-Maskawa (CKM) Matrix [8], shown in Figure 2.2. From the experimentally measured values [1], is it evident the matrix is nearly diagonal. It is also clear that correlations are strongest for the earlier generations, as off-diagonal terms are larger for the u quark, but very small for the t quark. Additionally, though the convention splits the negatively charged quarks into mixed states (leaving the positively charged quarks fixed), this choice has no physical basis. The reverse choice of having mixed positively charged quarks is also valid.

$$
\begin{bmatrix} |V_{ud}| & |V_{us}| & |V_{ub}| \\ |V_{cd}| & |V_{cs}| & |V_{cb}| \\ |V_{td}| & |V_{ts}| & |V_{tb}| \end{bmatrix} = \begin{bmatrix} 0.97427 \pm 0.00014 & 0.22536 \pm 0.00061 & 0.00355 \pm 0.00015 \\ 0.22522 \pm 0.00061 & 0.97343 \pm 0.00015 & 0.0414 \pm 0.0012 \\ 0.00886^{+0.00033}_{-0.00032} & 0.0405^{+0.0011}_{-0.0012} & 0.99914 \pm 0.00005 \end{bmatrix}
$$

Figure 2.2: The Cabibbo-Kobayashi-Maskawa (CKM) Matrix.

The values of the CKM matrix are typically parameterized using three Euler angles

$(\theta_{12}, \theta_{23}, \theta_{13})$ and a CP-violating phase parameter (δ_{13}), where the indices represent the three generations of quarks. This formulation allows the matrix to be cast in the "standard" parametrization, shown in Figure 2.3. The form with three separated matrices clearly shows the connections between each generation of quarks. Namely, the third shows the original formulation in terms of a single rotation, the Cabbibo angle (θ_{12}), before the discovery of the charm quark. This procedure was known as the Glashow-Iliopoulos-Maiani (GIM) mechanism [[9].

$$
\begin{bmatrix} 1 & 0 & 0 \\ 0 & c_{23} & s_{23} \\ 0 & -s_{23} & c_{23} \end{bmatrix} \begin{bmatrix} c_{13} & 0 & s_{13}e^{-i\delta_{13}} \\ 0 & 1 & 0 \\ -s_{13}e^{i\delta_{13}} & 0 & c_{13} \end{bmatrix} \begin{bmatrix} c_{12} & s_{12} & 0 \\ -s_{12} & c_{12} & 0 \\ 0 & 0 & 1 \end{bmatrix}
$$
$$
= \begin{bmatrix} c_{12}c_{13} & s_{12}c_{13} & s_{13}e^{-i\delta_{13}} \\ -s_{12}c_{23} - c_{12}s_{23}s_{13}e^{i\delta_{13}} & c_{12}c_{23} - s_{12}s_{23}s_{13}e^{i\delta_{13}} & s_{23}c_{13} \\ s_{12}s_{23} - c_{12}c_{23}s_{13}e^{i\delta_{13}} & -c_{12}s_{23} - s_{12}c_{23}s_{13}e^{i\delta_{13}} & c_{23}c_{13} \end{bmatrix}
$$

Figure 2.3: The standard form of the Cabibbo-Kobayashi-Maskawa (CKM) Matrix. The parameterization is in terms of three angles $(\theta_{12}, \theta_{23}, \theta_{13})$ and a phase angle (δ_{13}). Here, $c_{ij} = \cos\theta_{ij}$ and $s_{ij} = \sin\theta_{ij}$.

The leptons are also divided into two major distinctions based on their charge. The electron (e^-), muon (μ^-), and tau (τ^-) are all negatively charged particles. With the exception of mass, the interaction properties of each flavor is very similar. However, the three flavors themselves are treated as separate conserved quantities. There is also a neutral particle, a neutrino (ν), corresponding to each one $(\nu_e, \nu_\mu, \nu_\tau)$. These are very small mass $(< 1\,\text{eV})$ particles with extremely low interactions.

The original formulation of the Standard Model assumed these neutrinos to be massless particles. However, this was violated by the discovery of neutrino oscillations, where transformations occur between neutrino flavor states due to differences in their masses. Additionally, the flavor states, ν_e, ν_μ, and ν_τ, are not the states observed in nature. Rather, the states with definite mass, labeled ν_1, ν_2, and ν_3, are linear combinations of the three flavor states. This can be expressed in a rotation of bases called the Pontecorvo-Maki-Nakagawa-Sakata (PMNS) matrix [10, 11]. Its formulation is analogous to the CKM Matrix for quarks.

Bosons

For each of the three forces included in the Standard Model, there are accompanying gauge bosons. These include the photon (γ) for electromagnetic force, the $W^{\pm}$ and Z for the weak force, and the gluon (g) for the strong force. Each of the gauge bosons are a spin-1 vector boson, which means there are three available polarization states (-1, 0, +1). However, since the photon and gluon are both massive, gauge invariance requires these to have transverse polarizations. This means the spin-0 state is eliminated, and there are only two polarization states for each. There is also the Higgs boson (H), which unifies the electromagnetic and weak forces, and whose interactions with other particles is responsible for their mass. This is the only known fundamental spin-0 particle, which means it has only one polarization state.

Even with the amazing success of the Standard Model, the theory is not complete. Along with neutrino oscillations, other effects, such as dark matter or dark energy, remain major hindrances in constructing a unified theory. Such a theory must also include gravity, but there remain significant difficulties in explaining its effects through a quantum field theory. There also remains no conclusive explanation for various constants, such as the masses of each fundamental particle. Still, the Standard Model remains the most precise description of the universe to date, and continues to provide the basis for future experimental and theoretical work.

2.2   Charmonium

The majority of this analysis focuses on a specific group of particles known as Charmonium. These particles are resonances formed by a $c\bar{c}$ pair, and can be treated analogous to the hydrogen atom. Namely, there is a spectrum of various excited states in the Charmonium region, just as with the emission lines of hydrogen. The three states which are focused on include the $J/\psi, \psi'$, and ψ''. The ' and '' marks indicate these are the first and second excited states of the J/ψ, respectively. More commonly, the ψ' is denoted $\psi(3686)$ and the ψ'' is denoted $\psi(3770)$. The numbers in parentheses represent the mass of the particle in MeV.

An alternative label for these states uses the quantum numbers for each particle. This is written in the form $N^{2s+1}L_J$, where N refers to the principal quantum number,

s refers to the total spin angular momentum of the particle, L refers to the orbital angular momentum, and J refers to the total angular momentum. Here, the values of L are in spectroscopic notation, where $L = 1, 2, 3, 4 \ldots$ is denoted $S, P, D, F \ldots$, and higher values follow alphabetically (excluding J). As each of these states are comprised of two spin-$\frac{1}{2}$ particles, the value of s in this case can only be 0 (opposite) or 1 (aligned). With this, the $J/\psi, \psi(3686)$, and $\psi(3770)$ can be denoted 1^3S_1, 2^3S_1, and 1^3D_1. The values of n and L are used for the alternate notation of $\psi(2S)$ representing $\psi(3686)$. However, the notation of $\psi(1D)$ is not often used for $\psi(3770)$. This is due to evidence of mixing in $\psi(3770)$ between the 2^3S_1 and 1^3D_1 states that suggests more complicated underlying interactions [12, 13].

In fact, while the comparisons from this model work well for states less massive than the $\psi(3770)$, the predictions made above this often break down. This is likely based on the energy required to produce open-charm D mesons, such as $D^+(c\bar{u})$ and $D^0(c\bar{d})$. The $D\overline{D}$ threshold (twice the mass of the D^0) is just above the $\psi(2S)$ mass, and just slightly below the $\psi(3770)$ mass. Therefore, the decay products of the two particles end up being drastically different, even while the available phase space is relatively similar. Example Feynman diagrams for these two particles can be seen in Figures 2.4 and 2.5.
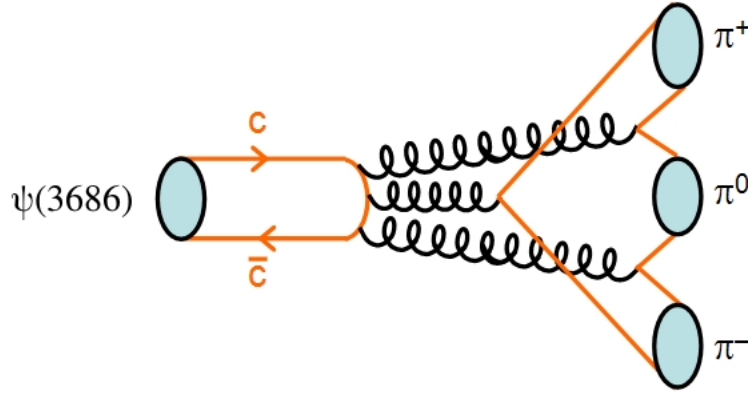
Figure 2.4: An example Feynman diagram for the decay of $\psi(3686)$.
Without sufficient energy to produce D mesons, the closed-charm decays of $\psi(3686)$ are suppressed by the need for three gluons.
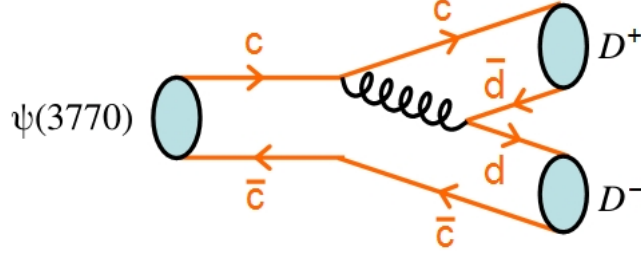
Figure 2.5: An example Feynman diagram for the decay of $\psi(3770)$. With sufficient energy to produce D mesons, the open-charm decays of $\psi(3770)$ are allowed to proceed, greatly increasing the total decay width.

The difference is also clearly seen in the total decay widths, where the most recent experimental averages [1] are $\Gamma^{\psi(2S)} = 286\,\mathrm{keV}$ and $\Gamma^{\psi(3770)} = 27.5\,\mathrm{MeV}$. An explanation for this discrepancy was proposed independently in the 1960s by Okubo [14], Zweig [15], and Iizuka [16], and is named the OZI rule. This states that any Feynman Diagram where the initial and final particles are separated at some point by only gluons represents a suppressed decay. Such behavior requires that the momentum transfer from the initial particles must occur entirely through these gluons. Because of the decreasing strength of the strong interaction with higher momentum transfer, the rate of these decays is thereby inhibited. This is further compounded by the need for three gluons in such an interaction, as one gluon could not conserve color charge, and two could not converse C-parity. Once above the $D\overline{D}$ threshold, the allowed open-charm decays dominate, and the total width is massively increased. This dominance points to a high branching fraction expected for decays of the type $\psi(3770) \to D\overline{D}$.

2.3 Derivation of $\sigma_{\psi(3770) \to D\overline{D}}$

The production rate for a pair of D mesons coming from $\psi(3770)$ at a given center-of-mass energy can be calculated following an approach of Kuraev and Fadin [17] applied by the KEDR collaboration [18]. This method also corrects for Initial State Radiation

(ISR), affecting particles accelerated in a collider, and is given by the following:

$$\sigma_{D\overline{D}}^{RC}(W) = \int z_{D\overline{D}}(W\sqrt{1-x})\,\sigma_{D\overline{D}}(W\sqrt{1-x})\,\mathcal{F}(x, W^2)\,dx. \tag{2.1}$$

Here, W is the given center-of-mass energy, x is an approximation for the fraction of radiated energy, and $\mathcal{F}(x, W^2)$ is the probability of losing this energy from ISR:

$$\mathcal{F}(x, W^2) = \beta\,x^{\beta-1}\left[1 + \frac{\alpha}{\pi}\left(\frac{\pi^2}{3} - \frac{1}{2}\right) + \frac{3}{4}\beta + \beta^2\left(\frac{37}{96} - \frac{\pi^2}{12} - \frac{L}{72}\right)\right] = \beta\,x^{\beta-1}F(W^2),$$

$$\beta = \frac{2\alpha}{\pi}(L-1), \qquad L = \log\left(\frac{W^2}{m_e^2}\right). \tag{2.2}$$

The factor $z_{D\overline{D}}$ includes the expected Coulomb interaction between the mesons in of the charged mode (D^+D^-),

$$z_{D^+D^-} = \frac{\pi\alpha/\beta_{D^+}}{1 - \exp(-\pi\alpha/\beta_{D^+})} \times \theta(W - 2m_{D^+}), \tag{2.3}$$

but only accounts for the $D\overline{D}$ energy threshold in the neutral mode $(D^0\overline{D^0})$,

$$z_{D^0\overline{D^0}} = \theta(W - 2m_{D^0}). \tag{2.4}$$

The theta function imposes the step in the cross section at the production threshold.

The integral in Eq. 2.1 can be simplified by taking advantage of the relatively constant values of $z_{D\overline{D}}$ and $\sigma_{D\overline{D}}$ over sufficiently small intervals. By splitting the full W range into such intervals and integrating over each, this becomes

$$\int \mathcal{F}(x, W^2)\,dx \approx \sum_{n=0}^{N} F(W^2)\int_{\frac{n}{N}}^{\frac{n+1}{N}} \beta x^{\beta-1}\,dx = \sum_{n}^{N} F(W^2)\left[x_{\text{upper}}^{\beta} - x_{\text{lower}}^{\beta}\right]. \tag{2.5}$$

The upper, lower, and mid-point values are given by

$$x_i = \left[1 - \left(\frac{2m_D}{W}\right)^2\right]\left(\frac{n_i}{N}\right), \qquad n_i : \begin{cases} n_{\text{lower}} &= n \\ n_{\text{mid}} &= n + \frac{1}{2} \\ n_{\text{upper}} &= n + 1 \end{cases}. \tag{2.6}$$

The bracketed expression in Eq. 2.6 represents the maximum value of x determined by the theta functions of Eqs. 2.3 and 2.4. To maintain sufficient precision with this interval approximation, the value of $N = 1024$ is used. Combining this with the other factors in Eq. 2.1, the cross section including the effect of ISR becomes

$$\sigma_{D\overline{D}}^{RC}(W) = \sum_{n=0}^{N} z_{D\overline{D}}(W') \, \sigma_{D\overline{D}}(W') \, F(W^2) \left[1 - \left(\frac{2m_D}{W} \right)^2 \right]^{\beta} \left[\frac{[(n+1)^{\beta} - n^{\beta}]}{N^{\beta}} \right], \quad (2.7)$$

where $W' = W\sqrt{1 - x_{\mathrm{mid}}}$. The Born level $D\overline{D}$ cross section is given theoretically by

$$\sigma_{D\overline{D}} = \frac{\pi \alpha^2}{3W^2} \beta_D^3 |F_D(W)|^2, \qquad \beta_D = \sqrt{1 - \frac{4m_D^2}{W^2}}. \quad (2.8)$$

Here, β_D is the velocity of the D meson in the center-of-mass system. The form factor F_D represents the contribution of each individual resonant (R) component and the total non-resonant (NR) component. Each resonant piece is parametrized with a phase angle relative to the non-resonant contribution:

$$F_D(W) = F_D^{\mathrm{NR}}(W) + \sum_r F_D^{R_r}(W) \, e^{i\phi_r}. \quad (2.9)$$

Each resonant contribution to the form factor is modeled by a Breit-Wigner amplitude,

$$F_D^R(W) = \frac{6 \, W \sqrt{(\Gamma_{ee}/\alpha^2)(\Gamma_{D\overline{D}}(W)/\beta_D^3)}}{M^2 - W^2 - iM\Gamma(W)}, \quad (2.10)$$

where Γ_{ee} is the electron partial width, and $\Gamma(W)$ represents the total width of the resonance with mass M:

$$\Gamma(W) = \left(\frac{M}{W} \right) \left[\frac{z_{D\overline{D}}(W) \, d_{D\overline{D}}(W)}{z_{D^0\overline{D^0}}(M) \, d_{D^0\overline{D^0}}(M) + z_{D^+D^-}(M) \, d_{D^+D^-}(M)} \right] \Gamma(M). \quad (2.11)$$

The value of $\Gamma(M)$ represents the total width at the nominal mass of the resonance. The factors $d_{D^+D^-}$ and $d_{D^0\overline{D^0}}$ are the Blatt-Weisskopf damping factors [19] for a vector resonance:

$$d_{D\overline{D}} = \frac{\rho_{D\overline{D}}^3}{\rho_{D\overline{D}}^2 + 1}, \qquad \rho_{D\overline{D}} = q_D R_0 = \left(\frac{\beta_D W}{2} \right) R_0. \quad (2.12)$$

Here, q_D is the D momentum in the center-of-mass frame, while R_0 represents the radius of the parent particle. The $D\overline{D}$ partial width listed in Eq. 2.10 is simply the total width rescaled according to $\mathcal{B}_{nD\overline{D}}$, the sum of all non-$D\overline{D}$ decay modes of $\psi(3770)$:

$$\Gamma_{D\overline{D}}(W) = \Gamma(W) \times (1 - \mathcal{B}_{nD\overline{D}}). \tag{2.13}$$

However, as a simplifying assumption, we use $\mathcal{B}_{nD\overline{D}} = 0$ throughout the analysis.

Chapter 3

Detector and Related Systems

All data used for this analysis were collected at the third Beijing Spectrometer (BESIII), located in Beijing, China, at the Institute of High Energy Physics (IHEP) campus. This detector records e^+e^- collision events provided by the second Beijing Electron-Positron Collider (BEPCII). The target energies for these collisions focus on τ^- and c production in the range of about $2.0\,\text{GeV}$ to $4.6\,\text{GeV}$. Both of these machines are upgrades from previous versions built on the same sites. The first BEPC and BES were originally constructed in 1989, while the upgrade to BESII occurred in 1996. These two sites were closed in 2004 to prepare for the upgrades to the current systems.

In 2009, BEPCII and BESIII resumed operation with the goal of utilizing greatly increased luminosity. For example, instead of the single-bunch electron collisions of BEPC, the new design utilized multiple bunch collisions. This creates many groups of electrons and positrons which are tightly packed in each ring during run time. BEPCII also utilizes a dual-storage ring for the electrons and positrons, compared to the single-ring available at BEPC. The improvements provide BEPCII with a design luminosity of $10^{33}\,\text{cm}^{-2}\,\text{s}^{-1}$, two orders of magnitude larger than the previous installation. This luminosity is optimized for energies near the $\psi(3770)$ resonance, as BESIII conducts many precision measurements and rare decay searches around this region. A detailed description of the BESIII detector can be found in Ref. [20].

3.1 BEPCII Accelerator

The setup for collisions in BEPCII begins with bombarding a fixed target with electrons. This generates high energy photons which interact with the target material to form e^+e^- pairs. The positrons from these pairs are then separated magnetically. Using a linear accelerator, these positrons are then injected into the desired storage ring until they reach the desired beam current. As electrons do not need to be created in this manner, they are instead directly accelerated and injected into the opposite storage ring. These injections occur at a rate of $50\,\mathrm{mA/\,min}$ for positrons and $200\,\mathrm{mA/\,min}$ for electrons.

To achieve the necessary high beam currents, many bunches of electrons and positrons are packed into the evacuated rings. During operation, each ring contains 93 bunches spaced $8\,\mathrm{ns}$ ($2.4\,\mathrm{m}$) with a length of $1.5\,\mathrm{cm}$. These provide a beam current of $0.91\,\mathrm{A}$ while operating in collision mode. At the interaction point, each beam is focused using super-conducting quadrupole magnets to compress the beam size to about $5.7\,\mu\mathrm{m}$ vertically, while the horizontal beam size is about $380\,\mu\mathrm{m}$. For collisions, each beam is also angled towards the center of the storage rings with an angle of $11\,\mathrm{mrad}$. This crossing angle provides better resolution for determining particle momenta in the detector.

For a normal run, collisions continue occurring until the instantaneous luminosity falls below useful levels. While this is typically depleted due to the collisions between the e^+e^- particles, other unwanted interactions (such as those with beam-gas in the storage rings) also reduce these currents. When this happens, BEPCII can replenish the beams using top-off injections. This allows the collider to continue utilizing the remaining particles within the storage rings without dumping the beams completely. Recycling these leftover electrons and positrons saves considerable time, and allows for more efficient data taking.

3.2 BESIII Detector

Centered around the interaction point of BEPCII, the BESIII detector records information about the particles produced by the resulting collisions. Each collision occurs within the beam-pipe of the detector, which is used to minimize multiple-scatterings and secondary interactions. Its inner and outer radii are $31.5\,\mathrm{mm}$ and $57.0\,\mathrm{mm}$, and is pressurized to $5 \times 10^{-10}\,\mathrm{Torr}$. Surrounding the entire apparatus is a uniform, $1.0\,\mathrm{T}$

magnetic field provided by a super-conducting solenoid with a mean radius of $1.482\,\mathrm{m}$ and a length of $3.53\,\mathrm{m}$. The field points in the z-direction, which is along the direction of the e^+ beam. The x-direction points towards the center of the storage rings, while the y-direction is vertically upwards. This magnetic field is used to provide better precision on momenta measurements. An appropriate field strength curves the tracks of charged particles sufficiently to interact with more of the tracking volume, while minimizing those which curl too much to reach all layers of the detector.
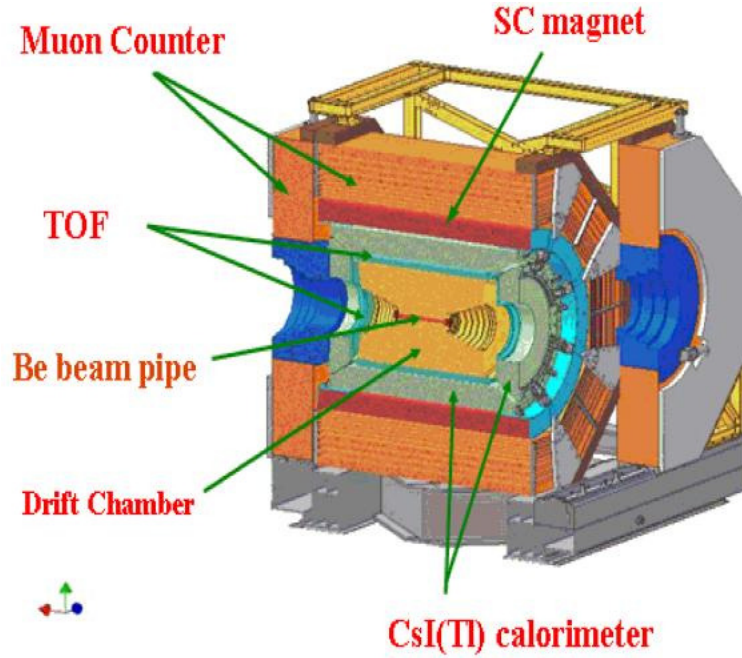
Figure 3.1: A schematic of the BESIII detector.
There are four main layers surrounding the beam-pipe: the Main Drift Chamber (MDC), the Time-of-Flight (ToF), the Electromagnetic Calorimeter (EMC), and the Muon Chamber (MUC). Each of these are surrounded by a $1\,\mathrm{T}$ magnetic field.

The BESIII detector, shown in Figure 3.1, is split into four main layers which analyze different aspects for identifying particles. Starting from the most interior, these layers are the Multi-Layer Drift Chamber (MDC), the Time-of-Flight System (ToF), the Electromagnetic Calorimeter (EMC), and the Muon Identifier (MUC). Using the information provided by each layer, the tracks seen in the detector are given a particle hypothesis for their most likely candidate. Only charged particles stable enough to

sufficiently traverse the detector are identifiable in this way. The candidate particles identified at BESIII are electrons (e), muons (μ), pions (π), kaons (K), and protons (p). Short-lived particles, such as D^0 and D^+, must be reconstructed from their decays into these constituents, as well as neutral shower energy from photons (γ).

3.2.1 Multi-Layer Drift Chamber

The purpose of the Multi-Layer Drift Chamber is to determine the momenta and trajectories of charged particles. Because of the magnetic field encasing the detector, charged particles will travel in helical trajectories. The direction of travel is used to determine their charge, while the curvature of the track is used to determine their momenta.

The MDC is comprised of many layers of tungsten and sense wires to detect the ionization of particles which pass through its gas-filled volume. The tungsten wires create a constant electric field which causes ionized electrons to drift towards the sense wires. This field is tuned to a strength which minimizes secondary ionization. Conversely, the electric field near each of the sense wires is much larger than the rest of the volume. This forces an avalanche of secondary ionizations in order to create a current in the sense wires. The amount of energy deposited by this process is proportional to the original ionization levels. Tracing the path of energy depositions over time allows for the reconstruction of each charged particle trajectory.

The main design of the MDC focuses on a multi-layer assortment of cells corresponding to the individual sense wires. The inner and outer radii of the MDC are 59 mm and 810 mm, respectively. There are 43 layers of sense wires which cover 93% of the 4π solid angle in the detector. This provides position resolutions of 130 µm and 2 mm in the $r - \phi$ plane and beam direction, respectively, for each cell. The uncertainty in these measurements is dominated by electron diffusion and the readout time uncertainty for the electronics. For the transverse momentum, the resolution is about 0.5 % for tracks with momenta of 1 GeV, with uncertainties coming mainly from wire position measurements, and multiple scatterings from other material in the MDC.

The gas used for ionization is a mixture of 60% helium (He) and 40% methane (C_3H_8). Helium, being chemically inert, will not interact with the ionized electrons used to measure the position and deposited energy. Its low atomic number, and thus,

long radiation length, also minimizes multiple scatterings which degrade the momentum resolution. Methane, with extra rotational and vibrational degrees of freedom not accessible to Helium, quenches the ionization energy. Without this effect, the ionization energy would not be diffused, and would degrade the measurements of deposited energy.

In addition to trajectory, the MDC also measures the rate of energy loss over distance for a particle traveling through a material [21],

$$-\frac{dE}{dx} = 4\pi N \frac{z^2 e^4}{m_e \beta^2} \left[\log\left(\frac{2m_e \beta^2}{I(1-\beta^2)}\right) - \beta^2 \right], \tag{3.1}$$

where N is the electron number density of the material, z is the charge of the particle in terms of e, the charge of the electron, m_e is the mass of the electron, β is the velocity of the particle, and I is the mean excitation potential for electrons in the material being traversed. The resolution of dE/dx is about 6 % for particles incident 90° to the beam-axis. The uncertainty is due to fluctuations in the number of primary ionizations along the flight path, fluctuations in the avalanche process, as well as from edge effects on each cell.
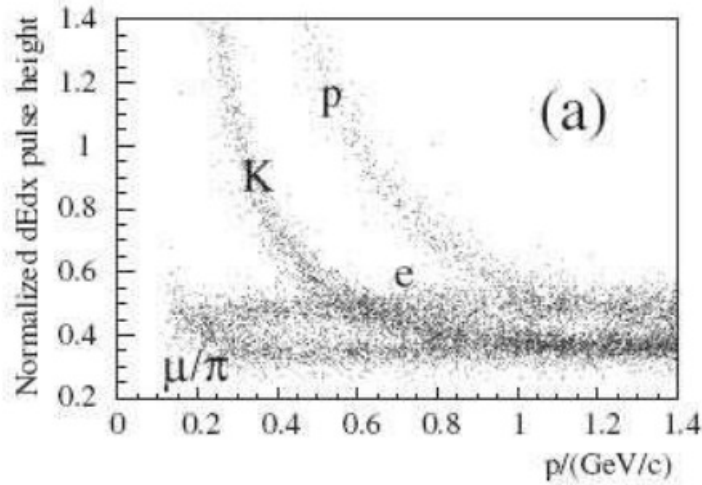
Figure 3.2: MDC energy deposition for various particles as a function of momenta. Distinction between K and π tracks is easier for low momenta, but becomes very difficult for higher values.

The energy deposition provides a method of distinguishing particle candidates, as

this quantity depends on the velocity of the particle. An example of this behavior for multiple types of particles can be seen in Figure 3.2. To identify a particle from the various candidates, the measured energy deposition (dE/dx_{meas}) is compared against the expected value (dE/dx_{exp}) of each hit used to reconstruct the particle's trajectory (i):

$$\chi^2 = \sum_i \chi_i^2 = \left(\frac{dE/dx_{\mathrm{meas}} - dE/dx_{\mathrm{exp}}}{\sigma}\right)_i^2, \tag{3.2}$$

where σ represents the uncertainty on the measured energy deposition. This process provides a separation of 3σ between K and π tracks with momenta up to $770\,\mathrm{MeV}$.

3.2.2 Time-of-Flight System

The purpose of the Time-of-Flight System is to determine the velocity of charged particles. This is useful for distinguishing particles with similar momenta, but different masses, as shown in Figure 3.3. It uses information provided by the MDC to determine the probability for each charged track to match the possible particle hypotheses. Namely, this includes the measured momentum, the expected time interval based on its trajectory, and the mass for each particle hypothesis. This process provides a separation of 3σ between K and π tracks with momenta up to $900\,\mathrm{MeV}$.
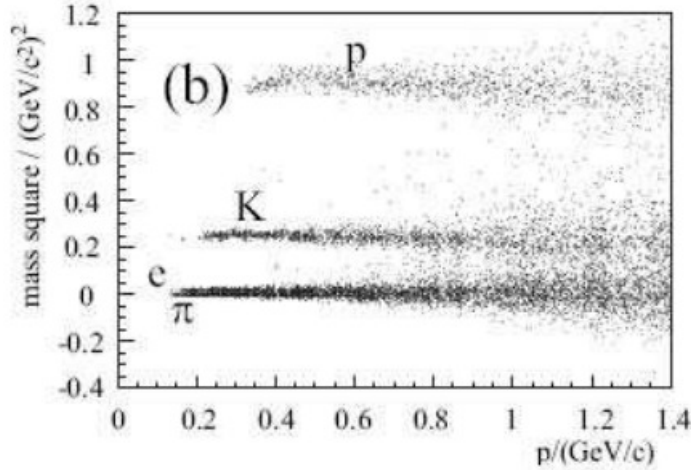
Figure 3.3: ToF measurements for various particles as a function of momenta. Distinction between K and π tracks is very easy for low momenta, but becomes more difficult for higher values.

The ToF is comprised of two bands of staggered plastic scintillators attached to photomultiplier tubes (PMTs). These two bands, located at $0.81\,\mathrm{m}$ and $0.86\,\mathrm{m}$ from the beam-pipe, measure a time difference used to determine the speed of each charged particle. The resolution is about $100\,\mathrm{ps}$, and is largely limited by the scintillation light rise time, as well as fluctuations associated with the PMTs. The layer is split into two regions, barrel and endcap, which cover the ranges $|\cos\theta| < 0.82$ and $0.85 < |\cos\theta| < 0.95$, respectively. The former is dual-layer with each containing 88 scintillators of $5\,\mathrm{cm}$ thickness arranged in a trapezoidal cross section, while the latter contains two single layers of 48 fan-shaped scintillators. Between the two are support structures for the MDC as well as other service lines.

3.2.3   Electromagnetic Calorimeter

The purpose of the Electromagnetic Calorimeter is to determine the energy deposited by photons. Since each of the candidates identified in the detector will be relativistic, they are minimum ionizing particles. This causes each to deposit a relatively constant value of energy, independent of the measured momenta. However, electrons, with their extremely small mass, will deposit significant amounts of energy due to Bremsstrahlung radiation. This provides a clear distinction in the detector between electron and muon tracks above $200\,\mathrm{MeV}$, as seen in Figure 3.4. Energy measurements from the EMC are also useful for identifying neutral particles which decay only to photons, such as π^0.
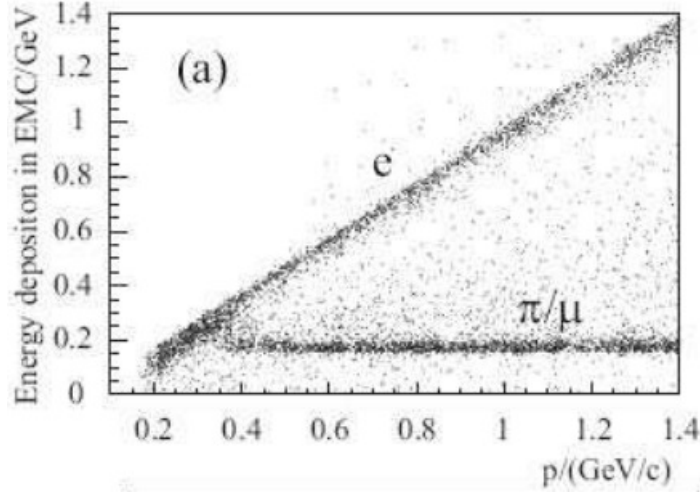
Figure 3.4: EMC energy deposition for various particles as a function of momenta. As the mass of e^- is so small, it deposits virtually all of its energy in the EMC. Both μ^- and π are generally minimum ionizing particles in this momenta range, and their similar masses make them difficult to distinguish from the EMC measurements alone.

The EMC is comprised of tellurium-doped cesium iodide (CsI(Tl)) crystals with square front faces attached to a photodiode. Each of the 6240 crystals are 5.2 cm long on the square edges and 28 cm (15 radiation lengths) deep. To prevent photons from aligning with the gaps between each crystal, each one is offset with a tilt of 1.5° in the ϕ-direction and 1.5° to 3° in the θ-direction. These crystals provide an energy resolution (σ/E) of 2.5% at 1 GeV and 4% down to 100 MeV. This is limited by energy not deposited over the length of the crystal, the areas between crystals, and by non-uniform light production. Additionally, only measurements of energy above 20 MeV are considered, as below this value is indistinguishable from noise. The position resolution is $\sigma = 0.6\,\mathrm{cm}/\sqrt{E\,[\mathrm{GeV}]}$, and is primarily limited by the crystal segmentation. The layer has an inner radius of 94 cm and a total weight of approximately 24 tons. It covers the regions $|\cos\theta| < 0.83$ (barrel) and $0.85 < |\cos\theta| < 0.93$ (endcap), but does not well capture the region between the two.

3.2.4 Muon Identifier

The purpose of the Muon Identifier is to determine the likelihood of a charged particle being a muon. Since electrons are significantly lower mass, they deposit virtually all of

their remaining energy in the EMC. Additionally, since muons do not interact strongly, they will penetrate notably further than will pions, kaons, or protons. This provides a clear indication of a muon when a particle traverses much of the MUC layer. However, due to the magnetic field, only muons with $p > 0.4\,\mathrm{GeV}$ will be able to traverse deep enough to be identifiable.

The MUC is comprised of resistive plate counters (RPC) which are interspersed between the steel plates of the super-conducting solenoid. Each of the steel layers generally increase in thickness working outwards from the center: $3\,\mathrm{cm}$, $3\,\mathrm{cm}$, $3\,\mathrm{cm}$, $4\,\mathrm{cm}$, $4\,\mathrm{cm}$, $8\,\mathrm{cm}$, $8\,\mathrm{cm}$, $8\,\mathrm{cm}$, and $15\,\mathrm{cm}$. Like the other layers, the MUC is also split into a barrel and an endcap region. The barrel has nine RPC layers of $4\,\mathrm{cm}$ thickness. In the endcap, the first RPC layer is after the first steel layer, leaving only eight RPC layers. Each of these layers have RPC strips oriented along only one direction. For the barrel, the z (ϕ) orientation is read out for only the odd (even) layers. Conversely, the endcap only reads out the x (y) orientation in the odd (even) layers.

3.3 Triggering Systems

In order to maintain a high efficiency for selecting physics events, many backgrounds must be filtered out. At BESIII, this is done through a triggering system with two-tiers: a hardware trigger (L1) and a software event filter (L3). This process is illustrated in Figure 3.5. The filtered background events are primarily from beam-related sources, such as beam-gas or beam-wall interactions, and occur at a rate of about $13\,\mathrm{MHz}$. To assist with this process, collimators and masks are used to prevent lost electrons from interacting with the detector. However, there are also other sources of backgrounds, such as cosmic rays, which occur at a rate of about $1.5\,\mathrm{kHz}$. The total backgrounds must be suppressed to a rate which does not overwhelm the recording of events by the readout systems. This rate is roughly $2\,\mathrm{kHz}$ at the J/ψ peak, and $600\,\mathrm{Hz}$ for the $\psi(2S)$ when running near peak luminosity. For Bhabha events ($e^+e^- \rightarrow e^+e^-$), which are used for calibration and luminosity measurements, this rate is $800\,\mathrm{Hz}$ within detector acceptance.
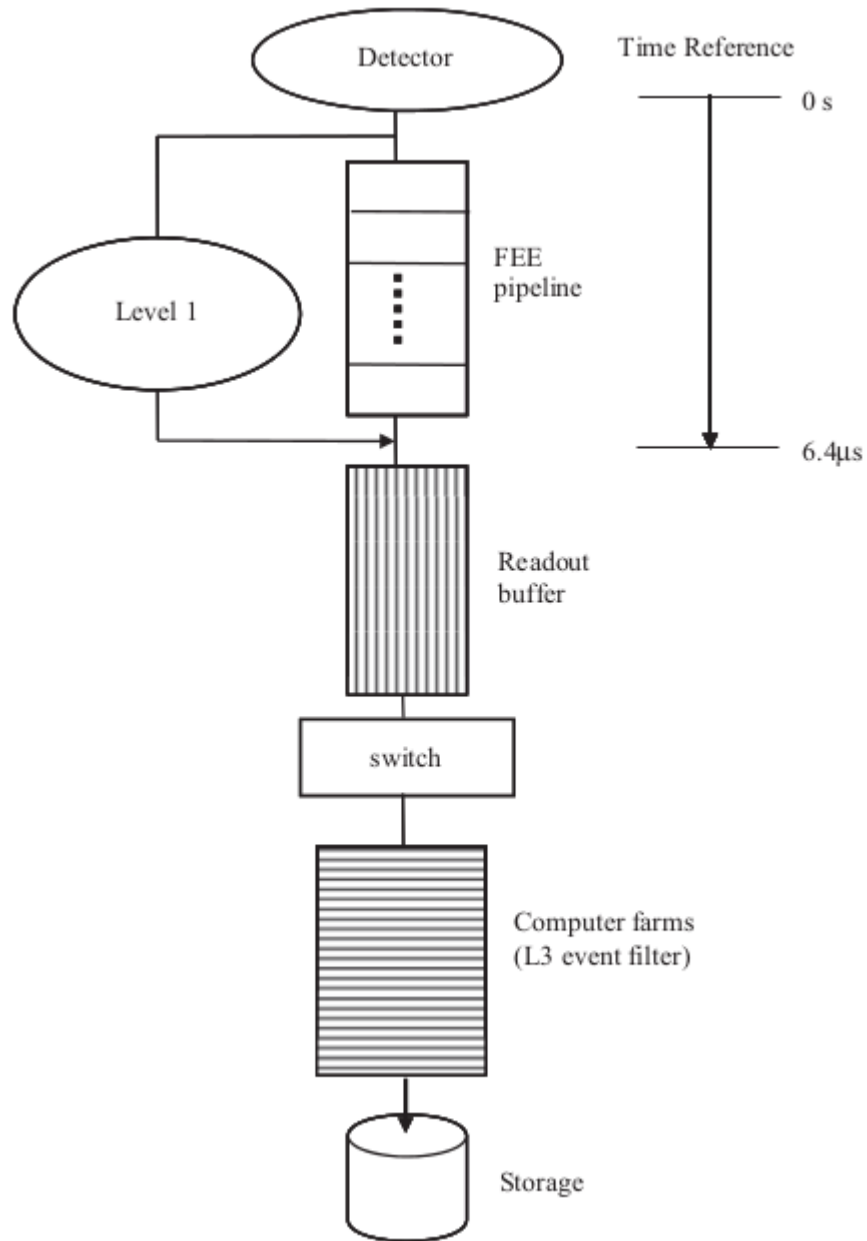
Figure 3.5: Triggering systems for event filtering at BESIII.
To prevent overloading the event recording system, non-physics background events must be disregarded in the detection system. This processing uses simple read-out information from each of the layer of the detector to quickly and efficiently determine whether or not events should be further considered for analysis.

The first step (L1) reads out every clock cycle (24 ns) at a rate of 41.65 MHz. It uses information from the MDC, ToF, and EMC collectively to reduce the rates of beam-related backgrounds to 1.84 kHz and cosmic rays to about 200 Hz. However, L1 has a maximum rate of about 4 kHz. Because of this, when the buffer holding the subdetector data is around 80 % full, L1 triggering is halted until the buffer drops below 10 % full.

From the MDC, L1 gathers information about each charged track. The main parameter examined is the number of superlayers a track passed through. Here, a superlayer is the collection of wires at the same radial distance away from the center of the detector. Tracks are defined as 'short' if they deposit energy in segments of superlayers 3-5, or 'long' for superlayers 3-5 and 10. To ensure a sufficient momentum to reach the outer superlayers while originating at the interaction point, a minimum transverse momentum cut is applied to each track. This cut is 90 MeV and 120 MeV for short and long tracks, respectively. In addition to the numbers of short and long tracks for an event, the information about back-to-back tracks is also used.

From the ToF, L1 gathers information about the number of hits in the barrel and end-cap regions. It also examines the number of back-to-back hits in each of the two regions. Here, 'back-to-back' is defined as having hits within a range of 9 counters on the opposite side of the detector.

From the EMC, L1 gathers information about the clustering of energies around a local maximum-energy crystal. This includes the number of isolated clusters, as well as the information about back-to-back hits in the barrel and end-cap. Additionally, the balance of energy in the ϕ-direction (barrel) and in the z-direction (endcap) is also used.

The subdetector information gathered during L1 is then passed off to an online computer farm (L3) where the event is assembled. This step reduces backgrounds from a rate of about 2 kHz to about 1 kHz. Combined with the signal rate at the J/ψ peak (2 kHz), this corresponds to a total event rate of 3 kHz, or a tape write speed of 40 MB/s.

Chapter 4

Analysis Software

4.1 BESIII Offline Software System

Reconstructing and processing event data gathered by the BESIII detector is done using the BESIII Offline Software System (BOSS) [22]. This is an analysis software distribution written using the C++ language and running primarily on the Scientific Linux CERN operating system [23]. There are five main parts to BOSS: framework, simulation, reconstruction, calibration, and analysis.

4.1.1 Framework

The framework is built on the Gaudi software architecture [24], which provides a standard interface and utilities for things such as event simulation, data processing, and physics analysis. The software is managed using the Configuration Management Tool [25], which provides a method for creating packages, handling package dependencies, and producing executables from source code. There are three main filetypes for data stored by the framework: raw data (`.raw`), reconstructed data (`.rec`), and Data-Summary-Tape (`.dst`). The latter two of these file types are derived from the ROOT [26] format (`.root`) for easy management and usage in various analyses.

4.1.2 Simulation

There are four main parts to the simulation process: event generation, detector description, particle tracking, and detector response. Event generation is primarily handled by the Monte Carlo (MC) generators KKMC, BesEvtGen, and Babayaga, which are described below. To model its geometry and materials, a unique description of the detector has been created using a format based on XML. This allows both simulation and reconstruction packages to appropriately model the behavior of events within the specific environment of BESIII. For particle tracking, interactions with detector materials are handled by GEANT4 [27]. Lastly, detector responses are modeled by the so-called 'digitization code'. This takes into account each detector component, as well as readout electronics, and realistic situations such as noise or dead channels. There is also a simulation of the triggering system implemented.

KKMC

Originally developed for the LEP and SLC colliders, KKMC [28] is a generator used to model electroweak interactions. Namely, the processes generated are of the form $e^+e^- \to f\bar{f} + (n)\gamma$, where $f = \{\mu, \tau, u, d, s, c, b\}$, and $(n)\gamma$ represents any number of additional photons. These are modeled taking into account second-order sub-leading corrections, as well as initial-state radiation (ISR), and interference between initial- and final-state radiation (FSR). The effects of beam energy spread, typically on the order of $1\,\mathrm{MeV}$ near the $\psi(3770)$, can also be included.

After generation, the $f\bar{f}$ pair is decayed by models depending on the fermions involved. The TAUOLA library [29] is used to decay $\tau^-\tau^+$ pairs, and takes into account spin-polarization effects. The PYTHIA model [30] is used to hadronize final-state $q\bar{q}$ continuum production using the parton shower model. For resonances like the $\psi(3770)$, the only action performed by KKMC is the generation of ISR. After this, the virtual photon produced is handed off to BesEvtGen.

BesEvtGen

Originally developed for the CLEO and BaBar collaborations, EvtGen [31] is another widely used generator. It is the basis for BesEvtGen [32], which incorporates many

different decay models into a single utility. Over 30 exclusive decay models are available in BesEvtGen, as well as the capability to incorporate user-created models.

The simulation process occurs sequentially using dynamic information from decay amplitude probabilities and forward / backward spin-density matrices. From this, final state radiation is handled by the PHOTOS model [33]. To generate unknown decays of charmonium resonances, the LundCharm model [34] is used, while other unknown hadronic decays are handled by PYTHIA. For radiative processes, such as radiative return to J/ψ or $\psi(2S)$, the VECTORISR model [35] is used. This occurs when one particle in the initial e^+e^- pair radiates a photon of high enough energy that only lower mass resonances can be produced from the reduced center-of-mass energy. When the radiation is less intense, the $\psi(3770)$ resonance is directly produced through the combination of KKMC and BesEvtGen.

Babayaga

Production of QED processes is done using the Babayaga generator [36]. This includes $e^+e^- \to \{e^+e^-, \mu^+\mu^-, \gamma\gamma\}$. The results are of very high precision, with an estimated theoretical accuracy of $0.1\,\%$. It also matches exact next-leading-order corrections from the parton shower algorithm. The high precision also helps determine the efficiencies and acceptances required to precisely measure the integrated luminosities of each data sample.

4.1.3 Reconstruction

Reconstruction primarily involves information about specific types of particles from each of the four main detector layers. These sources of information are as follows:

- a charged track finding algorithm and a Kalman-filter-based track-fitter

- a particle identifying algorithm based on dE/dx and time-of-flight measurements

- a shower- and cluster-finding algorithm for EMC energy and position

- a muon track finding algorithm

Further descriptions about each of these processes can be found in Sec. 4.2. Additionally, algorithms for determining the corresponding beam bunch crossing, as well as for secondary vertex and track refitting, are also utilized.

4.1.4 Calibration

To maintain consistent production and analysis of datasets, a centralized source of run-dependent information is maintained by BOSS. This includes algorithms which determine the calibration constants for each sub-detector, as well as a centralized database to store the results. Each of the calibration outputs are stored in a ROOT file along with other details such as the beam energy, luminosity, magnetic field information, trigger conditions, and hardware / software versions. While all of this information is stored by a central MySQL [37] server at IHEP, databases for other institutions in BESIII regularly synchronize with this server to create a mirrored copy of these values.

4.2 Detector Simulation

The following sections detail the simulation, calibration, and reconstruction processes for each layer. Each of these relies on a geometry description created using GEANT4.

4.2.1 Multi-Layer Drift Chamber

Simulating events in the MDC accounts for the axial layers and endplates, the stereo layers, and the stereo cells. The simulation also heavily relies on the calibration parameters to determine things such as wire efficiency and resolution as a function of drift distance for each wire, noise in each layer, and other misalignment issues.

Calibration of the MDC uses $J/\psi \to \mu^+\mu^-$ events to determine position and dE/dx measurements. Using J/ψ events allows for quickly obtaining sufficient statistics due to the very large production cross section at the peak. The information determined includes constants such as $x - t$ relations, timing, alignment, and absolute wire efficiency. Each of these values are stored in the database for each run. Additionally, turning off the magnetic field could allow for precise determination of wire positions.

Reconstructing MDC events starts by finding axial track segments using raw hits. Each of these are found by searching for pre-calculated patterns. Next, these segments

are linked to circular tracks by a circular fit using the least-squares method. Stereo segments are then added using an iterative helix fit. Lastly, additional hits which were possibly missed from the initial reconstruction are applied using a Kalman-filter process. This process also examines the tracks over multiple particle hypotheses. The reconstruction is remarkably efficient, with over $98\,\%$ of tracks with $p_T > 150\,\text{MeV}$ being reconstructed, even amidst high backgrounds. From this, the charge, momentum, and trajectory can be determined for each track.

In addition to tracking, the MDC also analyzes dE/dx for each particle. This calculates the energy deposition of each track as it passes through the chamber, and corrects the measured charge amplitudes to determine a probability for each particle hypothesis. Corrections applied account for things such as multiple scatterings, magnetic deflections, and ionization. This likelihood from dE/dx is used in conjunction with information from the ToF to identify the actual type of particle for each track.

4.2.2 Time-of-Flight System

Simulating events in the ToF accounts for the scintillator, wrapping materials, and photomultiplier tubes (PMTs). The process converts the energy deposited in the scintillator into photons, then propagates the shape of a photon pulse (rather than individual photons) to the PMTs in order to generate an electronic signal. A discriminator is applied to each pulse to determine the analog-to-digital conversion (ADC) and time-to-digital conversion (TDC) outputs. The algorithm is tested using the results of beam tests, however, subsequently gathered data sets require updated tuning. A full simulation tracing each optical photon can also be used for further details on the timing measurement.

Calibration of the ToF also uses J/ψ decays to leptons to determine both timing and energy measurements. The information determined includes effective velocity, attenuation length, and muon energy loss. The status and performance of the ToF are also regularly monitored by a laser-fiberoptics pulsing system.

Reconstructing ToF events starts by using tracks with trajectories extrapolated from the MDC. Each track is then matched with a particular ToF module; either the two layers of the barrel, or the single-layer endcap. The travel time for each hypothesis is then calculated using a weighted average of results from PMTs at both ends of the scintillator. Corrections are also applied to account for aspects like the effective light

velocity in the scintillator and the light attenuation length. Measurements of dE/dx are obtained for both charged and neutral particles, and are added back into the EMC in order to improve the shower energy resolution.

4.2.3 Electromagnetic Calorimeter

Simulating events in the EMC accounts for the crystals, casing, silicon photodiodes, preamplifier boxes, cables, and the support system. For each of the crystals and photodiodes, hit information is recorded, and the deposited energy is summed. From this, photon statistics are computed, and the resulting photodiode response is converted into electronic signals. To obtain the waveform in the time domain, an inverse Laplace transform is applied. Then, a sampling and peak searching process is simulated to yield energy and time information. For each bin, Gaussian-type electronic noise is added, and the background is produced by summing over the waveforms.

Calibration of the EMC uses Bhabha electrons with $E > 1.55 \, \text{GeV}$ for the high energy response, and $\pi^0 \to \gamma\gamma$ decays for the low energy response. The responses for individual crystals must be analyzed separately, due to their potential intrinsic variations. As a result, they are monitored frequently by a LED light pulser, and periodically recalibrated. Corrections due to temperature variations can also be applied.

Reconstructing EMC events starts by converting the ADC value of each crystal into energy based on the calibration constants. After this, clusters in both the barrel and endcaps are formed by analyzing local maximum energy deposits, called seeds. A clustering algorithm then relates hits around these seeds and sums the values for a particular shower. The positions of each shower is then calculated using energy-weighted first moments. If multiple seeds are found in one cluster, a splitting algorithm is invoked to split the cluster into multiple showers. Additionally, matching energy deposits from the ToF are also added back into the total shower energy. This improves the energy resolution, particularly for low energy photons.

4.2.4 Muon Identifier

Simulating events in the MUC accounts for forming each RPC, creating sets of strips to form each read-out plane, combining each of these with aluminum boxes to form a

muon counter module, and placing the modules alongside iron slabs. The digitization from the read-out planes is selected to fire based off the distance away of each track. Noise is simulated using Poisson distributions initially determined from measurements made during the construction of the chamber, and updated with the taking of actual data.

Calibration of the MUC analyzes RPC detection efficiencies over a function of area. The cluster size and noise levels are also studied.

Reconstructing MUC events starts by searching for collected hits in each of the barrel and endcap orientations. The two collections are then combined with reconstructed tracks from the MDC. Since low momentum muons may cause only a few layers to fire, a subsequent search is performed over unused hits based on the extrapolated trajectories of MDC tracks. The reconstruction process primarily analyzes the depth of the track in the MUC, the maximum number of hits in the layers fired by a track, and the matching between a MDC track with the MUC stand-alone track. These parameters, along with the track momentum and MDC exit angle, are input into an Artificial Neural Network in order to distinguish between hadron and muon tracks. The distinction process is quite effective, generally removing $\sim$96 % of pions and keeping around $\sim$90 % of muons.

4.3 D-Tagging

From the decay of the $\psi(3770)$, the most commonly produced particles are $D^0\overline{D^0}$ or D^+D^- pairs. Since the $D\overline{D}$ pairs produced are two-body decays, the energy available to each D is half of the center-of-mass energy (in the center-of-mass reference frame). Each of these D mesons then quickly decays to certain sets of particles. Reconstructing one of these decays requires assembling the right combination of such particles. From energy and momentum conservation, the total 4-momentum of the constituents must match the total energy of the D meson.

This reconstruction technique is known as 'D-Tagging', and was pioneered by the MARK-III collaboration [38, 39]. For our analysis, the particles analyzed in the detector include $\pi^\pm, K^\pm, \pi^0$, and K_S^0, and the decay modes used are shown in Table 4.1. There are three D^0 modes and six D^+ modes, where charge conjugation (converting all particles to their anti-particles) is implied throughout the analysis. The modes used are chosen for

their effectiveness of reconstruction in the detector; they generally have higher branching fractions and minimize multiplicity (the number of tracks used). Additionally, for the neutral modes, the doubly-Cabbibo suppressed decays (DCSD), such as $D^0 \to K^+ \pi^-$, are also included by this procedure.

(0) $D^0 \to K^- \pi^+$	(200) $D^+ \to K^- \pi^+ \pi^+$	(203) $D^+ \to K^0_S \pi^+ \pi^0$
(1) $D^0 \to K^- \pi^+ \pi^0$	(201) $D^+ \to K^- \pi^+ \pi^+ \pi^0$	(204) $D^+ \to K^0_S \pi^+ \pi^+ \pi^-$
(3) $D^0 \to K^- \pi^+ \pi^+ \pi^-$	(202) $D^+ \to K^0_S \pi^+$	(205) $D^+ \to K^+ K^- \pi^+$

Table 4.1: The reconstructed D-tag modes used in this analysis.

This process occurs for each event and searches over each decay mode for each charm (i.e., both D^+ and D^-). The combinations chosen for reconstruction are those with the smallest energy difference from the expected value. More than one D combination can be extracted from a given event, as long as it satisfies all other requirements (see Section 4.3.1). While this may sound like it overestimates the number of actual D particles found, the process is also used to calculate reconstruction efficiency, thereby cancelling out this effect.

4.3.1 Selection Cuts

Before being considered as potential reconstruction candidates, each track in the detector must also pass other cuts specific to its identified particle type. The following describes the necessary criteria required for the particles in the decay modes we are using.

$\pi^{\pm}/K^{\pm}$ Selection

Each of the reconstructed charged tracks must pass vertex cuts in both the transverse $(x - y)$ and beam (z) directions relative to the interaction point. This requires tracks originate sufficiently close to the interaction point to ensure they are not other backgrounds, such as cosmic rays, or other tracks which have decayed in flight. There is also a cut on the angle measured within the MDC (θ) to ensure the track has not disappeared down the beam-line (where detection cannot occur). Lastly, from the particle identification process, the probability of being a pion (kaon) must be more likely than being a kaon (pion). The values for each of these requirements can be found in Table 4.2.

Vertex (xy)	$V_{xy} < 1\,\text{cm}$
Vertex (z)	$|Vz| < 10\,\text{cm}$
MDC Angle	$|\cos\theta| < 0.93$
Pion Probability	$P(\pi) > 0, \quad P(\pi) > P(K)$
Kaon Probability	$P(K) > 0, \quad P(K) > P(\pi)$

Table 4.2: The required cuts to identify charged tracks as $\pi^{\pm}$ or $K^{\pm}$.

γ Selection

To distinguish photon energy from noise, each shower in the EMC is required to have a certain amount of deposited energy. These cuts are different for the barrel ($|\cos\theta| < 0.80$) and endcap ($0.84 < |\cos\theta| < 0.92$) regions. Each photon must also pass a TDC timing cut to ensure they are consistent with actual physics events, and not originating at other times. The values for each of these requirements can be found in Table 4.3.

Minimum Energy (Barrel)	$E_{\text{EMC}} > 25\,\text{MeV}$	($|\cos\theta| < 0.80$)
Minimum Energy (Endcap)	$E_{\text{EMC}} > 50\,\text{MeV}$	($0.84 < |\cos\theta| < 0.92$)
TDC Timing	$(0 \leq t \leq 14) \times 50\,\text{ns}$	

Table 4.3: The required cuts to identify neutral showers as a γ.

π^0 Selection

Reconstructing π^0 mesons involves finding $\gamma\gamma$ pairs, as this is its most dominant decay ($\sim 99\,\%$). Each of the γ showers used must pass the cuts described above. Additionally, at least one photon in the pair must be found in the barrel region. Each of the two photons are then kinematically fit to compare with the invariant mass of the π^0, and must also pass a proper fit cut. The resulting momentum from this fit is used for reconstructing D-tag candidates. The values used for each of these requirements are shown in Table 4.4.

Nominal Mass	$115\,\text{MeV} < m_{\pi^0} < 150\,\text{MeV}$
Fit Quality	$\chi^2 < 200$, Converged

Table 4.4: The required cuts to reconstruct $\gamma\gamma$ pairs as a π^0.

K_S^0 **Selection**

Reconstructing K_S^0 mesons involves finding $\pi^+\pi^-$ pairs, as this is its most common decay ($\sim$70 %). While $\pi^0\pi^0$ pairs are also a substantial decay mode ($\sim$30 %), these are not considered for reconstruction due to the increased difficulty of finding correct 4γ sets. To account for the K_S^0 decaying in flight, each of the charged pions considered are not subjected to the vertex or probability cuts in Table 4.2. Instead, the two found pions are kinematically constrained to a common vertex. The results must pass a nominal mass cut ($\sim$3 σ) and a proper fit cut to be deemed a K_S^0. From this, the resulting momentum from the vertex fit is used for reconstructing D-tag candidates. The values used for each of these requirements are shown in Table 4.5.

Nominal Mass	$487\,\mathrm{MeV} < m_{K_S^0} < 511\,\mathrm{MeV}$
Fit Quality	$\chi^2 < 100$, Converged

Table 4.5: The required cuts to reconstruct $\pi^+\pi^-$ pairs as a K_S^0.

Cosmic Ray and Lepton Veto

Lastly, when reconstructing the mode $D^0 \to K^-\pi^+$, an additional veto is used. Since the mode has only two charged tracks, it is common to misidentify particles which come from cosmic ray and two-lepton backgrounds. To prevent this, cuts on the timing difference between the tracks, as well as on the particle identification process, are enacted. The values used for each of these requirements are shown in Table 4.6.

Timing (TDC)	$|t_1 - t_2| < 5 \times 50\,\mathrm{ns}$
Particle Identification	$(\chi^2_{e^-} + \chi^2_{e^+}) - (\chi^2_{K^-} + \chi^2_{\pi^+}) > 10$

Table 4.6: Cuts to prevent cosmic ray and lepton backgrounds in $D^0 \to K^-\pi^+$.

4.3.2 Reconstruction

After each of the constituent particles are identified, a reconstructed D candidate can be characterized by two main properties:

$$\Delta E = |E_{\mathrm{beam}} - E_{\mathrm{tag}}|, \qquad m_{\mathrm{BC}} = \sqrt{E_{\mathrm{beam}}^2 - |\vec{p_{\mathrm{tag}}}|^2}. \qquad (4.1)$$

These are the energy difference (ΔE) and the beam-constrained mass (m_{BC}), and effectively represent the energy and momentum of the D-tag, respectively. As the candidate with the smallest ΔE for each decay mode in each event is selected, the values will typically peak near $0\,\mathrm{MeV}$. Distributions of m_{BC}, meanwhile, typically peak near $m_{D^0} = 1.865\,\mathrm{GeV}$ or $m_{D^+} = 1.870\,\mathrm{GeV}$. Additionally, while invariant mass ($m_{\mathrm{inv}} = \sqrt{E_{\mathrm{tag}}^2 - |\vec{p_{\mathrm{tag}}}|^2}$) can also be examined, m_{BC} is generally preferred due to a higher precision for the beam energy than of the individual particles comprising the D candidate.

Chapter 5

Measurement of $\sigma_{\psi(3770) \to D\overline{D}}$ near $\psi(3770)$

The main objective of this analysis is to measure the $\sigma_{\psi(3770) \to D\overline{D}}$ cross section at center-of-mass energies around the $\psi(3770)$. While the cross section very near the $\psi(3770)$ mass has been measured with excellent precision [40], the shape over a wider energy range has not been measured to a precise degree. This has left open the possibility of multiple functional shapes which could describe the cross section, and asks the question of whether or not to include interference effects. Fits to this region with a single Breit-Wigner shape (i.e., no interference) have provided a unsatisfactory description of the $\psi(3770)$, and further necessitate the need for interference. The most prominent candidate for shapes with interference assume a contribution from the lower mass $\psi(2S)$ state, and is the form considered here.

5.1   Form Factors

The procedure for this analysis largely follows the methodology of the KEDR collaboration [18]. With the larger statistics available at BESIII, however, an inclusive cross section measurement (such as performed by KEDR) is not required. Instead, the goal is to measure the production rate of $D\overline{D}$ events decaying from $\psi(3770)$ directly. The derivation for this cross section is given in Section 2.3. However, the description of the form factor contribution (Equation (2.9)) must still be determined. Since we assume

the $\psi(2S)$ resonant contribution is negligible in the energy range of our measurements, the only major resonant contribution is from the $\psi(3770)$:

$$F_D(W) = F_D^{\text{NR}}(W) + F_D^{\psi(3770)}(W) \, e^{i\phi^{\psi(3770)}}. \tag{5.1}$$

Currently, there is no definitive model for the non-resonant term, so we use two alternative parameterizations. The first is a simple exponential model:

$$F_D^{NR} = F_{\text{NR}} \, \exp(-q_D^2/a_{\text{NR}}^2), \tag{5.2}$$

where both F_{NR} and a_{NR} are parameters determined through fitting. The second treatment implements a Vector Dominance Model (VDM). This assumes the interference effects are due to the $\psi(2S)$ mediating $D\overline{D}$ production above threshold,

$$F_D^{NR}(W) = F_D^{\psi(2S)}(W) + F_0, \tag{5.3}$$

and that the effective properties of the $\psi(2S)$ are similar to those of the $\psi(3770)$. The real constant F_0 represents the potential effect of higher resonances, like the $\psi(4040)$. The first term is similar to Equation (2.10), but with a modification to the total width:

$$\Gamma^{\psi(2S)}(W) = \left(\frac{M^{\psi(2S)}}{W}\right) \left[\frac{z_{D^0\overline{D^0}}(W) \, d_{D^0\overline{D^0}}(W) + z_{D^+D^-}(W) \, d_{D^+D^-}(W)}{z_{D^0\overline{D^0}}(M^{\psi''}) \, d_{D^0\overline{D^0}}(M^{\psi''}) + z_{D^+D^-}(M^{\psi''}) \, d_{D^+D^-}(M^{\psi''})}\right] \Gamma^{\psi(2S)}(M). \tag{5.4}$$

Without this modification, the mass of the $\psi(2S)$ would be below the $D\overline{D}$ threshold, and thus, the vanishing $z_{D\overline{D}}$ terms would cause a singularity in the width. Therefore, we use the mass of the $\psi(3770)$ in its place to estimate the effects in this region. While it may behave like the total width in Equation (5.4), the true the physical meaning of the parameter $\Gamma^{\psi(2S)}(W)$ is uncertain. For the radii in Equation (2.12), however, the values used are distinct for each meson: $R_{\psi(2S)} = 0.75\,\text{fm}$ and $R_{\psi(3770)} = 1.00\,\text{fm}$.

5.2 Data and Monte Carlo Samples

5.2.1 Data Samples

This analysis primarily uses scan data produced by BEPCII and collected by BESIII in 2010 over an energy range of 3.643 GeV to 3.890 GeV. These data are partitioned into 34 center-of-mass energy (E_{cm}) bins of variable size over a range of 3.735 GeV to 3.870 GeV. The bin partitioning was determined from measurements of center-of-mass energies (Section 5.2.2). The total range was chosen to be above the $D^0\overline{D^0}$ threshold (3.730 GeV) and below the $D^{*0}\overline{D^0}$ threshold (3.872 GeV). This range includes bins which are below the threshold for D^+D^- (3.739 GeV), with production beginning in the third bin.

Additionally, there are three higher statistics points used for comparison. These include an 'On-Peak $\psi(3770)$' sample of 2.93 fb^{-1} at $E_{cm} = 3.7732$ GeV, an 'XYZ-scan' sample of 50.54 pb^{-1} at $E_{cm} = 3.810$ GeV, and an 'R-scan' sample of 7.95 pb^{-1} at $E_{cm} = 3.850$ GeV. The first of these is the high statistics measurement very near the $\psi(3770)$ mass using double-tag reconstruction (both D and $\overline{D}$ in a single event) performed by Derrick Toth. The other two samples were analyzed using the same procedure as for the scan data (See Sections 5.3 to 5.5). None of these points are used to determine the final results, as the differences between samples introduce additional systematics which overshadow any statistical improvement. However, these provide useful comparisons at important energy points along the cross section shape.

5.2.2 Center-of-Mass Energy Measurement

To precisely determine the values of center-of-mass energy along the scan data region, events of $e^+e^- \rightarrow \mu^+\mu^-$ collisions were analyzed to determine their invariant mass (m_{inv}). Assuming minimal radiating energy from the muons, this value is effectively equal to the energy produced by the collider. The selection process for such events is shown in Table 5.1. The statistics of the scan data are too small to precisely determine the energy for individual runs. Therefore, multiple runs were combined together into bins based off the assumption each was taken at nearly identical energies. A comparison of the measured values to the online beam energies is shown in Figure 5.1.

Vertex (xy)	$V_{xy} < 1\,\mathrm{cm}$
Vertex (z)	$|Vz| < 10\,\mathrm{cm}$
MDC Angle	$|\cos\theta|^{\mu^{\pm}} < 0.80$
Muon Opening Angle	$\cos(179.64^\circ) < \cos\theta_{\mu\mu} < \cos(178.60^\circ)$
Energy-Momentum Ratio	$0.05 \leq (E/p)^{\mu^{\pm}} < 0.15$
Shower Energy	$0.0\,\mathrm{GeV} < E_{EMC}^{\mu^{\pm}} < 0.3\,\mathrm{GeV}$

Table 5.1: Selection cuts on muon tracks used to determine the center-of-mass energy.
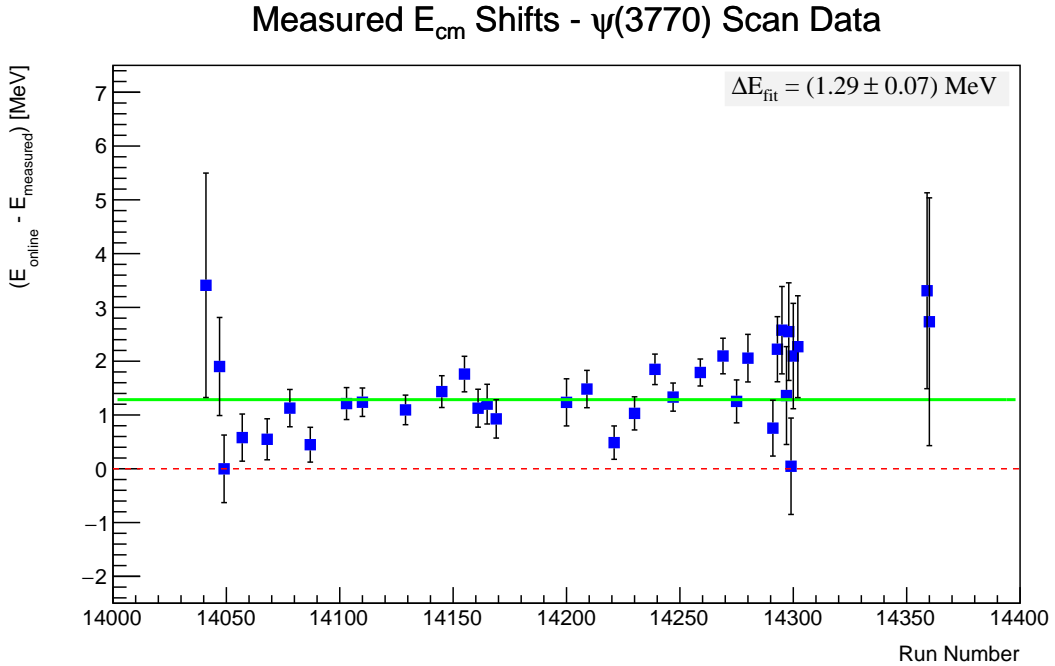
Figure 5.1: The differences measured for scan data center-of-mass energies. The average difference (green) is about 1.29 MeV higher than the recorded energy values provided by the collider at run time (red).

The use of muons to determine energy is subject to an overall scale shift due to potentially miscalibrated magnetic field effects. This requires a point of reference in order to ensure the measured values are correctly determined. We use the first round of the on-peak $\psi(3770)$ sample for this comparison, as its center-of-mass energy has been alternatively measured to a very precise degree [41]. The results of this method compared to our own for the on-peak data are shown in Figure 5.2. It is evident the

official procedure using $D\overline{D}$ events provides more stability over the run range than using muons. Still, the difference between average values of each measurement is taken as the offset for shifting the measured scan data points. From this, the measured center-of-mass energies for the scan data are increased by 1.86 MeV to determine the final values. Compared to the initial measurements of scan data energy, this indicates the values were lower by $\sim$0.7 MeV on average. The final center-of-mass energies of the scan data, along with the luminosity of each bin, are shown in Table 5.3.
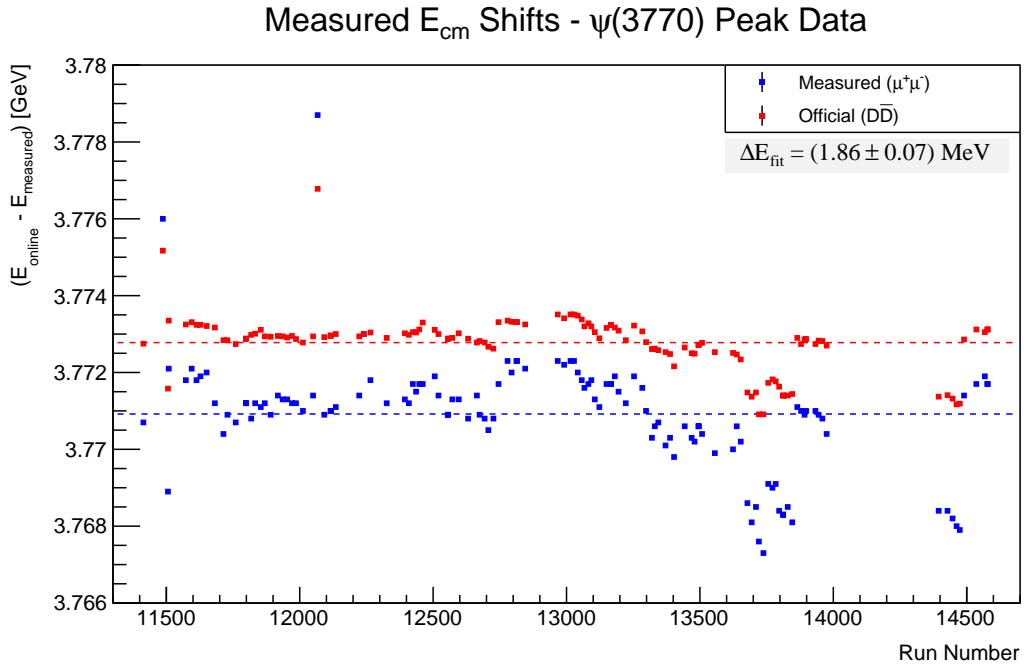
Figure 5.2: The values measured for on-peak data center-of-mass energies. The difference between our measured values (blue) and the official values (red) is used to shift the results of the measured scan data energy values.

5.2.3   Luminosity Measurement

To precisely determine the values of luminosity for each bin, radiative Bhabha events $(e^+e^- \to e^+e^-(\gamma))$ were analyzed to determine the total number of collisions produced. The procedure used is described in Ref. [42]. For each run, 1.4×10^6 events were generated using Babayaga 3.5. We select events with only two (oppositely) charged tracks, satisfying the event selection criteria shown in Table 5.2.

Vertex (xy)	$V_{xy} < 1\,\mathrm{cm}$
Vertex (z)	$|Vz| < 10\,\mathrm{cm}$
MDC Angle	$|\cos\theta| < 0.80$
Exclude $e^+e^- \to \mu^+\mu^-(\gamma)$ Events	$E_{\mathrm{EMC}} > 0.73 \times E_{\mathrm{beam}}$
Exclude $e^+e^- \to \gamma J/\psi,\ J/\psi \to e^+e^-$ Events	$p > 0.93 \times E_{\mathrm{beam}}$

Table 5.2: Selection cuts on electron tracks used to determine the luminosity.

Applying these cuts to both data and MC identically, we use the resulting number of events found in the MC divided by the number of total generated events to determine the efficiency (ϵ_{MC}). From this, and using the cross section provided by the generator (σ_{Bhabha}), we can take the events found in data (N_{data}) to determine the integrated luminosity ($\mathcal{L}$) of each run:

$$\mathcal{L} = \frac{N_{\mathrm{data}}}{\sigma_{\mathrm{Bhabha}}\ \epsilon_{MC}} \tag{5.5}$$

The integrated luminosity for each bin is shown in Table 5.3. The total luminosity for the scan data used is $(69.80 \pm 0.03)\,\mathrm{pb}^{-1}$, where the error listed is statistical.

Bin	Run Range	E_{cm} Range [GeV]	$\mathcal{L}$ [pb^{-1}]
0	14041 - 14046	3.734 - 3.736	0.8293(30)
1	14360 - 14360	3.736 - 3.744	0.3287(19)
2	14047 - 14048	3.744 - 3.748	0.9524(32)
3	14049 - 14053	3.748 - 3.750	1.4055(39)
4	14057 - 14067	3.750 - 3.751	2.2717(50)
5	14068 - 14077	3.751 - 3.753	2.9702(57)
6	14078 - 14086	3.753 - 3.755	3.3080(60)
7	14087 - 14101	3.755 - 3.756	3.4162(61)
8	14103 - 14109	3.756 - 3.759	3.8712(65)
9	14110 - 14123	3.759 - 3.762	4.4382(70)
10	14129 - 14144	3.762 - 3.765	4.4896(70)
11	14145 - 14154	3.765 - 3.767	3.2828(60)
12	14155 - 14160	3.767 - 3.771	2.4418(52)
13	14161 - 14164	3.771 - 3.774	2.0151(47)
14	14165 - 14168	3.774 - 3.777	1.8261(45)
15	14169 - 14174	3.777 - 3.780	1.8237(45)
16	14200 - 14203	3.780 - 3.782	1.9505(46)
17	14209 - 14217	3.782 - 3.787	2.1500(49)
18	14221 - 14226	3.787 - 3.789	2.5488(53)
19	14230 - 14238	3.789 - 3.792	2.8320(56)
20	14239 - 14246	3.792 - 3.797	3.5310(63)
21	14247 - 14258	3.797 - 3.800	4.0479(67)
22	14259 - 14268	3.800 - 3.802	3.9284(66)
23	14269 - 14274	3.802 - 3.807	2.6929(55)
24	14275 - 14279	3.807 - 3.809	1.7604(44)
25	14280 - 14290	3.809 - 3.813	1.2539(38)
26	14291 - 14292	3.813 - 3.815	0.8969(32)
27	14293 - 14294	3.815 - 3.823	0.6803(28)
28	14295 - 14296	3.823 - 3.832	0.3997(21)
29	14297 - 14297	3.832 - 3.839	0.2846(18)
30	14298 - 14298	3.839 - 3.849	0.2802(18)
31	14299 - 14299	3.849 - 3.855	0.2764(18)
32	14300 - 14301	3.855 - 3.863	0.3188(19)
33	14302 - 14303	3.863 - 3.870	0.3002(19)

Table 5.3: Measured luminosities for each energy bin.
The uncertainties listed are statistical errors from the data selection, as uncertainties from the MC statistics are negligible.

5.2.4 Monte Carlo Generation

To compare to the scan data sample, several Monte Carlo (MC) samples were produced. For the main signal determination, samples of generic $D^0\overline{D^0}$ from $\psi(3770)$ and generic D^+D^- from $\psi(3770)$ were generated with 2×10^5 events per bin. In addition, $100\times$ data-size samples were produced for $q\bar{q}$, $\tau^-\tau^+$, radiative return to J/ψ (denoted $\gamma J/\psi$), and radiative return to $\psi(2S)$ (denoted $\gamma\psi'$). Each of these samples was generated at the University of Minnesota in July of 2014 using BOSS 6.6.4.p02. The $D^0\overline{D^0}$, D^+D^-, $q\bar{q}$, and $\tau^-\tau^+$ states were generated using KKMC, while the $\gamma J/\psi$ and $\gamma\psi'$ were generated with BesEvtGen. All except $q\bar{q}$ were then decayed with BesEvtGen. The total numbers of events in each sample can be found in Table 5.4.

Sample	Number of Events
$\psi(3770) \to D^0\overline{D^0}$	6.800×10^6
$\psi(3770) \to D^+D^-$	6.400×10^6
$q\bar{q}$	8.916×10^7
$\gamma J/\psi$	7.307×10^6
$\gamma\psi'$	2.457×10^7
$\tau^-\tau^+$	2.164×10^7
Data	4.844×10^8

Table 5.4: Number of events contained in each generated sample and the scan data.

In general, all MC samples were generated based off communal decay card information used within BESIII. However, the $D\overline{D}$ samples were generated by implementing the Born-level cross section shape from the final fit into KKMC. This procedure was repeated over five iterations in order to provide a more data-driven basis for the ISR corrections. The effects of this process are examined in Section 5.6.

5.2.5 Software Packages

The main packages used for this analysis are shown in Table 5.5. The package `DtagRecAlg` is a custom package used to extract variables from `DTagAlg` relevant to the analysis.

Package	Version
KKMC	v00-00-51
DTagAlg	v00-00-51
DTagRecAlg	v00-00-01

Table 5.5: The software packages used in this analysis and their version numbers.

5.3 Signal Determination

We measure the yields of both $D^0\overline{D^0}$ and D^+D^- events with two-dimensional fits to ΔE and m_{BC}. MC samples are partitioned into the following four groups: proper D-tags ($N_{D\overline{D}}$), misreconstructed D-tags (N_{misrec}), continuum ($N_{q\bar{q}}$), and other (N_{other}). The first two groups are obtained using truth information from the $D\overline{D}$ samples, while the last group is a combination of the $\tau^-\tau^+$, $\gamma J/\psi$, and $\gamma\psi'$ samples. These groups are fitted to data using the RooFit package to perform a negative log-likelihood minimization for each energy bin (E_i) separately for both D^0 and D^+. For each fit, the four MC sample groups are used to construct 2D (ΔE vs. m_{BC}) PDF functions that are fitted against the corresponding data histograms. The proper $D\overline{D}$ shape is treated as signal, and its integral after fitting (N_D) is used for determining the signal yields and cross sections. An example fit is shown in Fig. 5.3, while the complete set of these plots can be found in Appendices B and C.
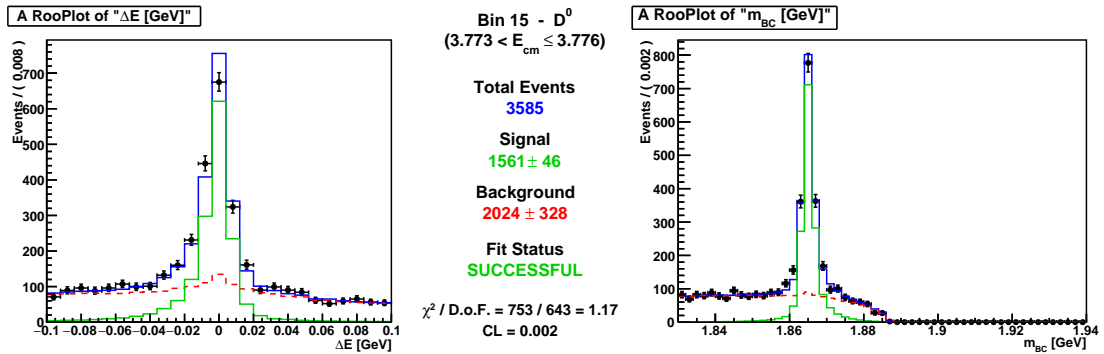

Figure 5.3: An example 2D (ΔE vs. m_{BC}) signal fit.
The covers D^0 events in the region $3.773\,\mathrm{GeV} < E_{\mathrm{cm}} \leq 3.776\,\mathrm{GeV}$. The data points (black) are fitted by the total MC shape (blue), which is the sum of the signal (green) and background (red) components.

5.4   Efficiency Correction

In addition to the parameters gathered by `DTagAlg`, truth information was taken from the generic $D\overline{D}$ samples in order to determine the mode-by-mode reconstruction efficiency. To be deemed proper, a reconstruction must pass not only the standard D-tag cuts, but also match the generator information for the event. This process removes peaking backgrounds from modes with similar constituents. The total number of proper D-tag reconstructions is then divided by the number of D particles generated for each mode, and the mode-by-mode efficiencies are weighted by the PDG branching ratios [1] to determine the overall efficiency (ϵ_D) for each of D^0 and D^+:

$$\epsilon_D = \sum_i \epsilon_{i\ \text{rec}}\, \mathcal{B}_i = \sum_i \left(\frac{N_{i\ \text{prop}}}{N_{i\ \text{gen}}} \right) \mathcal{B}_i. \tag{5.6}$$

Each D^0 efficiency also includes the corresponding DCSD terms for its decay (See Section 4.3).

To determine the cross section at each point, this procedure was applied separately for each energy bin. The total number of proper and generated particles for each energy bin are shown in Table 5.6 for D^0 and Tables 5.7 and 5.8 for D^+. The efficiencies for D^+ and D^0 were also calculated across the total sample, and are shown for each mode in Table 5.9 and Figure 5.4. Total efficiencies of each bin for both D^0 and D^+ are shown in Table 5.10.

5.4.1   CP Violation Correction

Due to CP violation in the $D^0\overline{D^0}$ system, each of the neutral decay modes must be corrected to account for quantum correlations. This is done by applying scaling factors to the efficiency for each of the three modes used in reconstruction. The corrections are parameterized for each mode (m) by the following form [43]:

$$\alpha_{D^0 \to m} = 1 + r_m^2 + 2 \times y \times r_m \times R_m \times \cos(\delta_m). \tag{5.7}$$

Here, r_m and δ_m represent the relative magnitudes and phases between the Cabbibo-favored and doubly-Cabbibo-suppressed modes, respectively, while the factor of R_m

Bin	$D^0 \to K^- \pi^+$			$D^0 \to K^- \pi^+ \pi^0$			$D^0 \to K^- \pi^+ \pi^+ \pi^-$		
	N_{prop}	N_{gen}	ϵ_{rec}	N_{prop}	N_{gen}	ϵ_{rec}	N_{prop}	N_{gen}	ϵ_{rec}
0	11197	15757	0.711	21600	55815	0.387	13592	33714	0.403
1	11266	15713	0.717	21735	56189	0.387	13651	33621	0.406
2	11065	15557	0.711	21683	55791	0.389	13984	33431	0.418
3	10748	15501	0.693	21114	55767	0.379	13168	33505	0.393
4	11176	15779	0.708	21922	55873	0.392	13613	33410	0.407
5	10984	15722	0.699	21366	56027	0.381	13483	33748	0.400
6	10837	15507	0.699	21144	55551	0.381	13738	33639	0.408
7	10707	15645	0.684	20889	56193	0.372	13074	33494	0.390
8	11031	15585	0.708	21788	55891	0.390	13967	33826	0.413
9	10994	15485	0.710	21978	56012	0.392	14020	33601	0.417
10	10952	15497	0.707	21400	56126	0.381	13727	33591	0.409
11	11025	15535	0.710	21700	55919	0.388	13980	33706	0.415
12	10909	15593	0.700	21713	55876	0.389	13787	33335	0.414
13	11088	15826	0.701	21696	55758	0.389	14013	33805	0.415
14	10975	15620	0.703	21576	55591	0.388	14039	33581	0.418
15	10965	15672	0.700	21501	55647	0.386	13777	33644	0.409
16	10803	15438	0.700	21505	55667	0.386	13832	33822	0.409
17	10913	15473	0.705	21574	56023	0.385	14163	34131	0.415
18	11156	15856	0.704	21461	55706	0.385	13725	33321	0.412
19	11124	15728	0.707	21775	56192	0.388	13930	33935	0.410
20	10837	15530	0.698	21149	55737	0.379	13883	33703	0.412
21	10756	15397	0.699	21212	55815	0.380	13577	33907	0.400
22	10986	15582	0.705	21178	56343	0.376	13352	33773	0.395
23	11147	15861	0.703	21088	56167	0.375	13200	33680	0.392
24	10785	15633	0.690	20763	55952	0.371	12651	33660	0.376
25	10972	15490	0.708	20687	55957	0.370	12841	33512	0.383
26	11016	15645	0.704	20707	55785	0.371	12563	33615	0.374
27	10800	15420	0.700	20244	55748	0.363	12362	33359	0.371
28	10939	15694	0.697	20077	55550	0.361	12507	33497	0.373
29	10839	15689	0.691	20685	56386	0.367	12575	33551	0.375
30	10798	15766	0.685	20238	55433	0.365	12526	33885	0.370
31	10568	15438	0.685	20533	55825	0.368	12901	33745	0.382
32	10820	15679	0.690	20706	55823	0.371	13155	33810	0.389
33	10643	15736	0.676	20488	55672	0.368	12875	33547	0.384

Table 5.6: Number of proper and generated particles for D^0.
The mode-by-mode numbers of particles used in the efficiency calculations for $D^0 \to K^- \pi^+, D^0 \to K^- \pi^+ \pi^0$, and $D^0 \to K^- \pi^+ \pi^+ \pi^-$.

Bin	$D^+ \rightarrow K^- \pi^+ \pi^+$			$D^+ \rightarrow K^- \pi^+ \pi^+ \pi^0$			$D^+ \rightarrow K^0_S \pi^+$		
	N_{prop}	N_{gen}	ϵ_{rec}	N_{prop}	N_{gen}	ϵ_{rec}	N_{prop}	N_{gen}	ϵ_{rec}
2	20643	37609	0.549	6853	24250	0.283	2302	5900	0.390
3	19935	37582	0.530	6569	24235	0.271	2335	6114	0.382
4	20859	37915	0.550	6653	24216	0.275	2291	5879	0.390
5	20193	37647	0.536	6611	24051	0.275	2292	5965	0.384
6	20484	37814	0.542	6616	24184	0.274	2292	5924	0.387
7	19635	37462	0.524	6411	24708	0.259	2127	5815	0.366
8	20876	37758	0.553	6867	24343	0.282	2328	5841	0.399
9	20873	37739	0.553	6754	24284	0.278	2377	5911	0.402
10	20571	37487	0.549	6604	24249	0.272	2360	6010	0.393
11	20669	37468	0.552	6818	24268	0.281	2296	5904	0.389
12	20843	37838	0.551	6783	24247	0.280	2401	6074	0.395
13	20486	37286	0.549	6942	24582	0.282	2335	6184	0.378
14	20935	37961	0.551	6836	24467	0.279	2282	5963	0.383
15	20543	37458	0.548	6769	24135	0.280	2295	5889	0.390
16	20713	37543	0.552	6758	24376	0.277	2356	5921	0.398
17	21016	37757	0.557	6949	24470	0.284	2302	5903	0.390
18	21123	38024	0.556	6635	24111	0.275	2320	5889	0.394
19	20708	37357	0.554	6662	24240	0.275	2204	5855	0.376
20	20760	37761	0.550	6768	24395	0.277	2263	5883	0.385
21	20860	37893	0.550	6668	24216	0.275	2296	5996	0.383
22	20827	37820	0.551	6673	24421	0.273	2353	5997	0.392
23	20796	37554	0.554	6723	24377	0.276	2290	5957	0.384
24	20058	37410	0.536	6415	24310	0.264	2341	5966	0.392
25	20677	37552	0.551	6462	24245	0.267	2364	5987	0.395
26	20300	37491	0.541	6539	24405	0.268	2356	5993	0.393
27	20754	37704	0.550	6530	24295	0.269	2288	5969	0.383
28	20213	37428	0.540	6362	24146	0.263	2341	5988	0.391
29	20565	37545	0.548	6495	24257	0.268	2262	5916	0.382
30	20313	37773	0.538	6535	24167	0.270	2323	6075	0.382
31	20322	37280	0.545	6566	24389	0.269	2378	5927	0.401
32	20883	37992	0.550	6594	24249	0.272	2306	5855	0.394
33	20645	37738	0.547	6560	24195	0.271	2269	5945	0.382

Table 5.7: Number of proper and generated particles for D^+ (part 1).
The mode-by-mode numbers of particles used in the efficiency calculations for
$D^+ \rightarrow K^- \pi^+ \pi^+, D^+ \rightarrow K^- \pi^+ \pi^+ \pi^0$, and $D^+ \rightarrow K^0_S \pi^+$.

Bin	$D^+ \to K_S^0 \pi^+ \pi^0$			$D^+ \to K_S^0 \pi^+ \pi^+ \pi^-$			$D^+ \to K^+ K^- \pi^+$		
	N_{prop}	N_{gen}	ϵ_{rec}	N_{prop}	N_{gen}	ϵ_{rec}	N_{prop}	N_{gen}	ϵ_{rec}
2	5742	27235	0.211	3562	15019	0.237	1720	4019	0.428
3	5668	27699	0.205	3169	14877	0.213	1637	3970	0.412
4	5710	27527	0.207	3358	14750	0.228	1791	4016	0.446
5	5614	27654	0.203	3282	14696	0.223	1748	3981	0.439
6	5656	27475	0.206	3392	14823	0.229	1771	4075	0.435
7	5481	27597	0.199	3293	14860	0.222	1593	3951	0.403
8	5827	27975	0.208	3462	15035	0.230	1736	4042	0.429
9	6003	27589	0.218	3427	14906	0.230	1716	3940	0.436
10	5722	27751	0.206	3327	14854	0.224	1690	3941	0.429
11	5888	27649	0.213	3385	14837	0.228	1672	3930	0.425
12	5731	27651	0.207	3370	14926	0.226	1718	3889	0.442
13	5792	27618	0.210	3336	14669	0.227	1696	3958	0.428
14	5745	27608	0.208	3288	14702	0.224	1712	3904	0.439
15	5832	27480	0.212	3384	14808	0.229	1649	3855	0.428
16	5891	27758	0.212	3443	14845	0.232	1783	3947	0.452
17	5954	27639	0.215	3484	14910	0.234	1804	3941	0.458
18	5875	27669	0.212	3366	14913	0.226	1700	3968	0.428
19	5773	27838	0.207	3371	14782	0.228	1766	4037	0.437
20	6024	28019	0.215	3367	14801	0.227	1709	3903	0.438
21	5804	27645	0.210	3306	14819	0.223	1688	3863	0.437
22	5893	27692	0.213	3304	14949	0.221	1741	3975	0.438
23	5780	27865	0.207	3313	14981	0.221	1670	3891	0.429
24	5623	27811	0.202	3161	14867	0.213	1667	3954	0.422
25	5684	27490	0.207	3250	14794	0.220	1711	3966	0.431
26	5704	27829	0.205	3137	14811	0.212	1641	3958	0.415
27	5630	27497	0.205	3132	14881	0.210	1678	3972	0.422
28	5724	28006	0.204	3271	14828	0.221	1690	3931	0.430
29	5693	27554	0.207	3272	15009	0.218	1772	3994	0.444
30	5574	27717	0.201	3308	14730	0.225	1673	4026	0.416
31	5556	27556	0.202	3288	15049	0.218	1746	3965	0.440
32	5785	27634	0.209	3259	14840	0.220	1680	3923	0.428
33	5653	27528	0.205	3287	14959	0.220	1734	4031	0.430

Table 5.8: Number of proper and generated particles for D^+ (part 2).
The mode-by-mode numbers of particles used in the efficiency calculations for
$D^+ \to K_S^0 \pi^+ \pi^0, D^+ \to K_S^0 \pi^+ \pi^+ \pi^-$, and $D^+ \to K^+ K^- \pi^+$.

Decay Mode (i)	PDG $\mathcal{B}_i$ [%]	MC Efficiency ϵ_i
$D^0 \to K^- \pi^+$	3.89 ± 0.05	0.7002 ± 0.0011
$D^0 \to K^- \pi^+ \pi^0$	13.93 ± 0.50	0.3794 ± 0.0004
$D^0 \to K^- \pi^+ \pi^+ \pi^-$	8.11 ± 0.21	0.3988 ± 0.0006
$\epsilon_{D^0} = (11.245 \pm 0.020)\%$		
$D^+ \to K^- \pi^+ \pi^+$	9.13 ± 0.19	0.5471 ± 0.0007
$D^+ \to K^- \pi^+ \pi^+ \pi^0$	5.99 ± 0.18	0.2739 ± 0.0006
$D^+ \to K^0_S \pi^+$	1.47 ± 0.07	0.3883 ± 0.0014
$D^+ \to K^0_S \pi^+ \pi^0$	6.99 ± 0.27	0.2079 ± 0.0005
$D^+ \to K^0_S \pi^+ \pi^+ \pi^-$	3.12 ± 0.11	0.2237 ± 0.0007
$D^+ \to K^+ K^- \pi^+$	0.95 ± 0.03	0.4317 ± 0.0018
$\epsilon_{D^+} = (9.770 \pm 0.063)\%$		

Table 5.9: Mode-by-mode reconstruction efficiencies for D^0 and D^+. The values shown are over the entire data sample, while calculations for the cross sections use the values of each energy point individually (see Table 5.10). The errors listed on the PDG branching fractions are shown for reference, and are not included in the efficiency errors (see Section 5.6.1).

represents a coherence factor characterizing the variation of δ_m over phase space. Note, there is no such variation for a two-body decay (like $D^0 \to K^- \pi^+$), so $R_{D^0 \to K^- \pi^+} = 1$. The value of y represents the difference in total width components of the $D^0 \overline{D^0}$ system, $y = (\Gamma_2 - \Gamma_1)/(\Gamma_2 + \Gamma_1)$, where 1 and 2 represent the CP-odd and CP-even states, respectively.

The mode-dependent values for these factors are listed in Table 5.11. These are taken from the CPV-allowed values in [44] for $D^0 \to K^- \pi^+$, and from [45] for $D^0 \to K^- \pi^+ \pi^0$ and $D^0 \to K^- \pi^+ \pi^+ \pi^-$. The value of $y = 0.0066^{+0.0007}_{-0.0010}$ is also from [44], and is the same for all modes. After applying each of the mode-dependent corrections, the efficiency for the full sample changes from $\epsilon_{D^0} = (11.320 \pm 0.213)\%$ to $\epsilon_{D^0} = (11.352 \pm 0.213)\%$, and similarly for the efficiencies of each E_{cm} bin.

Mode	r_m	R_m	δ_m [°]	α_m
$D^0 \to K^- \pi^+$	0.0591 ± 0.0063	1	$11.8^{+9.5}_{-14.7}$	1.00426 ± 0.00083
$D^0 \to K^- \pi^+ \pi^0$	0.0447 ± 0.0012	0.81 ± 0.06	18^{+14}_{-15}	1.00248 ± 0.00014
$D^0 \to K^- \pi^+ \pi^+ \pi^-$	0.0549 ± 0.0006	$0.43^{+0.17}_{-0.13}$	-52^{+28}_{-17}	$1.00270^{+0.00014}_{-0.00012}$

Table 5.11: The quantum correlated factors for the D^0 modes.

E_{bin}	ϵ_{D^0}	ϵ_{D^+}
0	0.1146 ± 0.0005	-
1	0.1151 ± 0.0005	-
2	0.1161 ± 0.0005	0.0990 ± 0.0005
3	0.1119 ± 0.0005	0.0952 ± 0.0005
4	0.1156 ± 0.0005	0.0983 ± 0.0005
5	0.1131 ± 0.0005	0.0964 ± 0.0005
6	0.1137 ± 0.0005	0.0972 ± 0.0005
7	0.1104 ± 0.0005	0.0934 ± 0.0005
8	0.1157 ± 0.0005	0.0991 ± 0.0005
9	0.1165 ± 0.0005	0.0996 ± 0.0005
10	0.1141 ± 0.0005	0.0977 ± 0.0005
11	0.1157 ± 0.0005	0.0990 ± 0.0005
12	0.1152 ± 0.0005	0.0986 ± 0.0005
13	0.1154 ± 0.0005	0.0985 ± 0.0005
14	0.1157 ± 0.0005	0.0984 ± 0.0005
15	0.1146 ± 0.0005	0.0986 ± 0.0005
16	0.1146 ± 0.0005	0.0992 ± 0.0005
17	0.1151 ± 0.0005	0.1003 ± 0.0005
18	0.1148 ± 0.0005	0.0990 ± 0.0005
19	0.1151 ± 0.0005	0.0984 ± 0.0005
20	0.1138 ± 0.0005	0.0988 ± 0.0005
21	0.1129 ± 0.0005	0.0982 ± 0.0005
22	0.1122 ± 0.0005	0.0984 ± 0.0005
23	0.1118 ± 0.0005	0.0982 ± 0.0005
24	0.1094 ± 0.0005	0.0953 ± 0.0005
25	0.1105 ± 0.0005	0.0975 ± 0.0005
26	0.1098 ± 0.0005	0.0962 ± 0.0005
27	0.1082 ± 0.0005	0.0969 ± 0.0005
28	0.1081 ± 0.0005	0.0961 ± 0.0005
29	0.1087 ± 0.0005	0.0971 ± 0.0005
30	0.1078 ± 0.0005	0.0959 ± 0.0005
31	0.1092 ± 0.0005	0.0969 ± 0.0005
32	0.1104 ± 0.0005	0.0978 ± 0.0005
33	0.1090 ± 0.0005	0.0971 ± 0.0005

Table 5.10: The overall reconstruction efficiency of D^0 and D^+ for each energy bin. These values are used to calculate the corresponding cross sections at each energy point. The listed errors are statistical only.

Monte Carlo Efficiency per Mode
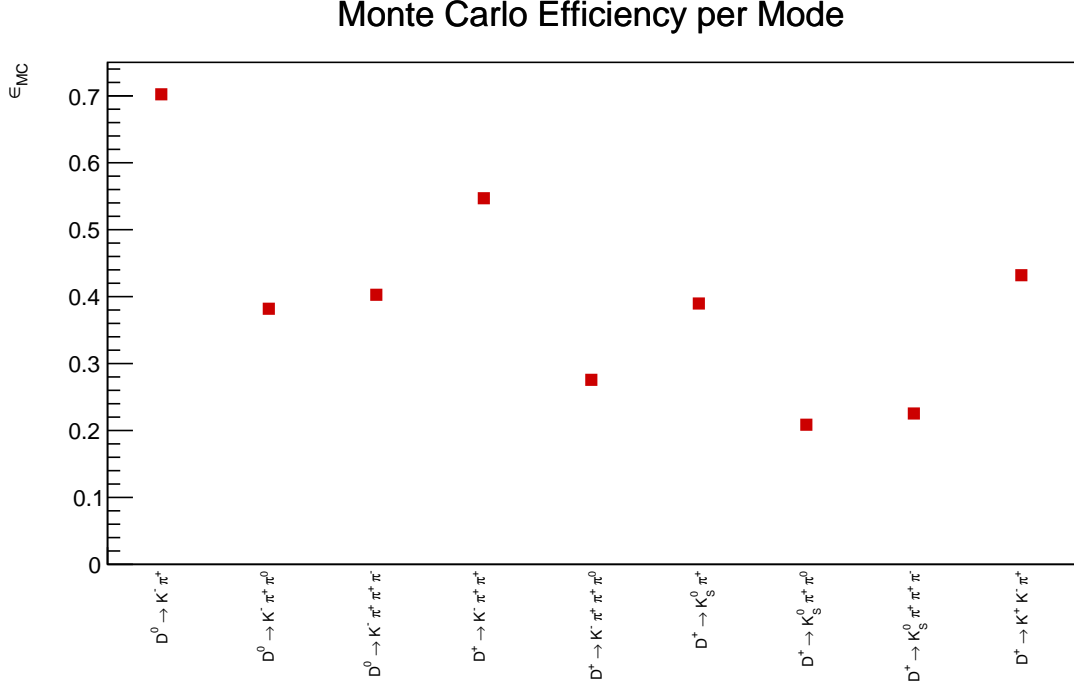
Figure 5.4: Mode-by-mode MC efficiencies for D^0 and D^+.
The error bars are negligible on the scale shown.

5.5 Fitting Procedure

After applying the correction in Section 5.4.1, the efficiency values (Table 5.10) were combined with the luminosity (Table 5.3) and the signal values from each 2D fit (Table 5.12) to determine the cross section at each energy point. Since each $\psi(3770)$ produces a $D\overline{D}$ pair, a factor of 2 is included to avoid double counting:

$$\sigma_{D\overline{D}}^{RC}(E_i) = \frac{N_D(E_i)}{2\,\epsilon_D(E_i)\,\mathcal{L}(E_i)}. \tag{5.8}$$

The resulting cross section values for D^0 and D^+ are also listed in Table 5.12, and shown in Figure 5.5.

Using the measured $D\overline{D}$ cross sections, we fit to Equation (2.7) using each of the form factor choices described in Section 5.1. In each case, there are four common fit parameters: $M^{\psi(3770)}$, $\Gamma^{\psi(3770)}$, $\Gamma_{ee}^{\psi(3770)}$, and $\phi^{\psi(3770)}$. These represent the mass, total

E_{mid}	$N_{D^0\overline{D^0}}$	$\sigma^{RC}_{D^0\overline{D^0}}$ [nb]	$N_{D^+D^-}$	$\sigma^{RC}_{D^+D^-}$ [nb]
3.7342	31 ± 9	0.164 ± 0.046	-	-
3.7368	16 ± 5	0.218 ± 0.068	-	-
3.7447	169 ± 16	0.765 ± 0.070	28 ± 7	0.150 ± 0.038
3.7483	264 ± 20	0.838 ± 0.064	96 ± 13	0.360 ± 0.048
3.7501	509 ± 28	0.968 ± 0.053	196 ± 18	0.439 ± 0.040
3.7517	831 ± 34	1.237 ± 0.052	329 ± 23	0.574 ± 0.040
3.7534	1036 ± 38	1.377 ± 0.051	481 ± 27	0.748 ± 0.042
3.7556	1182 ± 41	1.566 ± 0.055	508 ± 28	0.797 ± 0.045
3.7562	1459 ± 45	1.629 ± 0.051	701 ± 32	0.914 ± 0.042
3.7592	2014 ± 52	1.948 ± 0.052	1054 ± 39	1.192 ± 0.045
3.7624	2444 ± 58	2.385 ± 0.058	1346 ± 44	1.534 ± 0.051
3.7650	2062 ± 53	2.715 ± 0.071	1223 ± 42	1.882 ± 0.066
3.7676	1746 ± 48	3.102 ± 0.087	1059 ± 39	2.200 ± 0.081
3.7713	1585 ± 46	3.406 ± 0.101	1045 ± 38	2.634 ± 0.098
3.7742	1569 ± 46	3.714 ± 0.111	1103 ± 40	3.067 ± 0.111
3.7775	1543 ± 46	3.692 ± 0.111	1108 ± 39	3.078 ± 0.111
3.7802	1539 ± 46	3.444 ± 0.104	1006 ± 38	2.599 ± 0.100
3.7829	1381 ± 44	2.791 ± 0.090	951 ± 38	2.206 ± 0.088
3.7869	1167 ± 42	1.995 ± 0.072	821 ± 36	1.627 ± 0.073
3.7891	888 ± 38	1.361 ± 0.058	656 ± 34	1.178 ± 0.062
3.7926	739 ± 36	0.920 ± 0.045	475 ± 32	0.680 ± 0.045
3.7970	514 ± 34	0.562 ± 0.037	329 ± 31	0.414 ± 0.039
3.8003	374 ± 31	0.424 ± 0.035	186 ± 28	0.241 ± 0.037
3.8024	196 ± 23	0.325 ± 0.038	125 ± 23	0.236 ± 0.043
3.8070	136 ± 19	0.352 ± 0.050	97 ± 17	0.289 ± 0.051
3.8093	65 ± 14	0.233 ± 0.050	32 ± 13	0.132 ± 0.055
3.8135	12 ± 10	0.060 ± 0.049	26 ± 11	0.153 ± 0.066
3.8153	8 ± 7	0.056 ± 0.051	12 ± 8	0.089 ± 0.063
3.8229	12 ± 7	0.140 ± 0.083	15 ± 8	0.197 ± 0.107
3.8320	4 ± 5	0.069 ± 0.086	3 ± 5	0.046 ± 0.099
3.8390	14 ± 6	0.237 ± 0.105	14 ± 7	0.254 ± 0.124
3.8494	11 ± 6	0.186 ± 0.104	10 ± 6	0.186 ± 0.118
3.8555	24 ± 8	0.337 ± 0.111	17 ± 6	0.273 ± 0.104
3.8632	22 ± 8	0.340 ± 0.127	6 ± 5	0.099 ± 0.091

Table 5.12: The $D\overline{D}$ cross section at each E_{cm} point.
The number of data events observed in each E_{cm} bin are also shown. The uncertainties on the cross sections are statistical only and come from the signal fitting (N_D), PDG values (Table 5.9), and MC reconstruction efficiency (Table 5.10). The values for $N_{D^0\overline{D^0}}$ and $N_{D^+D^-}$ are taken from the signal fits shown in Appendices B and C.
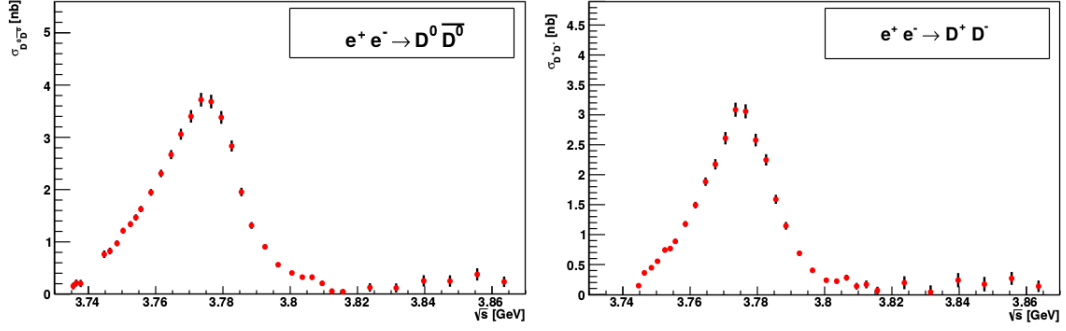
Figure 5.5: The measured $e^+e^- \to D\overline{D}$ cross sections.
The $D^0\overline{D^0}$ cross section is shown on the left and D^+D^- is shown on the right.

width, electron partial width, and relative phase to the non-resonant contribution for the $\psi(3770)$, respectively. This notation for the total width corresponds to $\Gamma(M)$ in Section 2.3. Two additional fitting parameters are dependent on which form factor is being used: F_{NR} and a_{NR} for the exponential, or $\Gamma^{\psi(2S)}$ and F_0 for the VDM. For the former, these represent the amplitude and exponent normalization for the non-resonant contribution. In the latter case, these represent the modified total width for the $\psi(2S)$ above resonance (see Section 5.1) and the constant contribution of resonances above the $\psi(3770)$. The fitting is done simultaneously for D^0 and D^+ with identical parameters using TMinuit with a χ^2 minimization. The value minimized is the sum of the χ^2 values from each of the D^0 and D^+ cross section functions. Results for the Exponential and VDM choices are shown in Figures 5.6 and 5.7, respectively.
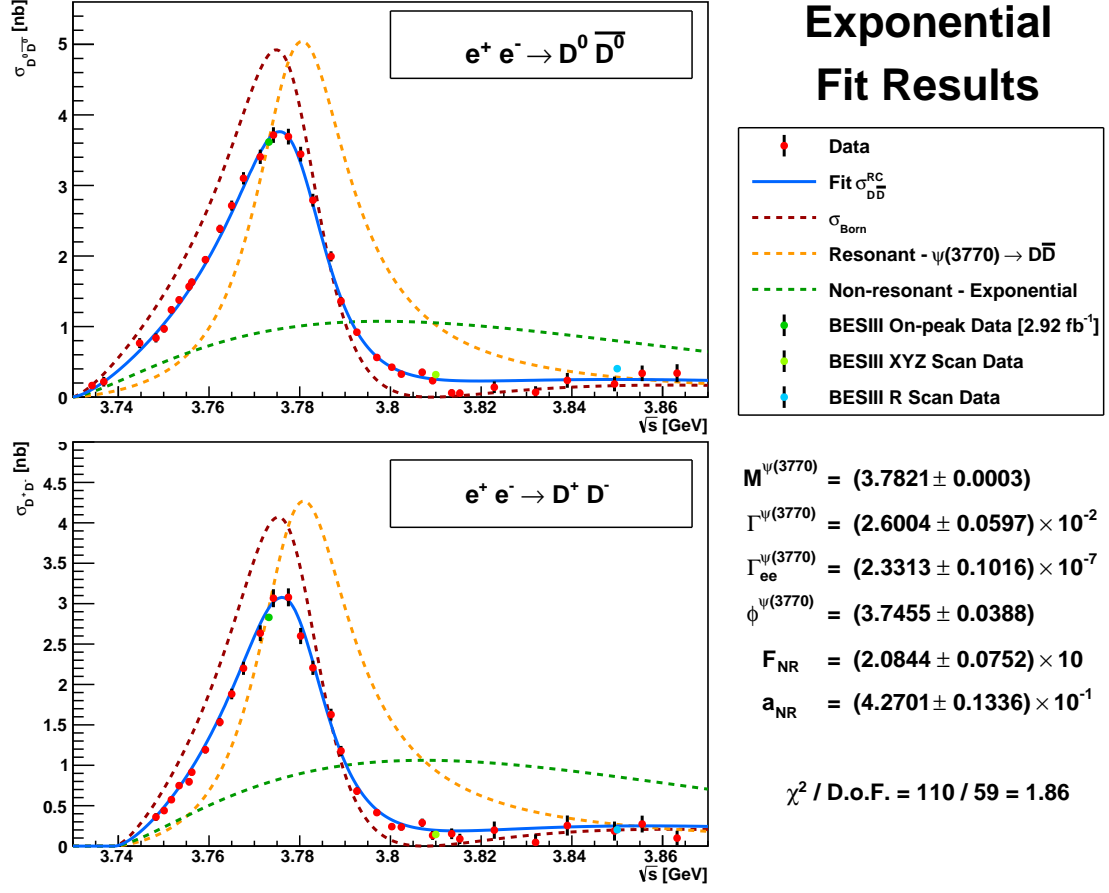
Figure 5.6: The Exponential Model fit results.
The results for D^0 are shown on the top and the results for D^+ are shown on the bottom. The fit shape (blue) is calculated from Equation (2.1) using the non-resonant component from Equation (5.2).
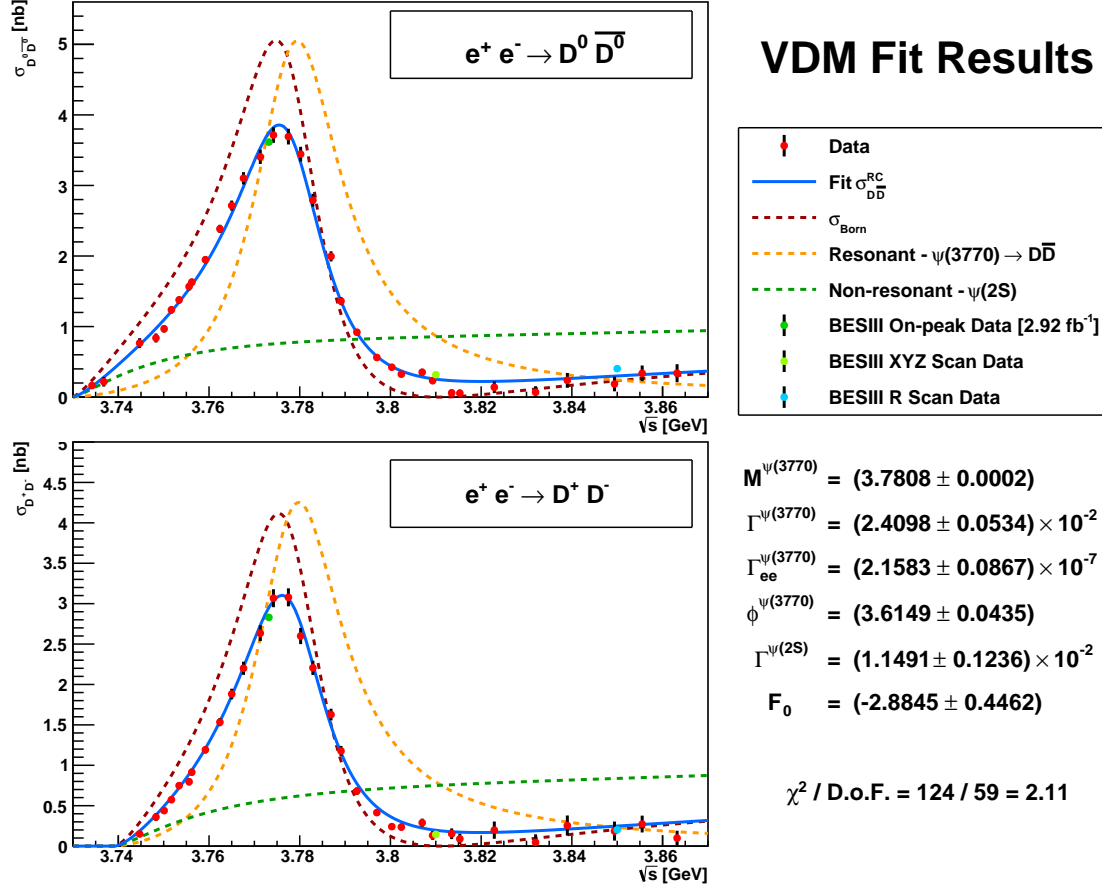
Figure 5.7: The Vector Dominance Model fit results.
The results for D^0 are shown on the top and the results for D^+ are shown on the bottom. The fit shape (blue) is calculated from Equation (2.1) using the non-resonant component from Equation (5.3).

5.5.1   Coulomb Correction

In the development of this analysis, it was discovered that the theoretical formulation in Section 2.3 did not lead to a successful fit of the $D\overline{D}$ cross sections, shown in Figure 5.8. Namely, including the Coulomb effect pulls the $D^0\overline{D^0}$ and D^+D^- cross sections in opposite directions. We found the best fits were achieved by altering Equation (2.3) to set the Coulomb factor to 1. While this disagrees with conventional theoretical wisdom, it is consistent with studies of $\Upsilon(4S) \to B\overline{B}$ where applying a Coulomb correction for the charged final state also leads to inconsistency with data.
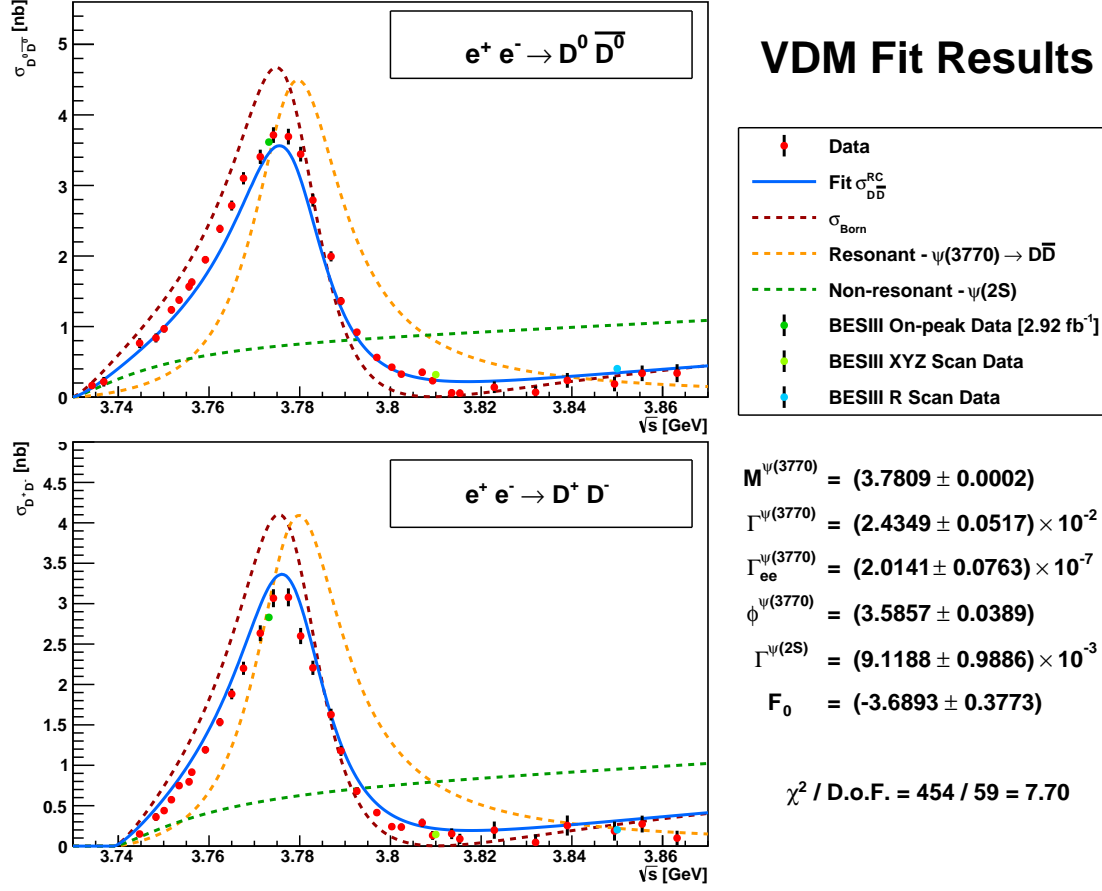
Figure 5.8: The Vector Dominance Model fit results with Coulomb interactions. The results for D^0 are shown on the top and the results for D^+ are shown on the bottom. Including this factor provides notably worse results than when excluding it (see Figure 5.7).

This is most clearly seen in the ratio of D^+D^- and $D^0\overline{D^0}$ cross sections, shown in Figure 5.9, where the 'No Coulomb' method sets $z_{D^+D^-}$ in Equations (2.7) and (2.11) to unity, the 'Partial Coulomb' sets this factor to unity only for Equation (2.7), and the 'Full Coulomb' is the default assumption. Agreement of the measured cross section ratio with the 'No Coulomb' calculation is substantially better. This is also true for the high statistics points measured at the $\psi(3770)$ peak by Derrick Toth [40] (light blue). As the data tend to follow the 'No Coulomb' method, we choose this as our nominal method for the results, presented in Section 5.7. However, the interpretation for this

behavior is still undetermined.
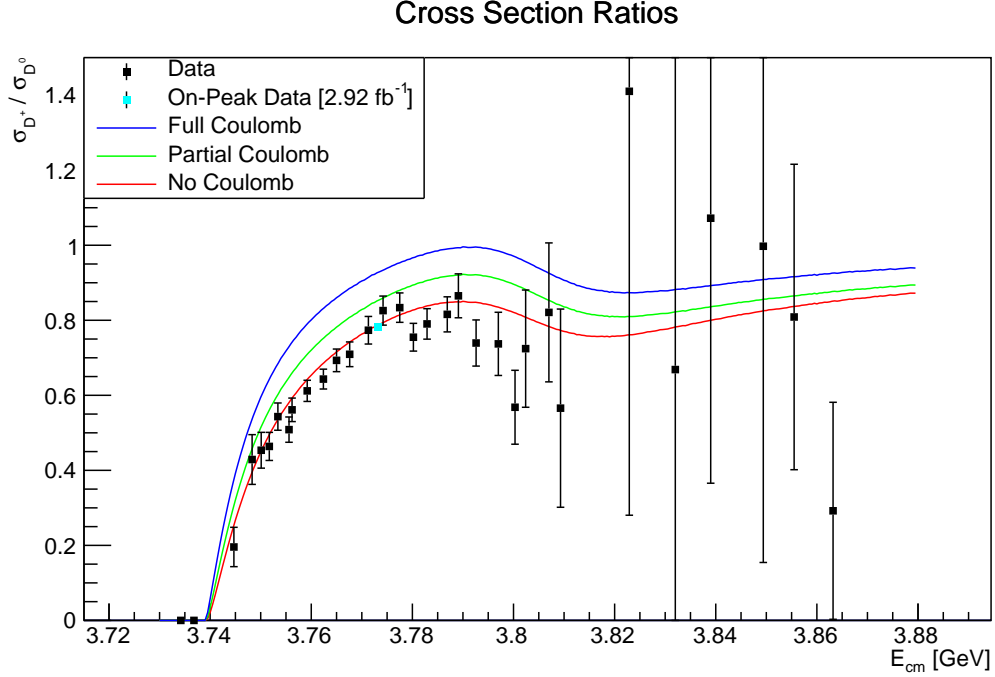
Figure 5.9: The ratio of measured D^+ to D^0 cross sections. Several levels of Coulomb interactions are examined.

5.6 Systematics

To assess the systematic uncertainties in our results, we look at a variety of factors. Many of these affect all BESIII analyses, such as luminosity and tracking. Others, like the modification to KKMC generation (see Section 5.2.4), are specific to this analysis. The remaining systematics are typically due to less well-known parameters, like the radii used to describe the $\psi(2S)$ and $\psi(3770)$ (see Section 5.1). Each of these contributions, as well as their total, can be found in Table 5.16.

5.6.1 $\psi(3770)$ Parameter Systematics

Each systematic is obtained by changing a specific aspect, and re-fitting to the altered values using the VDM method. The uncertainties for each parameter are obtained by

taking the difference between this result and the nominal fit (Figure 5.7). Generally, each change was done both positively and negatively, and the values used are the largest differences seen between the two changes. The systematics examined in this analysis are summarized below, where a * denotes aspects which were deemed negligible.

Luminosity

A 1 % change [46] was applied to $\mathcal{L}$ in Equation (5.8). As this is an overall scale change, the only variable significantly affected is $\Gamma_{ee}^{\psi(3770)\to D\overline{D}}$.

$\pi^{\pm}/K^{\pm}$ Tracking

A 1.0 % change [47] was applied for each $\pi^{\pm}$ or $K^{\pm}$ in a given decay mode. The summed contribution for each mode is applied to ϵ_m in Equation (5.6). As this is an overall scale change, the only variable significantly affected is $\Gamma_{ee}^{\psi(3770)\to D\overline{D}}$.

π^0 Tracking

A 2.0 % change [48] was applied for each π^0 in a given decay mode. The summed contribution for each mode is applied to ϵ_m in Equation (5.6). As this is an overall scale change, the only variable significantly affected is $\Gamma_{ee}^{\psi(3770)\to D\overline{D}}$.

K_S^0 Tracking

A 1.5 % change [49] was applied for each K_S^0 in a given decay mode. The summed contribution for each mode is applied to ϵ_m in Equation (5.6). As this is an overall scale change, the only variable significantly affected is $\Gamma_{ee}^{\psi(3770)\to D\overline{D}}$.

Single Tag Fitting

A mode-dependent change [40] was applied to N in Equation (5.8). Differences from fitting were obtained by Derrick Toth after examining the use of single-Gaussian convolved signal shapes, and are shown in Table 5.13. The changes applied were obtained from the sums of the mode-dependent values averaged over their efficiencies. As this is an overall scale change, the only variable significantly affected is $\Gamma_{ee}^{\psi(3770)\to D\overline{D}}$.

Tag Mode	Difference (%)
$D^0 \to K^- \pi^+$	0.27
$D^0 \to K^- \pi^+ \pi^0$	0.10
$D^0 \to K^- \pi^+ \pi^+ \pi^-$	0.47
D^0 Average: 0.25 %	
$D^+ \to K^- \pi^+ \pi^+$	0.20
$D^+ \to K^- \pi^+ \pi^+ \pi^0$	0.00
$D^+ \to K_S^0 \pi^+$	0.17
$D^+ \to K_S^0 \pi^+ \pi^0$	0.29
$D^+ \to K_S^0 \pi^+ \pi^+ \pi^-$	0.17
$D^+ \to K^+ K^- \pi^+$	0.74
D^+ Average: 0.20 %	

Table 5.13: Single-tag fitting differences by mode.
The total D^0 and D^+ values are averaged over the efficiencies for each mode.

PDG Branching Fractions

A mode-dependent change based on the PDG branching fraction errors (Table 5.9) was applied to ϵ_m in Equation (5.6). The branching fraction for each mode was changed by its uncertainty. As this is an overall scale change, the only variable significantly affected is $\Gamma_{ee}^{\psi(3770) \to D\overline{D}}$.

Meson Radii

The most uncertain parameters used in the analysis are the radii of the mesons $\psi(2S)$ and $\psi(3770)$. We take the same values as used by KEDR, however, each of these is quoted to have an ~25% uncertainty. With this, we adjust the two radii values up or down by 25% over the four possible combinations (both up, both down, and each opposite). The maximum deviations from the nominal method seen across all four cases is used as the systematic uncertainty. Due to the high level of uncertainty on these parameters, this effect provides one of the largest systematic sources in the analysis.

MC Iteration*

In generating MC for this analysis, the $D\overline{D}$ samples used a modified form of KKMC which generates events based off an input Born cross-section shape for the $\psi(3770)$.

However, as this shape is also the final output of the procedure, only an estimation of the results can be used for generation. To assess the variation from the input shape, we compared the output fit parameters to those used in the generation process. This process used the Exponential method, and the results are shown in Table 5.14. The numbers listed are from an earlier iteration of the MC than shown in Section 5.5, but the consistency seen is representative of all iterations. Very little difference is seen in the primary fitting parameters of the $\psi(3770)$. These similarities show the fit result values converging, even after only a single iteration. From this, we treat variations due to MC iteration as negligible.

Parameter		KKMC Input	Fit Results	Difference
$M^{\psi(3770)}$	[GeV]	3.7815 ± 0.0003	3.7814 ± 0.0003	0.0001
$\Gamma^{\psi(3770)}$	[MeV]	24.887 ± 0.686	24.839 ± 0.681	0.048
$\Gamma_{ee}^{\psi(3770) \to D\overline{D}}$	[eV]	217.55 ± 11.18	214.65 ± 11.10	2.90
$\phi^{\psi(3770)}$		3.6374 ± 0.0513	3.6375 ± 0.0518	0.0001
F_{NR}		21.394 ± 1.866	20.147 ± 1.765	0.992
a_{NR}		-1.6202 ± 0.5271	-1.5265 ± 0.5119	0.0937

Table 5.14: Comparison of input and output fit parameters.
The MC generation is done using the Exponential form factor model as an input Born cross section to generate $D\overline{D}$ events using KKMC.

MC ISR Generation*

To compare to the generation process of KKMC, we also generated alternative MC samples of $D\overline{D}$ using the ConExc ISR generator. This process used an input Born level shape identical to a previous iteration produced with KKMC. Each of the background samples used (such as $q\bar{q}$ and $\tau^-\tau^+$) were the same as in the nominal procedure. The cross section results using the VDM model are shown in Table 5.15, and provide $\psi(3770)$ fit parameters within the statistical errors of the nominal method. From this, we treat variations due to the MC ISR generator as negligible.

Parameter		ConExc Fit Results	KKMC Fit Results
$M^{\psi(3770)}$	[GeV]	3.7803 ± 0.0003	3.7804 ± 0.0003
$\Gamma^{\psi(3770)}$	[MeV]	23.784 ± 0.616	23.732 ± 0.612
$\Gamma_{ee}^{\psi(3770)\to D\overline{D}}$	[eV]	204.68 ± 10.28	207.35 ± 10.02
$\phi^{\psi(3770)}$		3.5954 ± 0.0559	3.5952 ± 0.0525
$\Gamma_{ee}^{\psi(2S)}$	[MeV]	12.229 ± 1.336	14.070 ± 1.431
F_0		-2.3415 ± 0.4898	-2.0768 ± 0.4924

Table 5.15: Comparison of output fit parameters between ISR generators. The MC generation is done using both the ConExc and KKMC generators and the final VDM fit results are shown. The values shown are from a previous iteration than the final results, but the output from each method remains very similar.

Intermediate Resonances*

In looking at the mode $D^+ \to K^- \pi^+ \pi^+$, we also analyzed the contribution of intermediate resonances, like the ρ^0. Using the $2.93\,\text{fb}^{-1}$ data sample of $\psi(3770)$ events at $E_\text{cm} = 3.773\,\text{GeV}$, we split the signal region of this mode based on a $1.0\,(\text{GeV})^2$ cut in both the invariant masses of $K\pi$ and $\pi\pi$ separately. These cuts were chosen to separate the sample into distinctly different regions, as can be seen in Figure 5.10. Fitting the signal distributions for each of these subsamples, we found no statistically significant deviations in the measured yields. From this, we treat variations due to intermediate resonances as negligible.
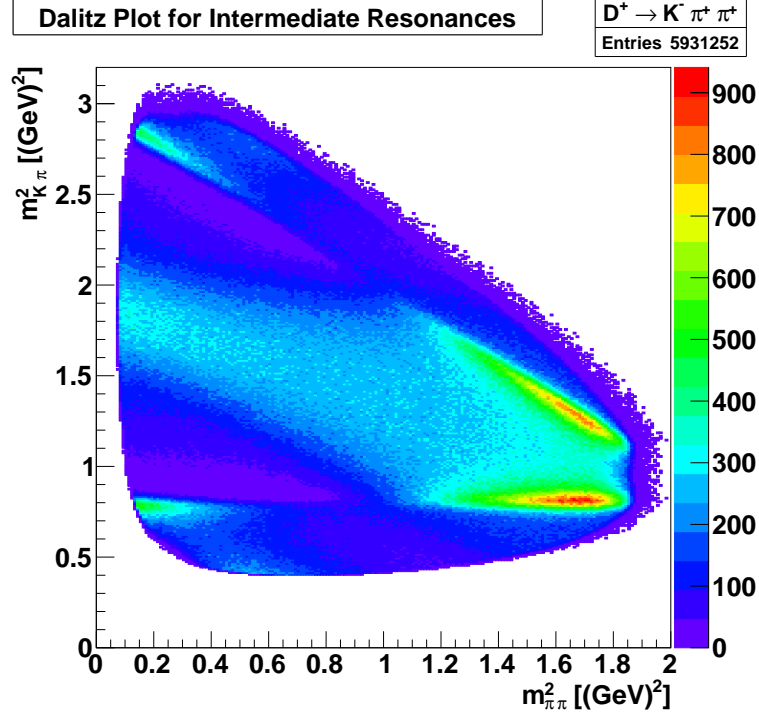
Figure 5.10: The $K\pi$ vs. $\pi\pi$ invariant masses for the mode $D^+ \to K^- \pi^+ \pi^+$. The data used are from the on-peak $\psi(3770)$ sample, as the statistics are significantly higher than for the scan data.

Non-Resonant Form Factor

In addition to the systematics described above, there is a significant source of uncertainty coming from the non-resonant form factor used. Each of the models examined, Exponential and VDM, provided quality fit results for the cross section shapes. From this, we conservatively assign an uncertainty equal to the differences in fit parameters provided by these two methods. Following the example of KEDR, we treat this as separate from the other systematics, and list it as a model uncertainty.

Systematic	$M^{\psi(3770)}$ [%]	$\Gamma^{\psi(3770)}$ [%]	$\Gamma_{ee}^{\psi(3770)\to D\overline{D}}$ [%]	$\phi^{\psi(3770)}$ [%]
Luminosity	0.000	0.004	1.005	0.014
$K^{\pm}/\pi^{\pm}$ Tracking	0.000	0.008	2.646	0.033
π^0 Tracking	0.000	0.012	0.746	0.028
K_S^0 Tracking	0.000	0.004	0.260	0.019
Single Tag Fits	0.000	0.012	0.213	0.008
PDG Errors	0.000	0.017	2.840	0.036
Meson Radii	0.016	2.411	3.512	1.477
Form Factor†	0.034	7.909	8.016	3.613
Total [%]	0.016	2.411	5.389	1.479
Relative Stat. Error [σ]	3.000	1.088	1.342	1.229

Table 5.16: Systematic uncertainties relative to the measured parameters of the $\psi(3770)$. †The Form Factor is treated as an uncertainty on the model, and is not included in the total systematic error.

5.6.2 Cross Section Systematics

In addition to the statistical uncertainties provided in Table 5.12, we also provide systematic uncertainties on the cross section measurements. These are calculated from the systematic shifts (ΔS) which affect Equation (5.8): Luminosity, $K^{\pm}/\pi^{\pm}$ Tracking, π^0 Tracking, K_S^0 Tracking, and Single Tag Fits. For the luminosity, this value is the same 1% shift used previously. The others are calculated by weighting the efficiency from each decay mode:

$$\Delta S = \frac{\sum_m \epsilon_m \Delta S_m}{\sum_m \epsilon_m} \qquad (5.9)$$

The value of ΔS_m for $K^{\pm}/\pi^{\pm}$ Tracking is 1.0% per $K^{\pm}$ or $\pi^{\pm}$ in each decay mode, and defined similarly for the other systematics using the previously listed values. The calculated shifts are listed in Table 5.17, and the resulting cross section values are listed in Table 5.18.

Systematic	ΔS (D^0) [%]	ΔS (D^+) [%]
Luminosity	1.00	1.00
$K^\pm/\pi^\pm$ Tracking	2.58	2.59
π^0 Tracking	0.94	0.63
K_S^0 Tracking	0.00	0.42
Single Tag Fits	0.25	0.20
PDG Error	0.31	0.18
Total	2.95	2.89

Table 5.17: Systematics shifts affecting the cross section measurements. The total shifts are used to calculate the systematic uncertainties of the D^0 and D^+ cross sections.

E_{mid} [GeV]	$\sigma^{RC}_{D^0\overline{D^0}}$ [nb]	$\sigma^{RC}_{D^+D^-}$ [nb]
3.7342	$0.164 \pm 0.046 \pm 0.005$	-
3.7368	$0.218 \pm 0.068 \pm 0.006$	-
3.7447	$0.765 \pm 0.070 \pm 0.023$	$0.150 \pm 0.038 \pm 0.004$
3.7483	$0.838 \pm 0.064 \pm 0.025$	$0.360 \pm 0.048 \pm 0.010$
3.7501	$0.968 \pm 0.053 \pm 0.029$	$0.439 \pm 0.040 \pm 0.013$
3.7517	$1.237 \pm 0.052 \pm 0.036$	$0.574 \pm 0.040 \pm 0.017$
3.7534	$1.377 \pm 0.051 \pm 0.041$	$0.748 \pm 0.042 \pm 0.022$
3.7556	$1.566 \pm 0.055 \pm 0.046$	$0.797 \pm 0.045 \pm 0.023$
3.7562	$1.629 \pm 0.051 \pm 0.048$	$0.914 \pm 0.042 \pm 0.026$
3.7592	$1.948 \pm 0.052 \pm 0.057$	$1.192 \pm 0.045 \pm 0.034$
3.7624	$2.385 \pm 0.058 \pm 0.070$	$1.534 \pm 0.051 \pm 0.044$
3.7650	$2.715 \pm 0.071 \pm 0.080$	$1.882 \pm 0.066 \pm 0.054$
3.7676	$3.102 \pm 0.087 \pm 0.092$	$2.200 \pm 0.081 \pm 0.064$
3.7713	$3.406 \pm 0.101 \pm 0.100$	$2.634 \pm 0.098 \pm 0.076$
3.7742	$3.714 \pm 0.111 \pm 0.110$	$3.067 \pm 0.111 \pm 0.089$
3.7775	$3.692 \pm 0.111 \pm 0.109$	$3.078 \pm 0.111 \pm 0.089$
3.7802	$3.444 \pm 0.104 \pm 0.102$	$2.599 \pm 0.100 \pm 0.075$
3.7829	$2.791 \pm 0.090 \pm 0.082$	$2.206 \pm 0.088 \pm 0.064$
3.7869	$1.995 \pm 0.072 \pm 0.059$	$1.627 \pm 0.073 \pm 0.047$
3.7891	$1.361 \pm 0.058 \pm 0.040$	$1.178 \pm 0.062 \pm 0.034$
3.7926	$0.920 \pm 0.045 \pm 0.027$	$0.680 \pm 0.045 \pm 0.020$
3.7970	$0.562 \pm 0.037 \pm 0.017$	$0.414 \pm 0.039 \pm 0.012$
3.8003	$0.424 \pm 0.035 \pm 0.013$	$0.241 \pm 0.037 \pm 0.007$
3.8024	$0.325 \pm 0.038 \pm 0.010$	$0.236 \pm 0.043 \pm 0.007$
3.8070	$0.352 \pm 0.050 \pm 0.010$	$0.289 \pm 0.051 \pm 0.008$
3.8093	$0.233 \pm 0.050 \pm 0.007$	$0.132 \pm 0.055 \pm 0.004$
3.8135	$0.060 \pm 0.049 \pm 0.002$	$0.153 \pm 0.066 \pm 0.004$
3.8153	$0.056 \pm 0.051 \pm 0.002$	$0.089 \pm 0.063 \pm 0.003$
3.8229	$0.140 \pm 0.083 \pm 0.004$	$0.197 \pm 0.107 \pm 0.006$
3.8320	$0.069 \pm 0.086 \pm 0.002$	$0.046 \pm 0.099 \pm 0.001$
3.8390	$0.237 \pm 0.105 \pm 0.007$	$0.254 \pm 0.124 \pm 0.007$
3.8494	$0.186 \pm 0.104 \pm 0.005$	$0.186 \pm 0.118 \pm 0.005$
3.8555	$0.337 \pm 0.111 \pm 0.010$	$0.273 \pm 0.104 \pm 0.008$
3.8632	$0.340 \pm 0.127 \pm 0.010$	$0.099 \pm 0.091 \pm 0.003$

Table 5.18: Measurements of the D^0 / D^+ cross sections. The first errors are statistical and the second are systematic.

5.7 Results

After incorporating the systematic and model uncertainties, the total results for the main $\psi(3770)$ parameters are shown in Table 5.19. The results shown are from the VDM model, as we treat this as the nominal results. The Exponential model is used as a measure of uncertainty, however, the quality of fits found by this approach means it cannot be excluded as a viable option.

$M^{\psi(3770)}$	$3780.8 \pm 0.2 \pm 0.6 \pm 1.3$	[MeV]
$\Gamma^{\psi(3770)}$	$24.1 \pm 0.5 \pm 0.6 \pm 1.9$	[MeV]
$\Gamma_{ee}^{\psi(3770)\to D\overline{D}}$	$216 \pm 9 \pm 11 \pm 17$	[eV]
$\phi^{\psi(3770)}$	$207 \pm 3 \pm 3 \pm 7$	[°]

Table 5.19: Final results for the $\psi(3770)$ parameters.
The first error listed is statistical, the second is systematic, and the third is from the form factor model.

Additionally, since this analysis is based on an approach developed by the KEDR collaboration, a comparison to their results is also shown in table 5.20. For their measurement of $\Gamma_{ee}^{\psi(3770)}$, two solutions were found with very close χ^2 values, so both are quoted in their final results. With the larger statistics available at BESIII, no alternate solution was found during searches over the parameter space.

Method	$M^{\psi(3770)}$ [MeV]	$\Gamma^{\psi(3770)}$ [MeV]	$\Gamma_{ee}^{\psi(3770)\to D\overline{D}}$ [eV]
Exponential	$3782.1 \pm 0.3 \pm 0.6$	$26.0 \pm 0.6 \pm 0.7$	$233 \pm 10 \pm 13$
VDM	$3780.8 \pm 0.2 \pm 0.6$	$24.1 \pm 0.6 \pm 0.6$	$216 \pm 9 \pm 12$
KEDR	$3779.2^{+1.8+0.5+0.3}_{-1.7-0.7-0.3}$	$24.9^{+4.6+0.5+0.2}_{-4.0-0.6-0.9}$	$154^{+79+17+13}_{-58-9\ -25}$, $414^{+72+24+90}_{-80-26-10}$
PDG	3773.15 ± 0.33	27.2 ± 0.9	$[262 \pm 18] \times \mathcal{B}_{D\overline{D}}$

Table 5.20: Fit results compared to the KEDR results and the PDG.
The first errors listed are statistical, while the second are systematic. In the case of KEDR, the third error is from the model.

We can also compare our results to the cross section values found in the previous analysis of BESIII's on-peak $\psi(3770)$ data sample of $2.93\,\text{fb}^{-1}$ by Derrick Toth [40]. The values displayed on Figures 5.6 and 5.7 are his double-tag (DT) values. Each of these cross sections are shown in Table 5.21. Further analysis to better understand

the differences seen is still in progress, however both methods used in this analysis are within $\sim 1\sigma$ of the high statistics method.

Model	$\sigma_{D^0\overline{D^0}}$ [nb]	$\sigma_{D^+D^-}$ [nb]
Derrick (DT)	$3.615 \pm 0.010 \pm 0.035$	$2.830 \pm 0.011 \pm 0.026$
Exponential	$3.662 \pm 0.131 \pm 0.108$	$2.947 \pm 0.118 \pm 0.085$
VDM	$3.748 \pm 0.131 \pm 0.111$	$2.951 \pm 0.118 \pm 0.085$

Table 5.21: Comparison of cross section calculations at $E_{\mathrm{cm}} = 3.7732\,\mathrm{GeV}$
The values measured previously used a $2.93\,\mathrm{fb}^{-1}$ data sample of $\psi(3770)$ events to reconstruct double-tag (DT) decays. The first errors listed are statistical, while the second is systematic.

Chapter 6

Measurement of Hadronic Production and $\Gamma(\psi(3770) \to \text{non-}D\overline{D})$

6.1 Data and Monte Carlo Samples

6.1.1 Data Samples

The data used for this analysis was also produced by BEPCII and collected by BESIII. The samples used include continuum data taken at $3.650\,\text{GeV}$ in 2009, as well as multiple other continuum points taken around this energy in 2013. We also use Round 1 (R1) and Round 2 (R2) of the high-statistics $\psi(3770)$ data taken in 2010 and 2011, respectively. Each of these samples, and their measured luminosities, can be seen in Table 6.1. The values of luminosity were measured during a previous version of this analysis using the procedure described in Section 5.2.3. The labels given to each continuum point are the intended energy targets, but may differ from their true values. In addition to these datasets, the scan data described previously (Section 5.2.1) is also used.

6.1.2 Center-of-Mass Energy Measurement

As before, a precise measurement of each energy point is vital to the accuracy of the final results. Most notably, due to the rapidly increasing shape of the $\psi(2S)$ cross section

near the high end of the continuum points, the value of the 3671 (New) point has a dramatic effect on the $q\bar{q}$ extrapolation. Following the procedure of Section 5.2.2, we measured the E_{cm} value of each continuum point. This resulted in a $4\,\mathrm{MeV}$ to $6\,\mathrm{MeV}$ shift downwards for each of the new continuum points, but virtually no shift for the old continuum point. The energy measurements are shown in Table 6.1.

Sample Name	E_{cm} [GeV]	Luminosity pb^{-1}
3500 (New)	3.496	3.680 ± 0.009
3542 (New)	3.538	3.481 ± 0.009
3600 (New)	3.596	0.395 ± 0.019
3650 (New)	3.644	5.420 ± 0.009
3671 (New)	3.665	4.669 ± 0.009
3650 (Old)	3.650	44.334 ± 0.009
3773 (R1)	3.773	926.922 ± 0.092
3773 (R2)	3.773	1978.920 ± 0.091

Table 6.1: Data samples used for the inclusive measurement.
While the 3600 (New) sample was intended to be similar in luminosity to the other continuum points, accelerator issues inhibited the data collection procedure. There is also a sizable difference in total luminosity between the new continuum points and the other datasets used in this analysis.

6.2 Event Selection

In order to select the number of hadronic events in each sample, we apply a variety of cuts. For charged tracks in the MDC, these include the cuts shown in Table 6.2.

Vertex (xy)	$V_{xy} < 1\,\mathrm{cm}$
Vertex (z)	$|Vz| < 10\,\mathrm{cm}$
MDC Angle	$|\cos\theta| < 0.93$

Table 6.2: Selection cuts on charged tracks used to count hadronic events.

For neutral tracks in the EMC, these include the cuts shown in Table 6.3.

Minimum Energy (Barrel)	$E_{\mathrm{EMC}} > 25\,\mathrm{MeV}$	$(|\cos\theta| < 0.80)$
Minimum Energy (Endcap)	$E_{\mathrm{EMC}} > 50\,\mathrm{MeV}$	$(0.86 < |\cos\theta| < 0.92)$
TDC Timing	$(0 \leq t \leq 14) \times 50\,\mathrm{ns}$	

Table 6.3: Selection cuts on neutral tracks used to count hadronic events.

To reject background events of $e^+e^- \to e^+e^-$ or $e^+e^- \to \gamma\gamma$, we also employ cuts related to the most energetic and highest momentum tracks in the event. These are listed in Table 6.4.

Highest Energy	$\cos\theta_+^{\max} < 0.8$ $\cos\theta_-^{\max} > -0.8$	$(N_{\text{tracks}} = 2)$
	$\cos\theta_+^{\max} < 0.8$ or $(p/E_{\text{cm}})_+^{\max} \leq 0.3$ $\cos\theta_-^{\max} > -0.8$ or $(p/E_{\text{cm}})_-^{\max} \leq 0.3$	$(N_{\text{tracks}} = 3, 4)$
Highest Momentum	$0.8 \leq (E_{\text{EMC}}/p)_+^{\max} \leq 1.1$ $0.8 \leq (E_{\text{EMC}}/p)_-^{\max} \leq 1.1$	

Table 6.4: Selection cuts to remove Bhabha and two-photon backgrounds. The $_+$ and $_-$ denote positively and negatively charged tracks, respectively. The $^{\max}$ notation indicates the highest energy or momenta track for the corresponding charge. The energy cuts depend on the total number of charged tracks in the event, N_{tracks}.

After applying these sets of cuts, there are three groups of cuts which are considered: Standard (SHAD), Loose (LHAD), and Tight (THAD). For the nominal procedure, SHAD is used, while LHAD and THAD are for systematic consideration. The cuts included in each of these sets are shown in Tables 6.5 to 6.7. These apply to the number of charged tracks (N_{tracks}), the visible energy (E_{vis}), the total visible momentum in the z-direction ($p_{z\,\text{vis}}$), the maximum shower energy ($E_{\text{EMC}}^{\max}$), and the total shower energy ($E_{\text{EMC}}^{\text{tot}}$). Here, 'visible' refers to the sum over charged and neutral tracks.

Number of Tracks	$N_{\text{tracks}} > 2$	
Visible Energy	$(E_{\text{vis}}/E_{\text{cm}}) > 0.3$	
Visible Momentum	$(p_{z\,\text{vis}}/E_{\text{vis}}) < 0.6$	$(N_{\text{tracks}} = 3, 4)$
Maximum Shower Energy	$(E_{\text{EMC}}^{\max}/E_{\text{beam}}) < 0.75$	$(N_{\text{tracks}} = 3, 4)$
Total Shower Energy	$0.25 < (E_{\text{EMC}}^{\text{tot}}/E_{\text{cm}}) < 0.75$	$(N_{\text{tracks}} = 3)$
	$0.15 < (E_{\text{EMC}}^{\text{tot}}/E_{\text{cm}}) < 0.75$	$(N_{\text{tracks}} = 4)$

Table 6.5: Standard selection cuts (SHAD) for counting hadronic events.

Number of Tracks	$N_{\text{tracks}} > 1$	
Visible Energy	$(E_{\text{vis}}/E_{\text{cm}}) > 0.4$	$(N_{\text{tracks}} = 2)$
	$(E_{\text{vis}}/E_{\text{cm}}) > 0.3$	$(N_{\text{tracks}} \geq 3)$
Visible Momentum	$(p_{z\,\text{vis}}/E_{\text{vis}}) < 0.3$	$(N_{\text{tracks}} = 2)$
	$(p_{z\,\text{vis}}/E_{\text{vis}}) < 0.6$	$(N_{\text{tracks}} = 3, 4)$
Maximum Shower Energy	$(E_{\text{EMC}}^{\max}/E_{\text{beam}}) < 0.50$	$(N_{\text{tracks}} = 2)$
	$(E_{\text{EMC}}^{\max}/E_{\text{beam}}) < 0.75$	$(N_{\text{tracks}} = 3, 4)$
Total Shower Energy	$0.25 < (E_{\text{EMC}}^{\text{tot}}/E_{\text{cm}}) < 0.75$	$(N_{\text{tracks}} = 2, 3)$
	$0.15 < (E_{\text{EMC}}^{\text{tot}}/E_{\text{cm}}) < 0.75$	$(N_{\text{tracks}} = 4)$

Table 6.6: Loose selection cuts (LHAD) for counting hadronic events.

Number of Tracks	$N_{\text{tracks}} > 3$	
Visible Energy	$(E_{\text{vis}}/E_{\text{cm}}) > 0.4$	
Visible Momentum	$(p_{z\,\text{vis}}/E_{\text{vis}}) < 0.6$	$(N_{\text{tracks}} = 4)$
Maximum Shower Energy	$(E_{\text{EMC}}^{\max}/E_{\text{beam}}) < 0.75$	$(N_{\text{tracks}} = 4, 5)$
Total Shower Energy	$0.15 < (E_{\text{EMC}}^{\text{tot}}/E_{\text{cm}}) < 0.75$	$(N_{\text{tracks}} = 4)$
	$0.00 < (E_{\text{EMC}}^{\text{tot}}/E_{\text{cm}}) < 0.75$	$(N_{\text{tracks}} = 5)$

Table 6.7: Tight selection cuts (THAD) for counting hadronic events.

6.3 Background Subtraction

6.4 Efficiency Extrapolation

6.5 $D\overline{D}$ Correction

6.6 Hadron Counting

6.7 Results

Chapter 7

Conclusion

This is where the Conclusions go!

References

[1] K.A. Olive et al. (Particle Data Group), Chin. Phys. C, **38**, 090001 (2014).

[2] Wikimedia Commons. Standard model of elementary particles. 2006.

[3] C. S. Wu, E. Ambler, R. W. Hayward, D. D. Hoppes, and R. P. Hudson Phys. Rev. **105**, 1413 (1957).

[4] J. H. Christenson, J. W. Cronin, V. L. Fitch, and R. Turlay Phys. Rev. Lett. **13**, 138 (1964).

[5] M. Ablikim et al. (BESIII Collaboration) Phys. Rev. Lett. **110**, 252001 (2013).

[6] Z. Q. Liu et al. (Belle Collaboration) Phys. Rev. Lett. **110**, 252002 (2013).

[7] R. Aaij et al. (LHCb Collaboration) Phys. Rev. Lett. **115**, 072001 (2015).

[8] M. Kobayashi and T. Maskawa, "CP-Violation in the Renormalizable Theory of Weak Interaction". Prog. Theor. Phys. 1973; 49 (2): 652-657. [doi: 10.1143/PTP.49.652]

[9] S. L. Glashow, J. Iliopoulos, and L. Maiani Phys. Rev. D **2**, 1285 (1970).

[10] B. Pontecorvo. (1957). "Inverse beta processes and nonconservation of lepton charge". Zhurnal ksperimentalno i Teoretichesko Fiziki. **34**: 247. reproduced and translated in Soviet Physics JETP. 7: 172. 1958.

[11] Z. Maki, M. Nakagawa, S. Sakata. (1962). "Remarks on the Unified Model of Elementary Particles". Progress of Theoretical Physics. **28**: 870.

[12] J. L. Rosner, Phys. Rev. D **64**, 094002 (2001) [hep-ph/0105327].

[13] J. L. Rosner, Annals Phys. **319**, 1 (2005) [hep-ph/0411003].

[14] S. Okubo, Phys. Lett. **5**, 165 (1963).

[15] G. Zweig, Developments in the Quark Theory of Hadrons, Volume 1. Edited by D. Lichtenberg and S. Rosen. pp. 22-101

[16] J. Iizuka, K. Okada and O. Shito, Prog. Theor. Phys. **35**, 1061 (1966).

[17] E. A. Kuraev and V. S. Fadin, Sov. J. Nucl. Phys. **41**, 466 (1985) [Yad. Fiz. **41**, 733 (1985)].

[18] V. V. Anashin *et al.*, Phys. Lett. B **711**, 292 (2012) [arXiv:1109.4205 [hep-ex]].

[19] J. M. Blatt and V. F. Weisskopf, Theoretical Nuclear Physics, Wiley, New York, (1952).

[20] M. Ablikim *et al.* [BESIII Collaboration], Nucl. Instrum. Meth. A **614**, 345 (2010) [arXiv:0911.4960 [physics.ins-det]].

[21] J. D. Jackson. *Classical Electrodynamics (3rd ed.)*. Wiley. (Section 13.2)

[22] W. Li, *et al.*, Proc. Int. Conf. Comput. High Energy and Nucl. Phys. 225 (2006).

[23] See `http://linux.web.cern.ch/linux/scientific5`.

[24] G. Barrand, I. Belyaev, P. Binko, M. Cattaneo, R. Chytracek, G. Corti, M. Frank and G. Gracia *et al.*, Comput. Phys. Commun. **140**, 45 (2001).

[25] C. Arnault, "CMT: A software configuration management tool," (2000).

[26] See `http://root.cern.ch`.

[27] S. Agostinelli, *et al.*, Nucl. Instr. and Meth. **506**, (3), 250 (2003); J. Allison, *et al.*, IEEE Trans. Nucl. Sci. NS **53** (1), 270 (2006); See `http://www.geant4.org/geant4`.

[28] S. Jadach , B. F. L. Ward and Z. Was, Comp. Phys. Commun. **130**, 260 (2000); S. Jadach, B. F. L. Ward and Z. Was, Phys. Rev. D **63**, 113009 (2001).

[29] S. Jadach, Z. Was, R. Decker and J. H. Kuhn, Comput. Phys. Commun. **76**, 361 (1993).

[30] See http://home.thep.lu.se/~torbjorn/Pythia.html.

[31] D.J. Lange, Nucl. Instrum. Meth. A **462**, 152 (2001).

[32] R. G. Ping, Chinese Physics C **32**, 8 (2008).

[33] E. Barberio, B. van Eijk and Z. Was, Comput. Phys. Commun. **66**, 115 (1991).

[34] J. C. Chen, G. S. Huang, X. R. Qi, D. H. Zhang and Y. S. Zhu, Phys. Rev. D **62**, 034003 (2000).

[35] G. Bonneau and F. Martin, Nucl. Phys. B **27**, 381 (1971).

[36] C.M. Carloni Calame, G. Montagna, O. Nicrosini, F. Piccinini, Nucl. Phys. Proc. Suppl. **131** 48-55 (2004).

[37] See http://www.mysql.com/about.

[38] R. M. Baltrusaitis *et al.* [MARK-III Collaboration], Phys. Rev. Lett. **56**, 2140 (1986).

[39] J. Adler *et al.* [MARK-III Collaboration], Phys. Rev. Lett. **60**, 89 (1988).

[40] D. Toth. (2014). "Measurement of Non-$D\overline{D}$ Decays of the $\psi(3770)$ Resonance at BESIII".

[41] L. Dong, "Center-of-mass beam energy calibration for psi(3770) data with BOSS 6.6.4," BESIII-doc-284-v6 (2014).

[42] A. Hafner, "Luminosity Measurement for the $\psi(3770)$ data at BESIII," BESIII-doc-406-v2 (2015).

[43] D. M. Asner and W. M. Sun, Phys. Rev. D, **77**, 019901 (2008).

[44] HFAG 2015 (CPV-Allowed) [http://www.slac.stanford.edu/xorg/hfag/charm/CHARM15/results_mi

[45] T. Evans et al., Physics Letters B 757 (2016) 520527.

[46] M. Ablikim et al. [BESIII Collaboration], Chin. Phys. C, **37**, 12 (2013):12300.

[47] G. Rong et. al, "Measurements of Branching Fractions and Form Factors for $D^0 \to K^- e^+ \nu_e$, $\pi^- e^+ \nu_e$ Decays", BESIII-doc-125-v3 (2015).

[48] B. C. Ke et al. [Carnegie Mellon University], "π^0 Reconstruction Efficiency", BESIII-doc-446-v4 (2015).

[49] T. Ma , "Determination of K_S^0 Systematics", BESIII-doc-125-v3 (2014).

Appendix A

Glossary and Acronyms

Care has been taken in this thesis to minimize the use of jargon, but this cannot always be achieved. This appendix defines certain terms used in a glossary, and contains a table of acronyms and initialisms used along with their meanings.

A.1   Glossary

A.2   Acronyms / Initialisms

Table A.1: Acronyms and Initialisms

Name	Meaning
BESIII	The third Beijing Spectrometer
IHEP	Institute of High Energy Physics
BEPCII	The second Beijing Electron-Position Collider
MDC	Multi-Layer Drift Chamber
ToF	Time-of-Flight System
EMC	Electromagnetic Calorimeter
MUC	Muon Identifier
PMTs	Photomultipler Tubes
	Continued on next page

Table A.1 – Continued from previous page

Acronym	Meaning
RPC	Resistive Plate Counter
ISR	Initial State Radiation
FSR	Final State Radiation
BOSS	BESIII Offline Software System
MC	Monte Carlo
ADC	Analog-to-Digital Conversion
TDC	Time-to-Digital Conversion

Appendix B

D^0 Signal Fits

Signal Fit - D^0 Bin 0
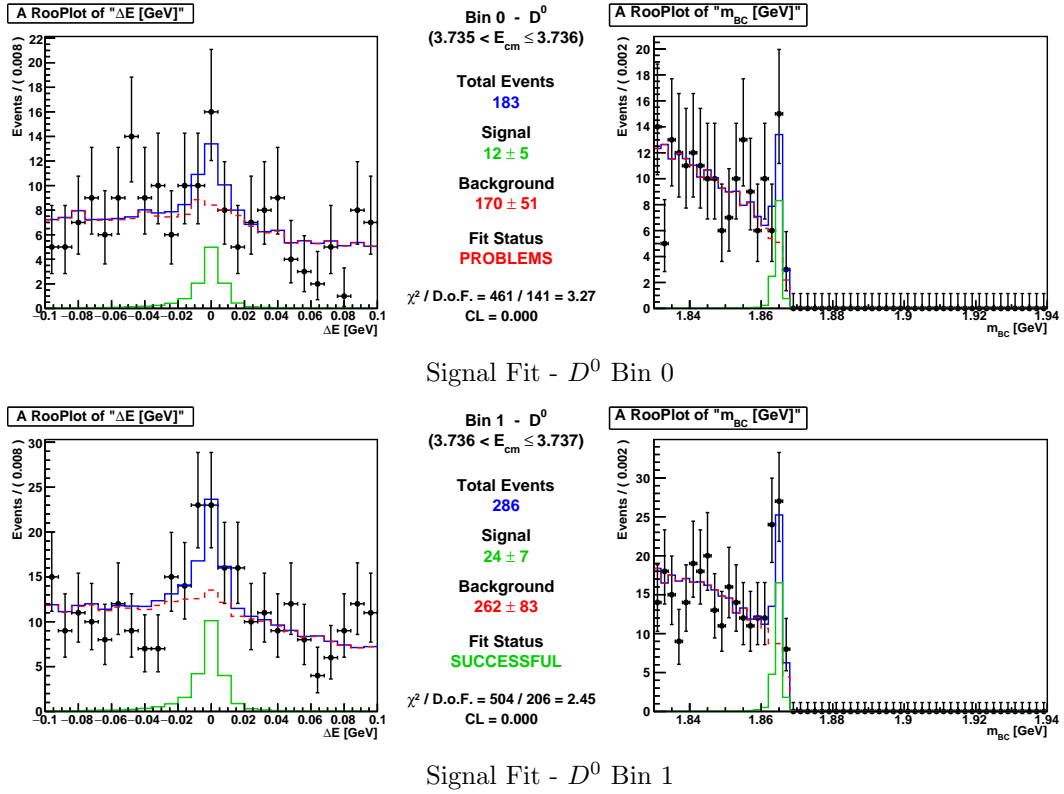
Signal Fit - D^0 Bin 1

Figure B.1: Signal Fitting Plots for D^0 Bins 0 - 1.

Bin 2 - D⁰
(3.737 < E_cm ≤ 3.744)

Total Events
174

Signal
15 ± 5

Background
158 ± 53

Fit Status
SUCCESSFUL

χ^2 / D.o.F. = 551 / 134 = 4.11
CL = 0.000

Signal Fit - D^0 Bin 2

Bin 3 - D⁰
(3.744 < E_cm ≤ 3.746)

Total Events
650

Signal
166 ± 15

Background
483 ± 152

Fit Status
SUCCESSFUL

χ^2 / D.o.F. = 502 / 323 = 1.56
CL = 0.000

Signal Fit - D^0 Bin 3

Bin 4 - D⁰
(3.746 < E_cm ≤ 3.748)

Total Events
1070

Signal
266 ± 20

Background
803 ± 236

Fit Status
SUCCESSFUL

χ^2 / D.o.F. = 647 / 407 = 1.59
CL = 0.000

Signal Fit - D^0 Bin 4

Bin 5 - D⁰
(3.748 < E_cm ≤ 3.750)

Total Events
1935

Signal
508 ± 27

Background
1426 ± 373

Fit Status
SUCCESSFUL

χ^2 / D.o.F. = 557 / 489 = 1.14
CL = 0.018

Signal Fit - D^0 Bin 5

Figure B.2: Signal Fitting Plots for D^0 Bins 2 - 5.
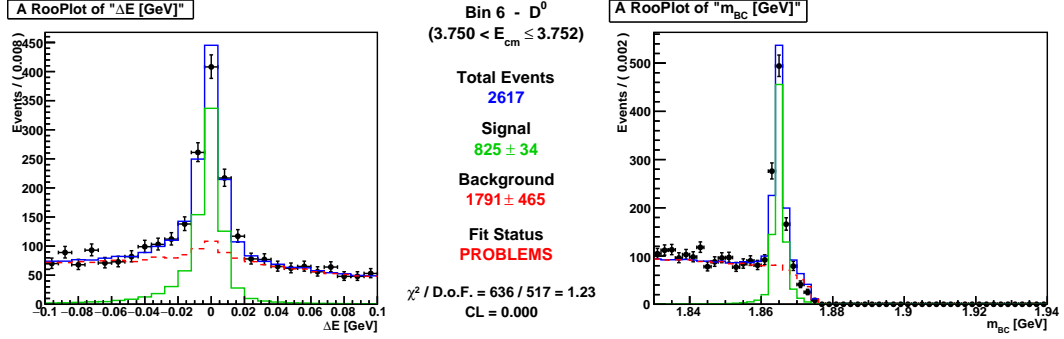
Signal Fit - D^0 Bin 6
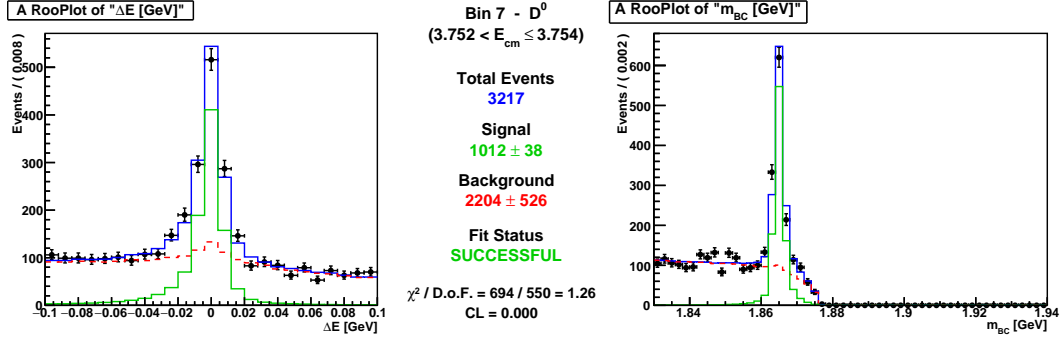
Signal Fit - D^0 Bin 7
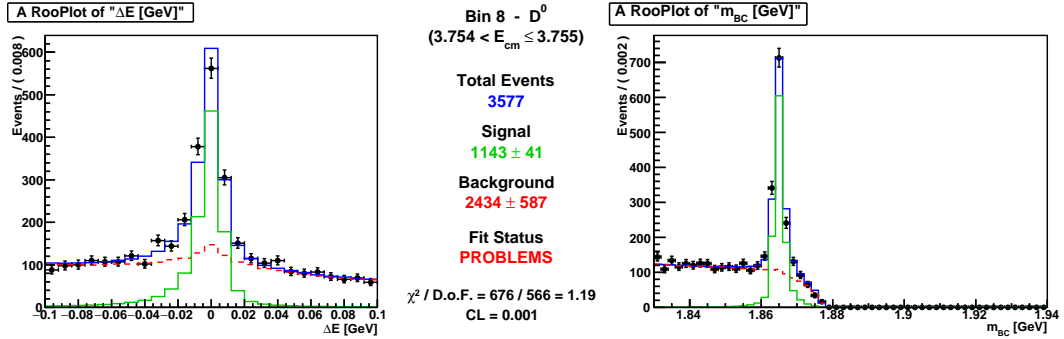
Signal Fit - D^0 Bin 8
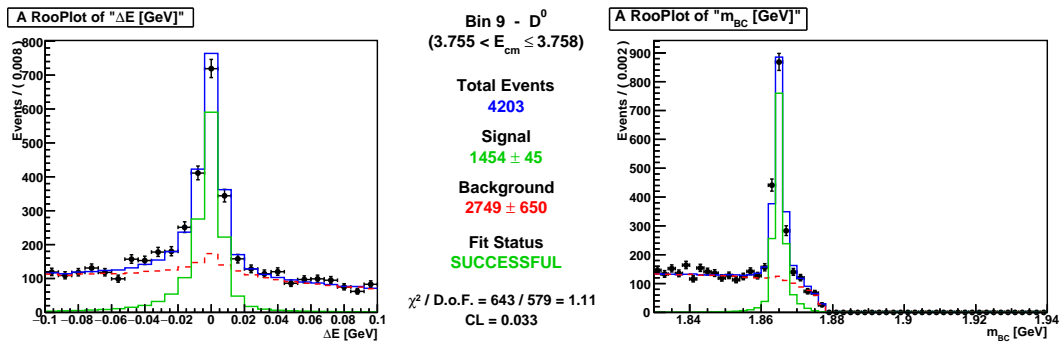

Signal Fit - D^0 Bin 9
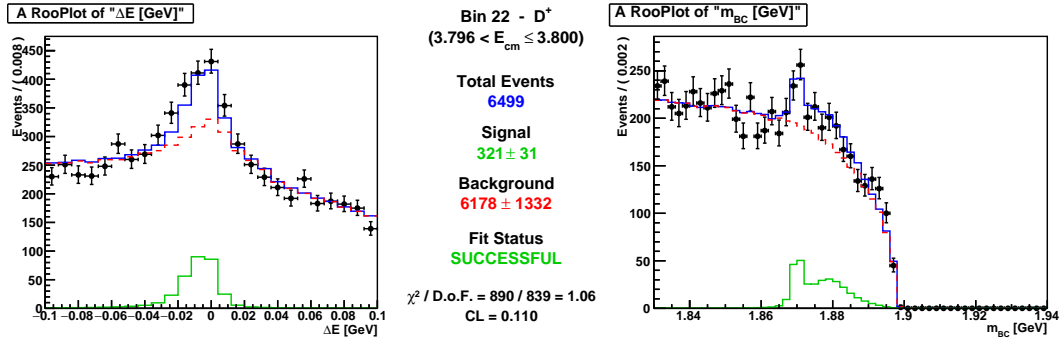
Figure B.3: Signal Fitting Plots for D^0 Bins 6 - 9.
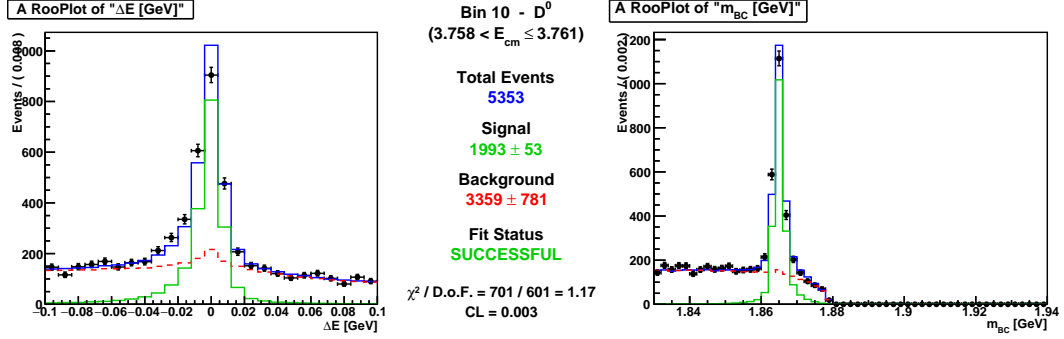
Signal Fit - D^0 Bin 10
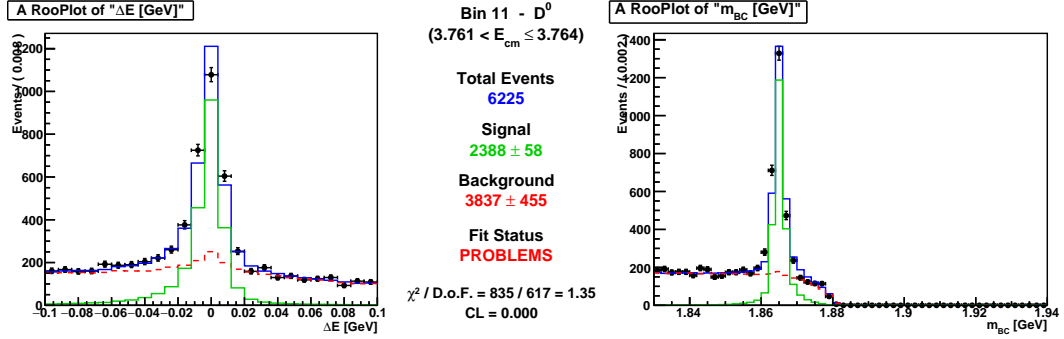
Signal Fit - D^0 Bin 11
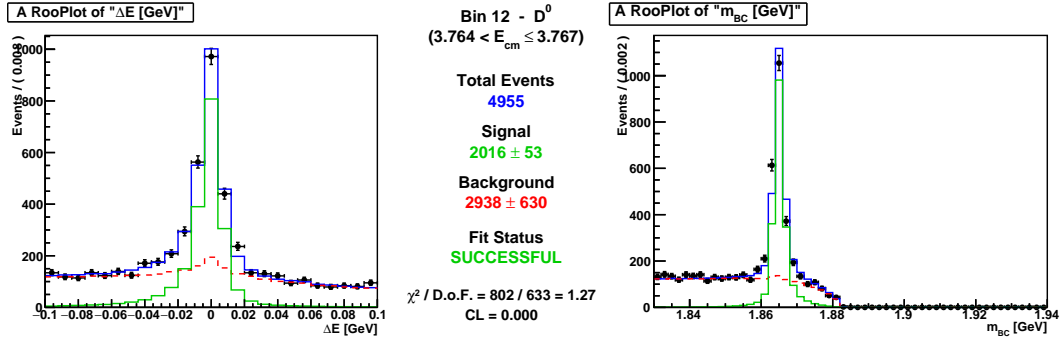

Signal Fit - D^0 Bin 12
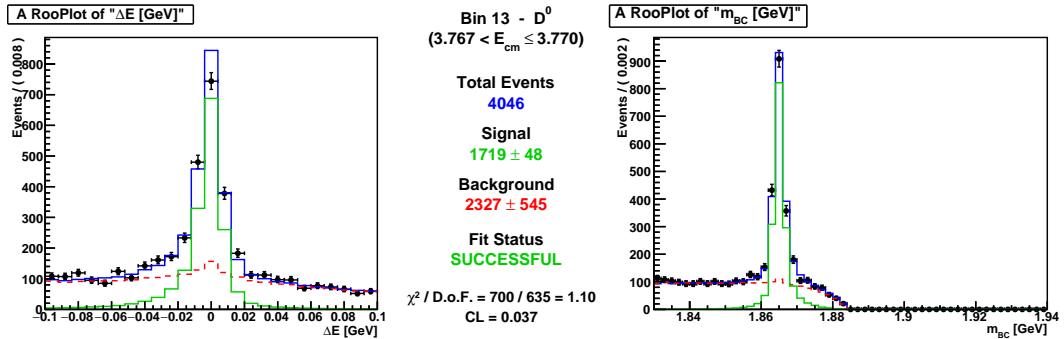
Signal Fit - D^0 Bin 13

Figure B.4: Signal Fitting Plots for D^0 Bins 10 - 13.

Bin 14 - D⁰
$(3.770 < E_{cm} \leq 3.773)$

Total Events
3657

Signal
1578 ± 46

Background
2079 ± 494

Fit Status
SUCCESSFUL

χ^2 / D.o.F. = 734 / 628 = 1.17
CL = 0.002

Signal Fit - D^0 Bin 14

Bin 15 - D⁰
$(3.773 < E_{cm} \leq 3.776)$

Total Events
3585

Signal
1561 ± 46

Background
2024 ± 328

Fit Status
SUCCESSFUL

χ^2 / D.o.F. = 753 / 643 = 1.17
CL = 0.002

Signal Fit - D^0 Bin 15

Bin 16 - D⁰
$(3.776 < E_{cm} \leq 3.779)$

Total Events
3619

Signal
1543 ± 45

Background
2076 ± 462

Fit Status
SUCCESSFUL

χ^2 / D.o.F. = 793 / 659 = 1.20
CL = 0.000

Signal Fit - D^0 Bin 16

Bin 17 - D⁰
$(3.779 < E_{cm} \leq 3.782)$

Total Events
3739

Signal
1522 ± 46

Background
2217 ± 486

Fit Status
SUCCESSFUL

χ^2 / D.o.F. = 820 / 688 = 1.19
CL = 0.000

Signal Fit - D^0 Bin 17

Figure B.5: Signal Fitting Plots for D^0 Bins 14 - 17.
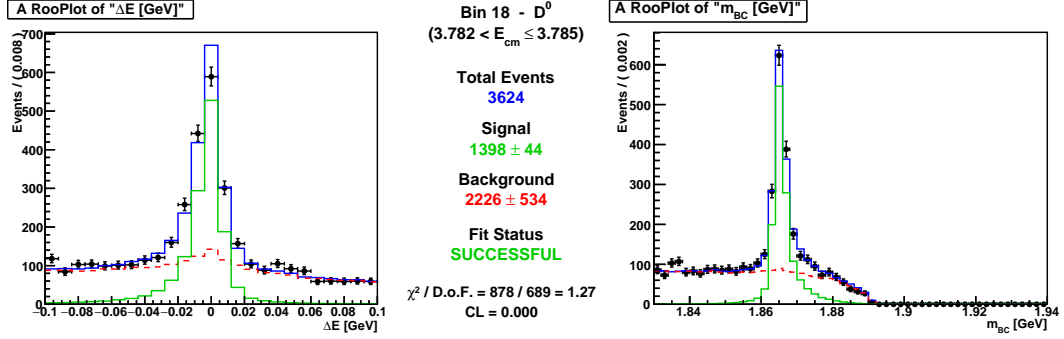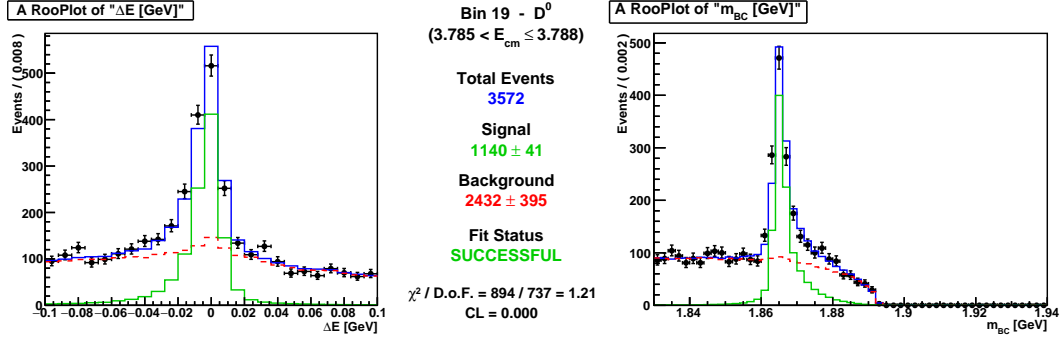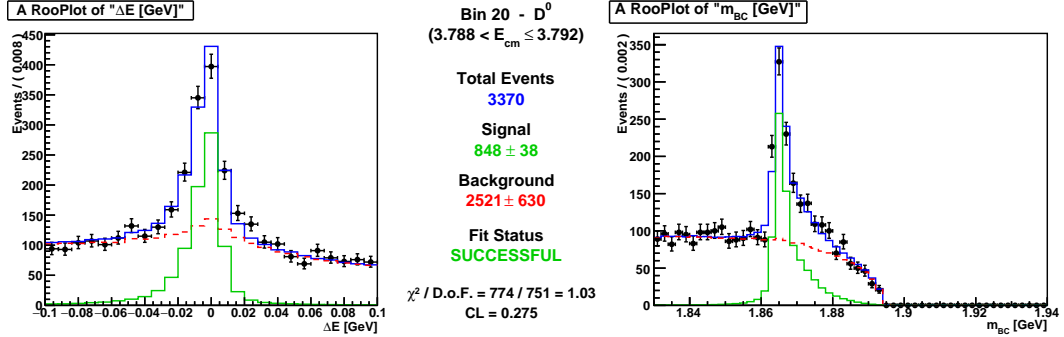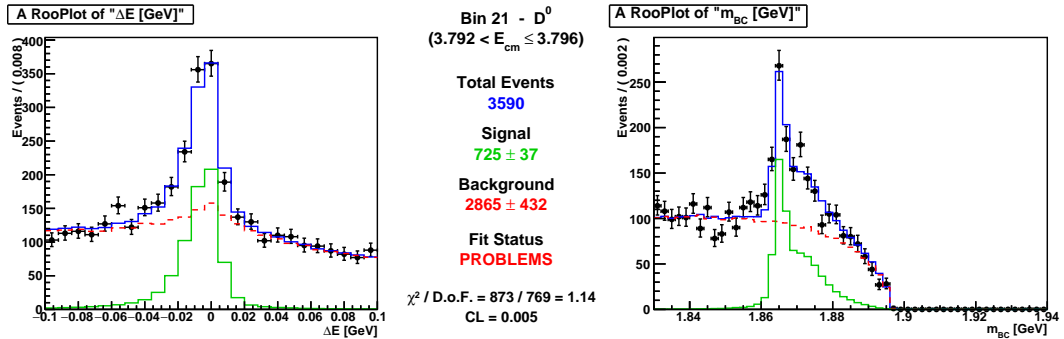
Figure B.6: Signal Fitting Plots for D^0 Bins 18 - 21.
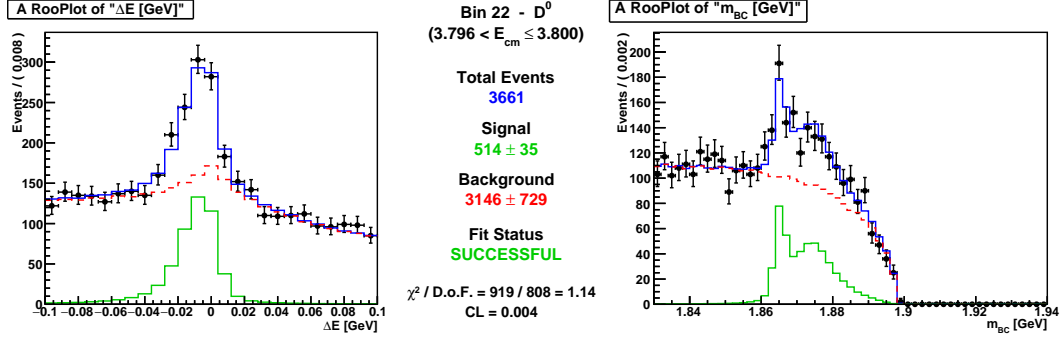
Signal Fit - D^0 Bin 22
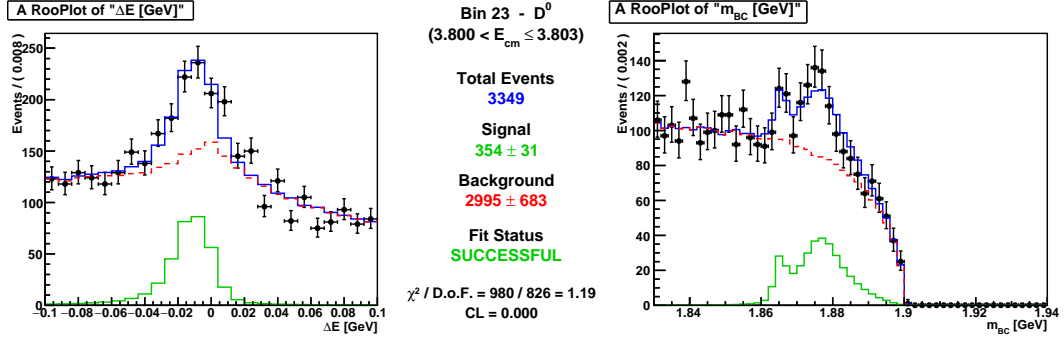
Signal Fit - D^0 Bin 23
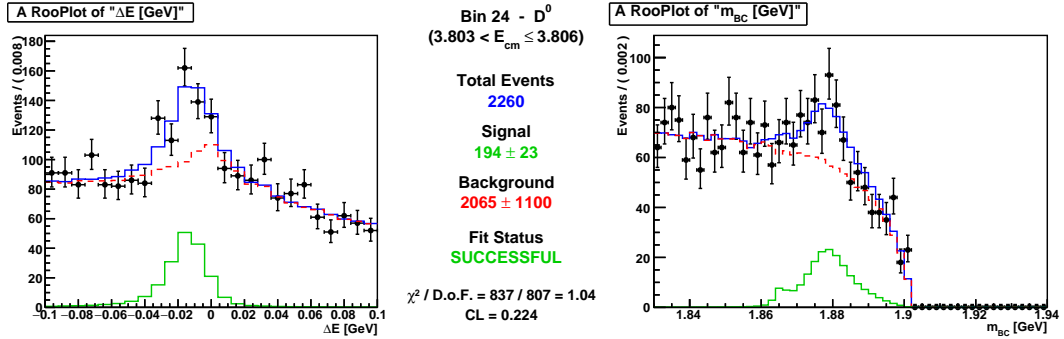
Signal Fit - D^0 Bin 24
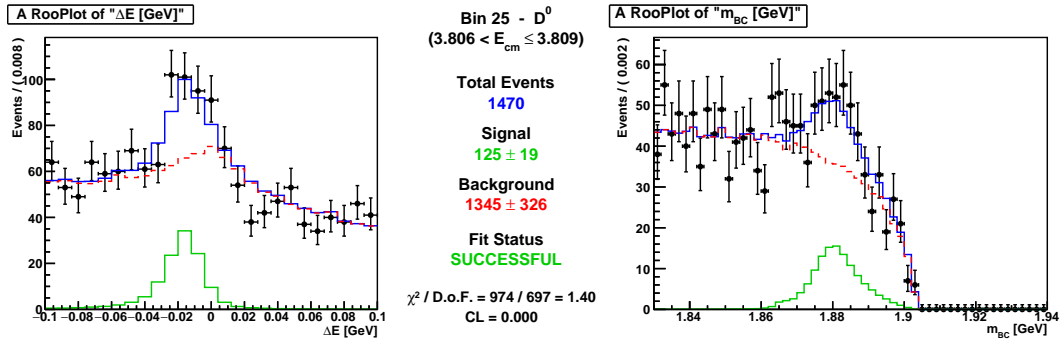
Signal Fit - D^0 Bin 25

Figure B.7: Signal Fitting Plots for D^0 Bins 22 - 25.
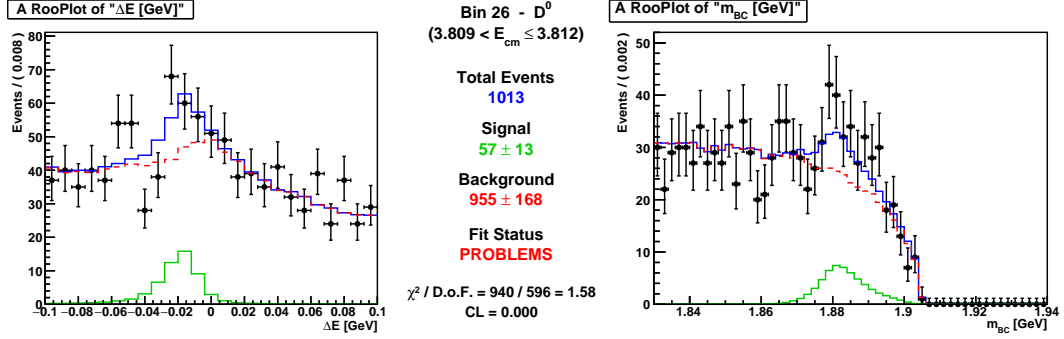
Signal Fit - D^0 Bin 26
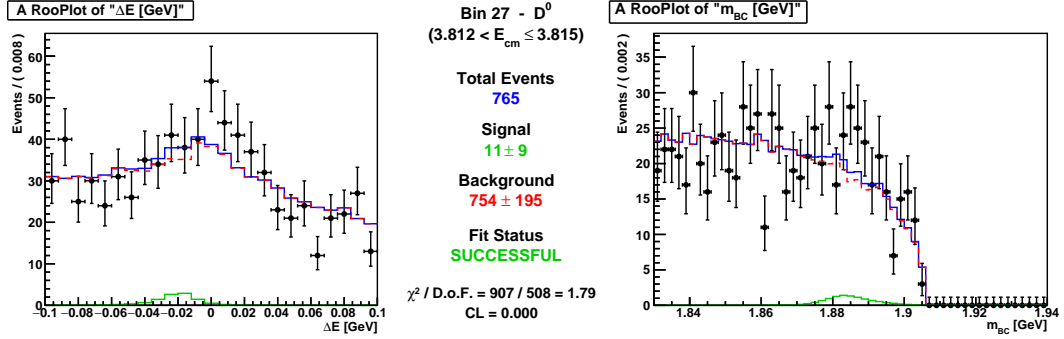
Signal Fit - D^0 Bin 27
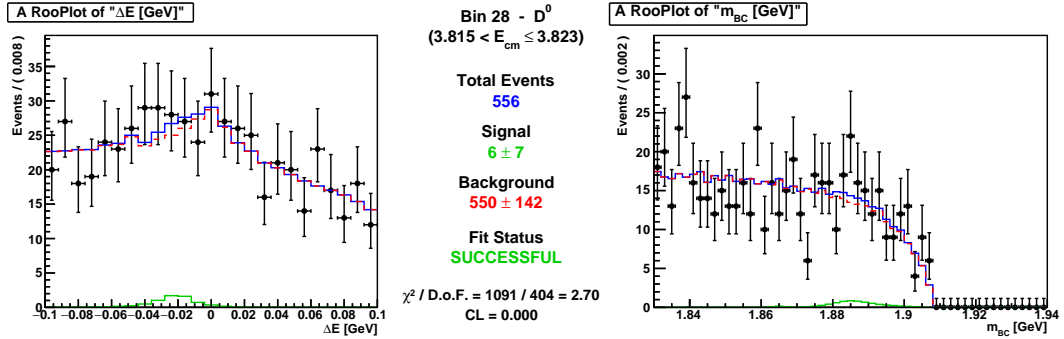
Signal Fit - D^0 Bin 28
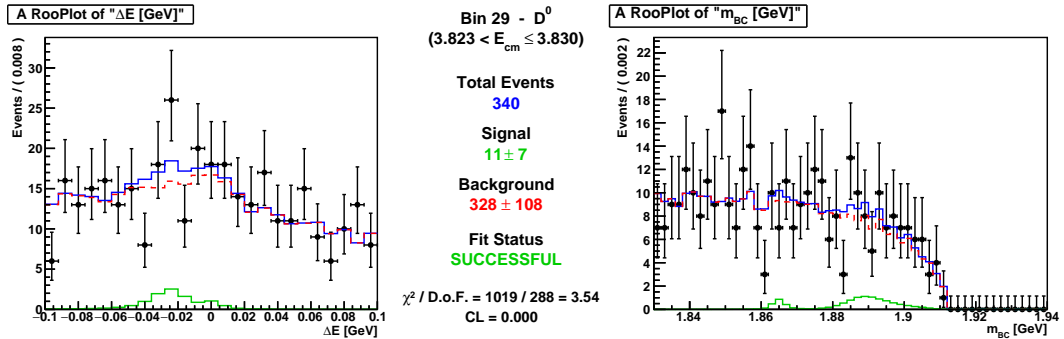
Signal Fit - D^0 Bin 29

Figure B.8: Signal Fitting Plots for D^0 Bins 26 - 29.
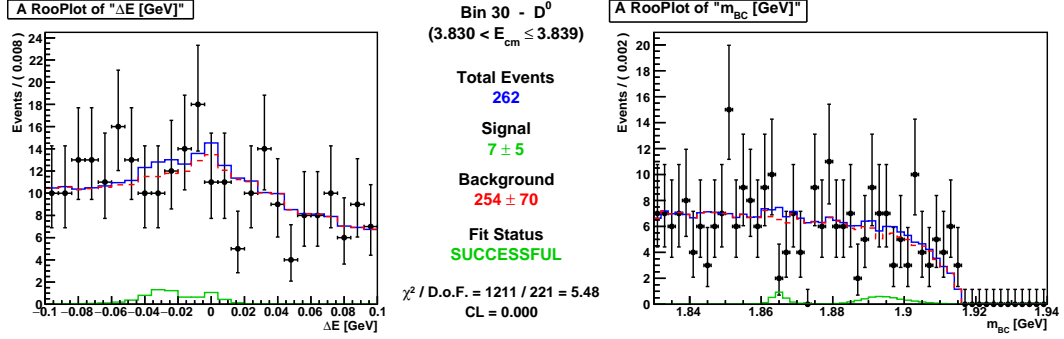
Signal Fit - D^0 Bin 30
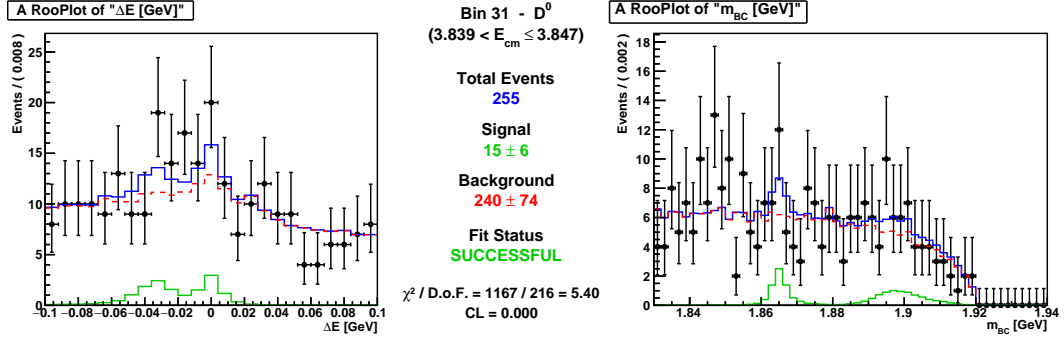
Signal Fit - D^0 Bin 31
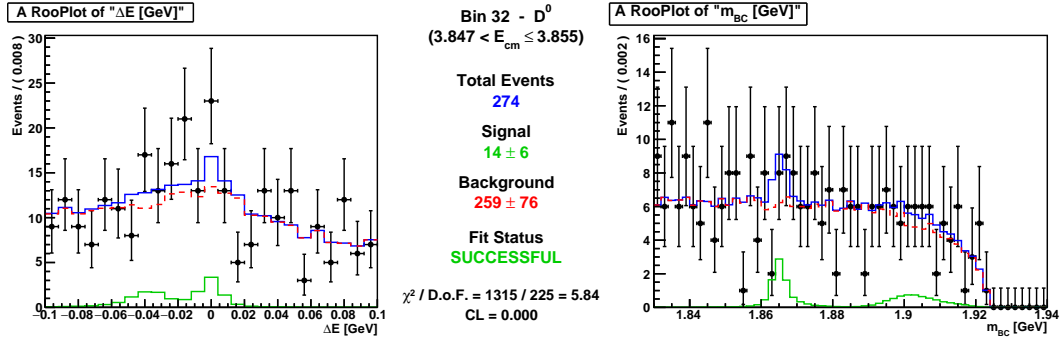
Signal Fit - D^0 Bin 32
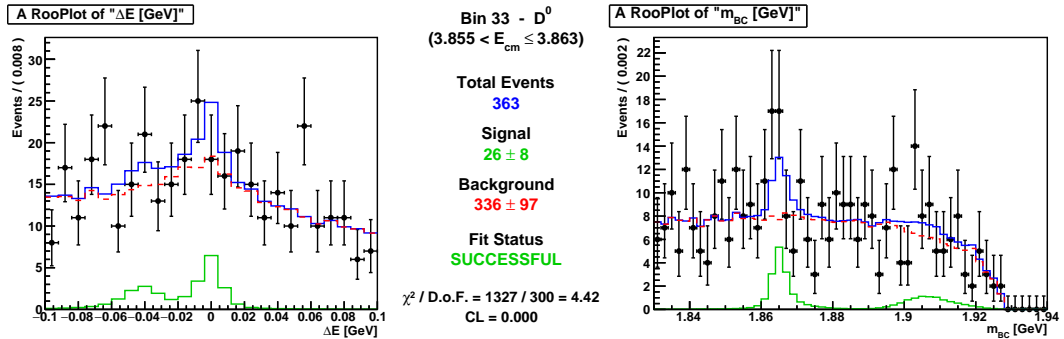
Signal Fit - D^0 Bin 33

Figure B.9: Signal Fitting Plots for D^0 Bins 30 - 33.
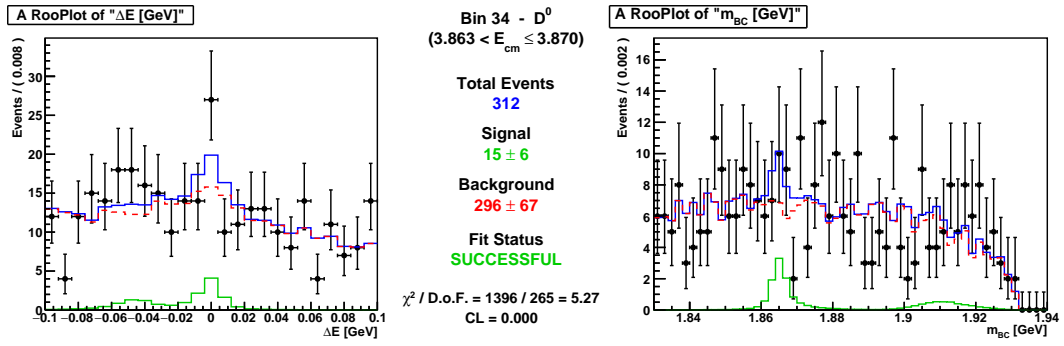
Signal Fit - D^0 Bin 34

Figure B.10: Signal Fitting Plots for D^0 Bin 34.

Appendix C

D^+ Signal Fits

Signal Fit - D^+ Bin 3
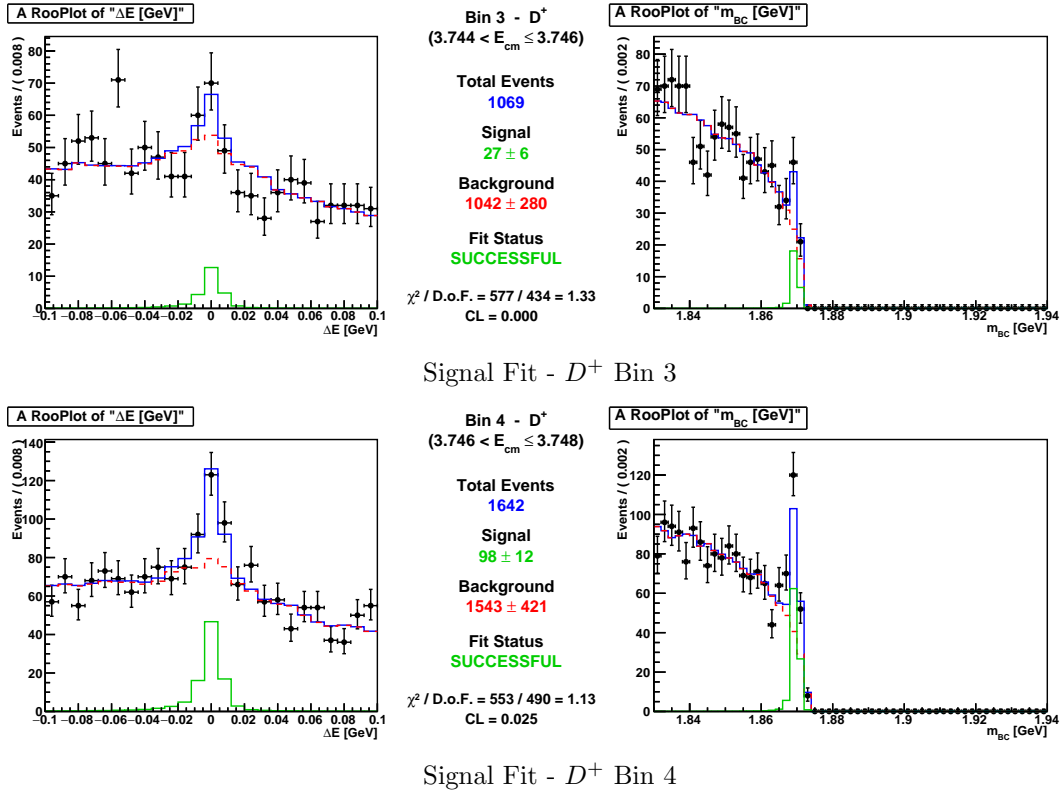
Signal Fit - D^+ Bin 4

Figure C.1: Signal Fitting Plots for D^+ Bins 3 - 4.
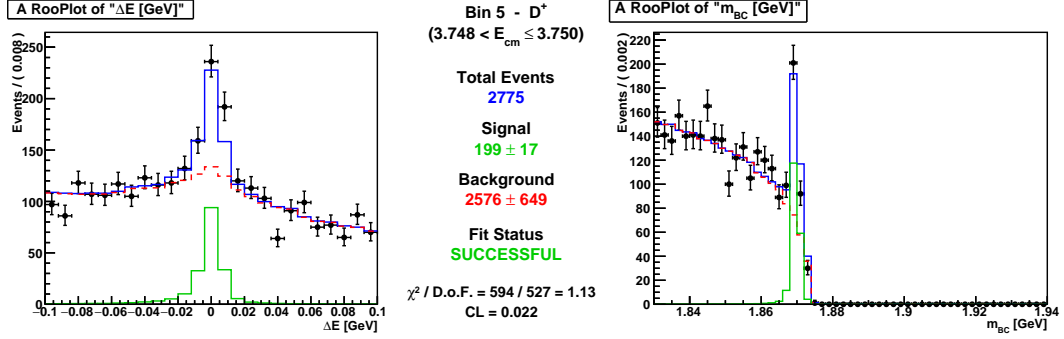
Signal Fit - D^+ Bin 5
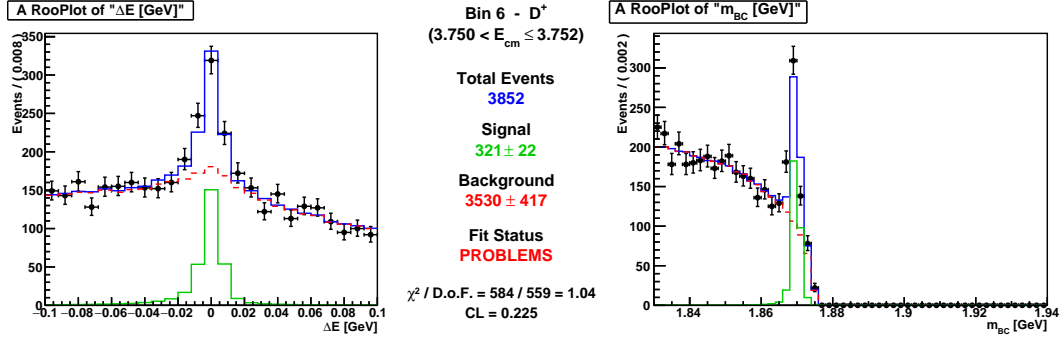
Signal Fit - D^+ Bin 6
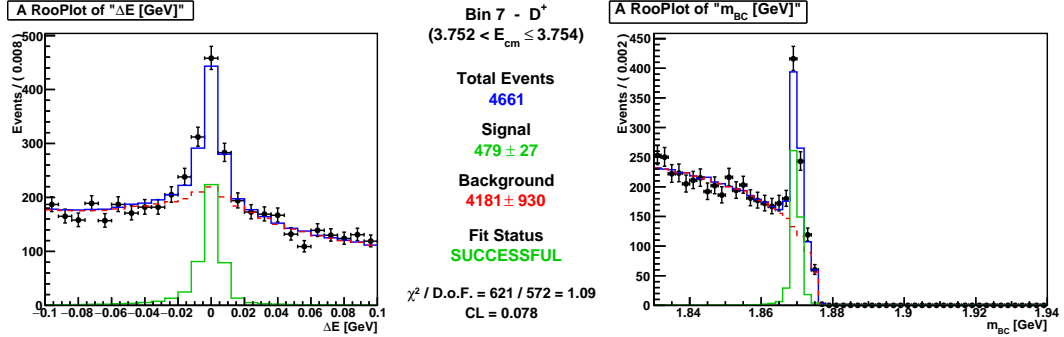
Signal Fit - D^+ Bin 7
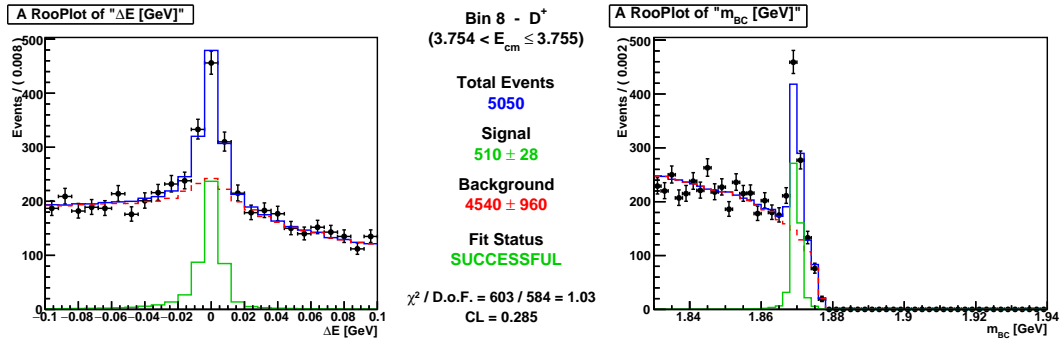
Signal Fit - D^+ Bin 8
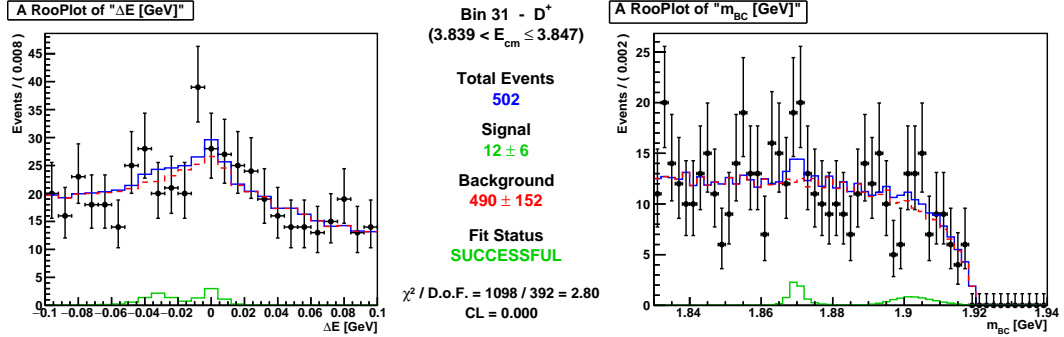
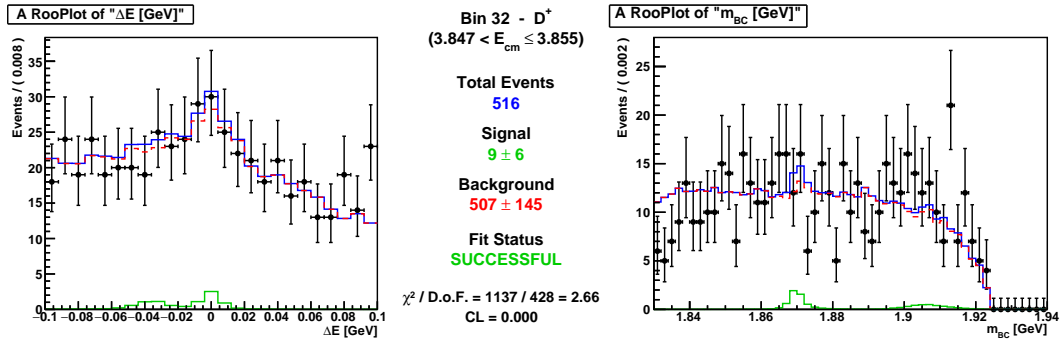Figure C.2: Signal Fitting Plots for D^+ Bins 5 - 8.
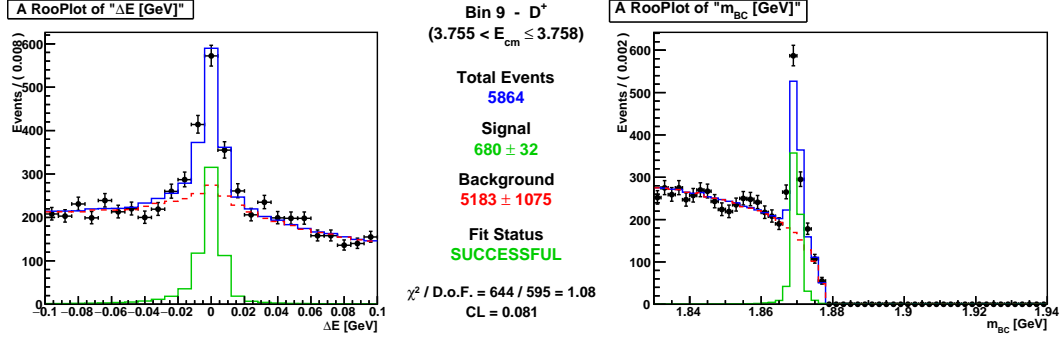
Signal Fit - D^+ Bin 9
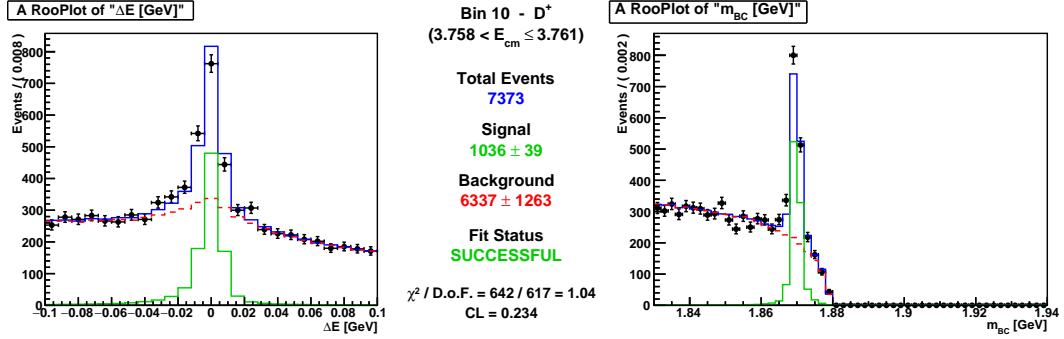
Signal Fit - D^+ Bin 10
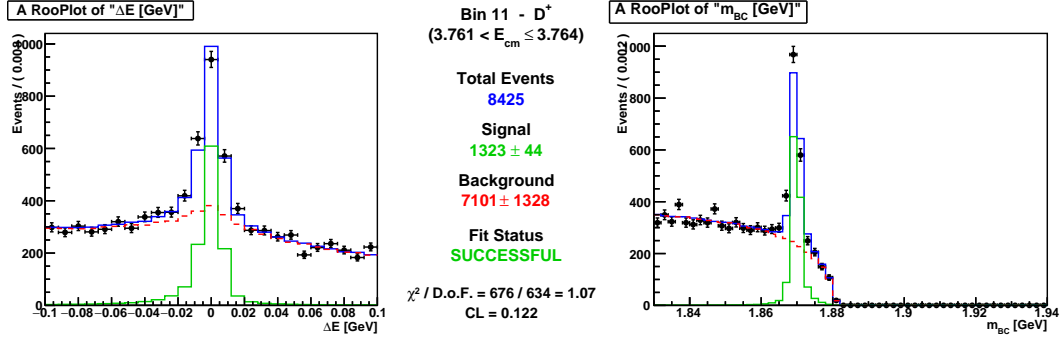
Signal Fit - D^+ Bin 11
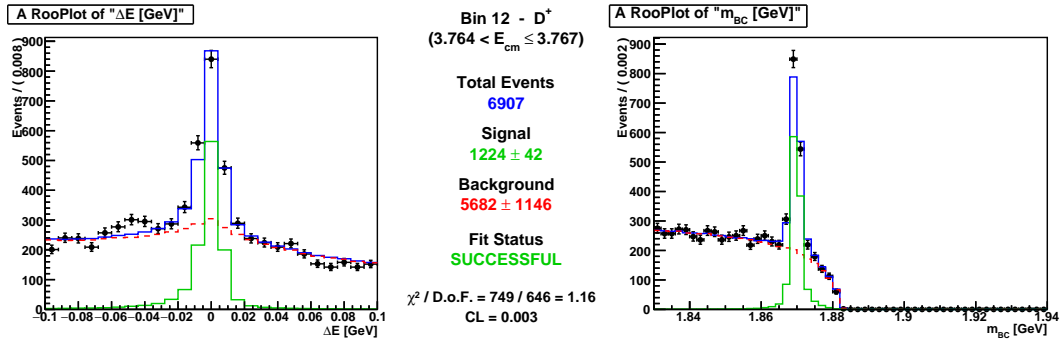
Signal Fit - D^+ Bin 12

Figure C.3: Signal Fitting Plots for D^+ Bins 6 - 12.
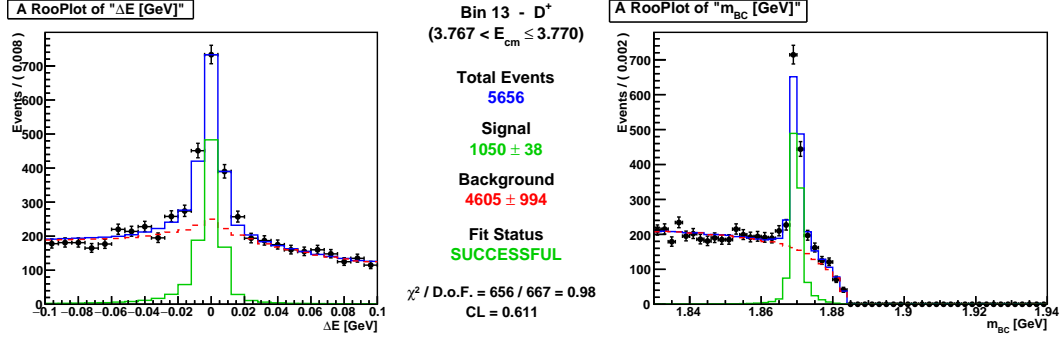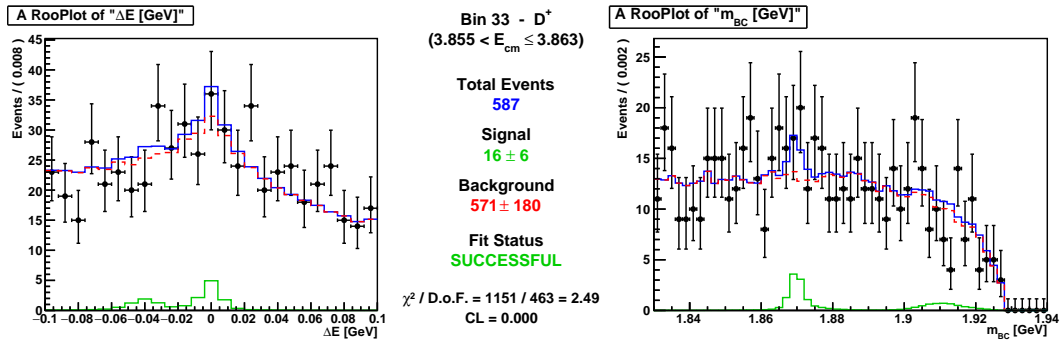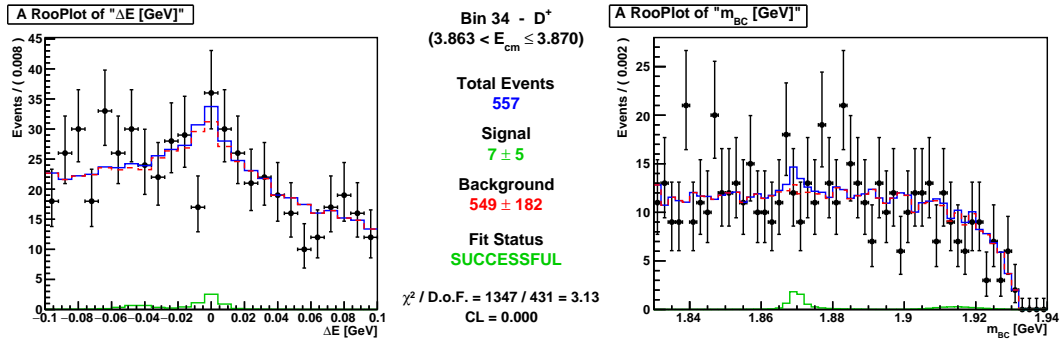
Signal Fit - D^+ Bin 13
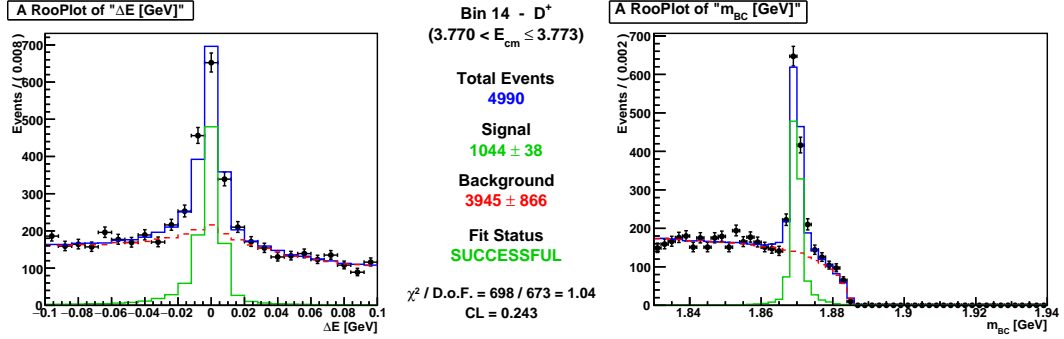
Signal Fit - D^+ Bin 14
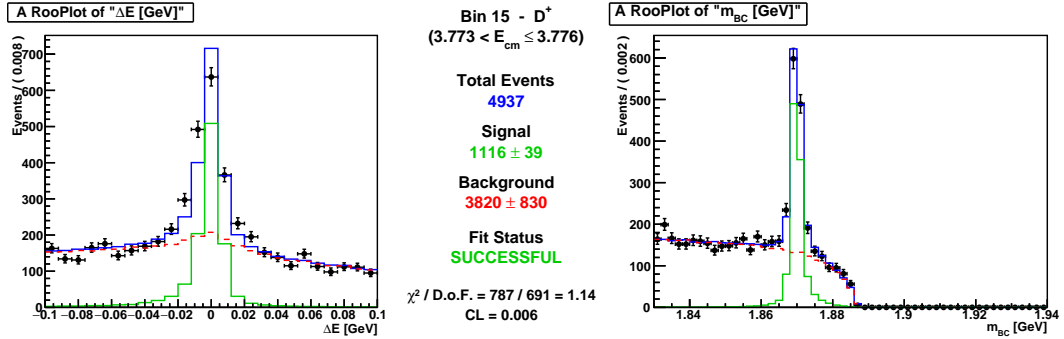
Signal Fit - D^+ Bin 15
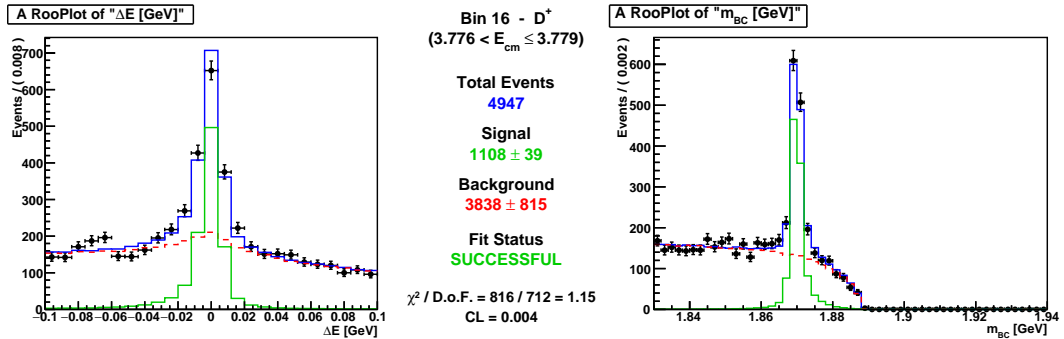
Signal Fit - D^+ Bin 16

Figure C.4: Signal Fitting Plots for D^+ Bins 13 - 16.
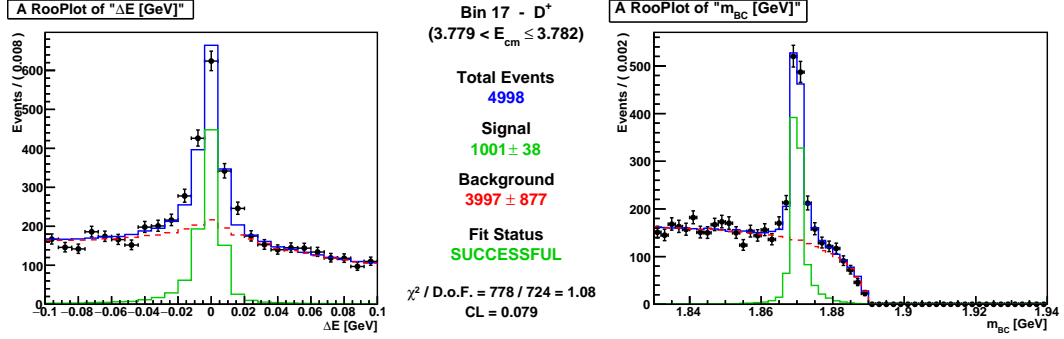
Signal Fit - D^+ Bin 17
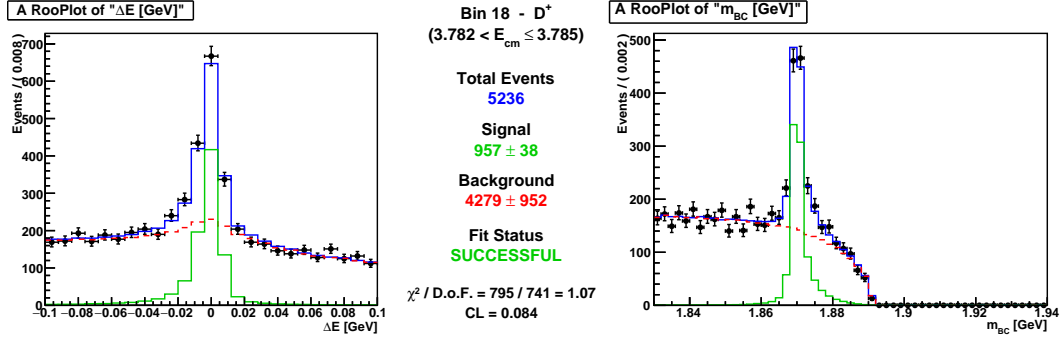
Signal Fit - D^+ Bin 18
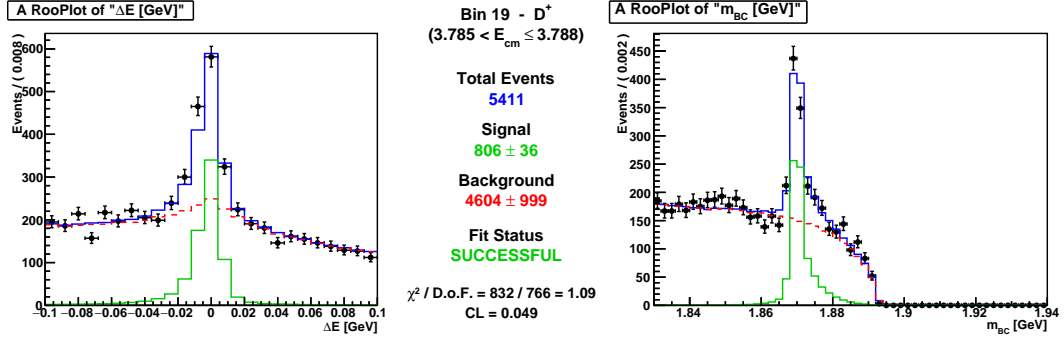
Signal Fit - D^+ Bin 19
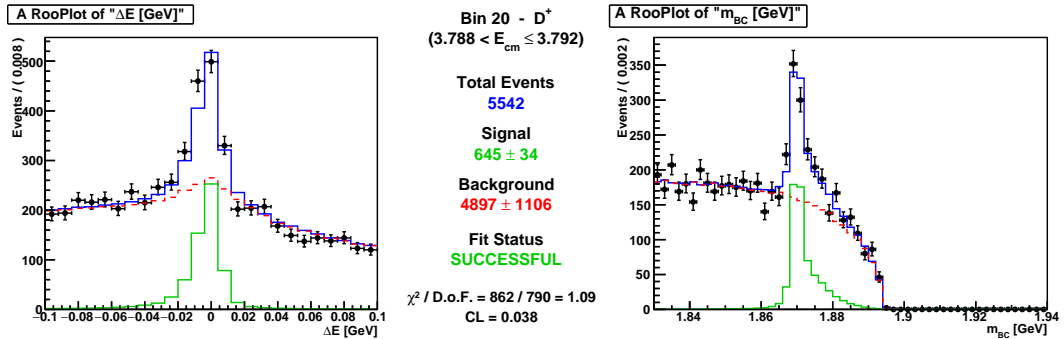
Signal Fit - D^+ Bin 20

Figure C.5: Signal Fitting Plots for D^+ Bins 17 - 20.
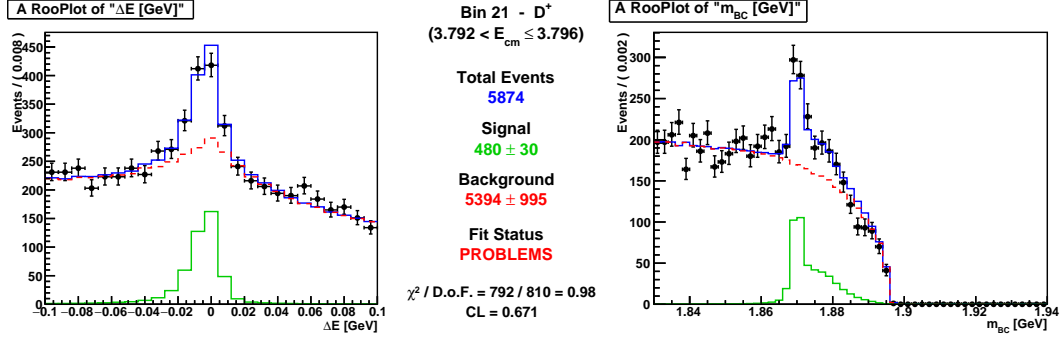
Signal Fit - D^+ Bin 21

Signal Fit - D^+ Bin 22
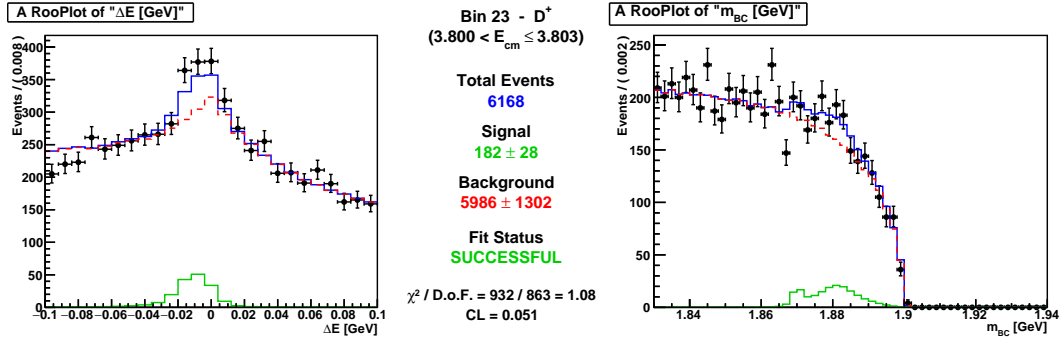
Signal Fit - D^+ Bin 23
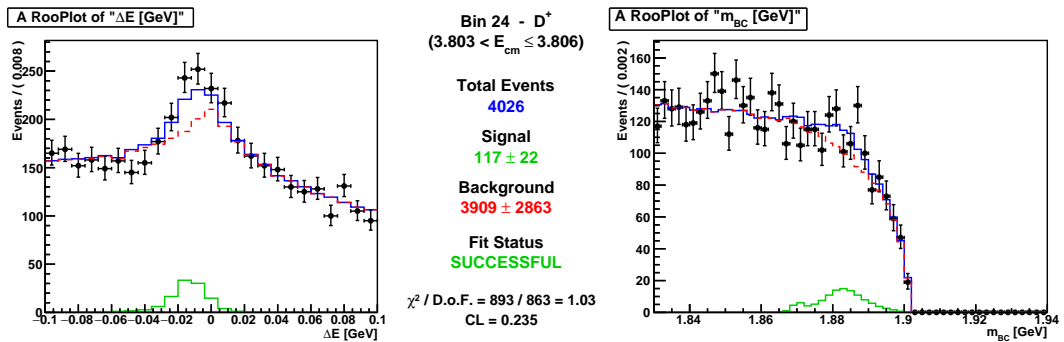
Signal Fit - D^+ Bin 24

Figure C.6: Signal Fitting Plots for D^+ Bins 21 - 24.
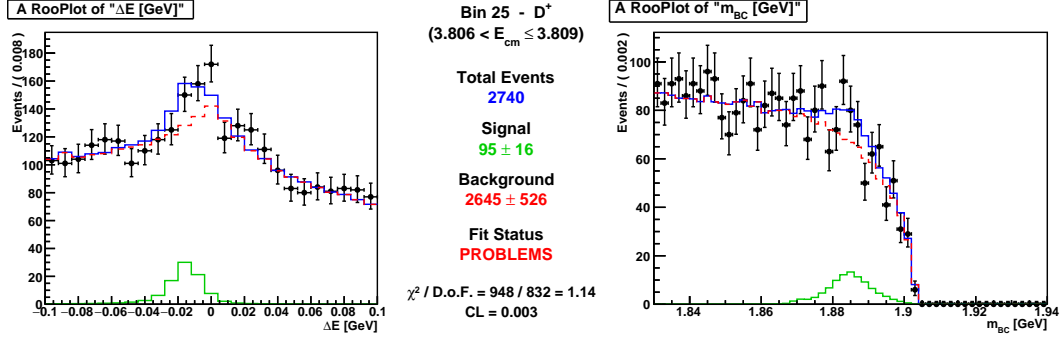
Signal Fit - D^+ Bin 25
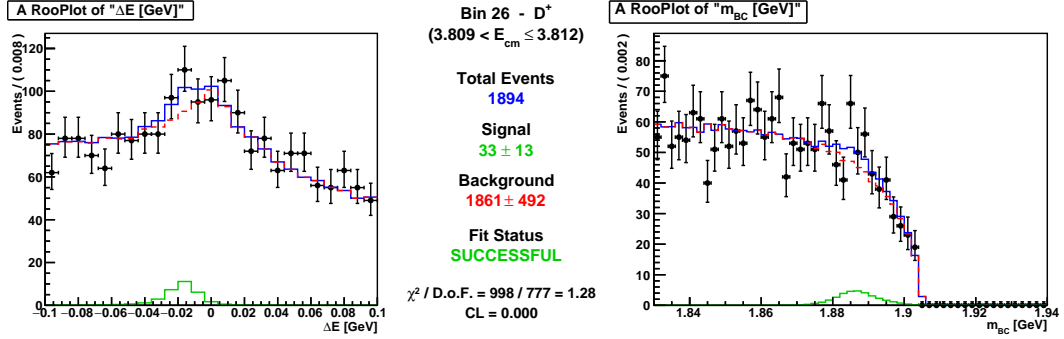
Signal Fit - D^+ Bin 26
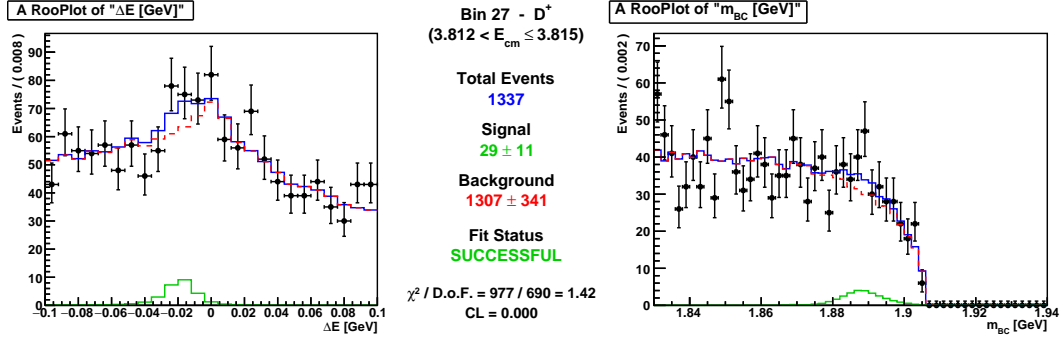
Signal Fit - D^+ Bin 27
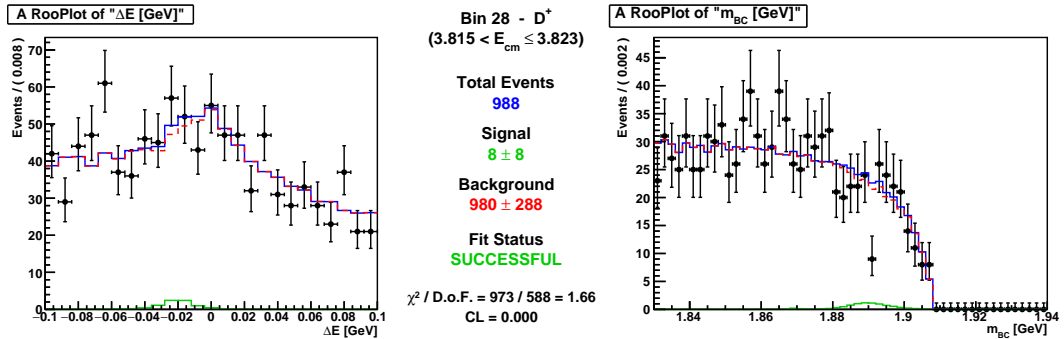
Signal Fit - D^+ Bin 28

Figure C.7: Signal Fitting Plots for D^+ Bins 25 - 28.
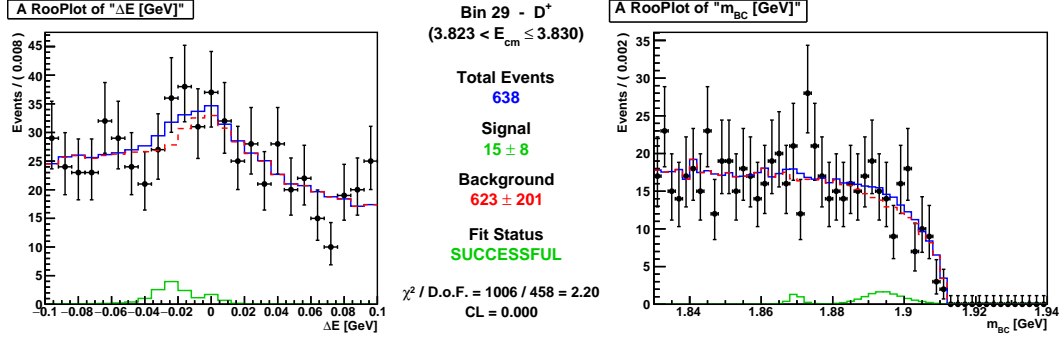
Signal Fit - D^+ Bin 29
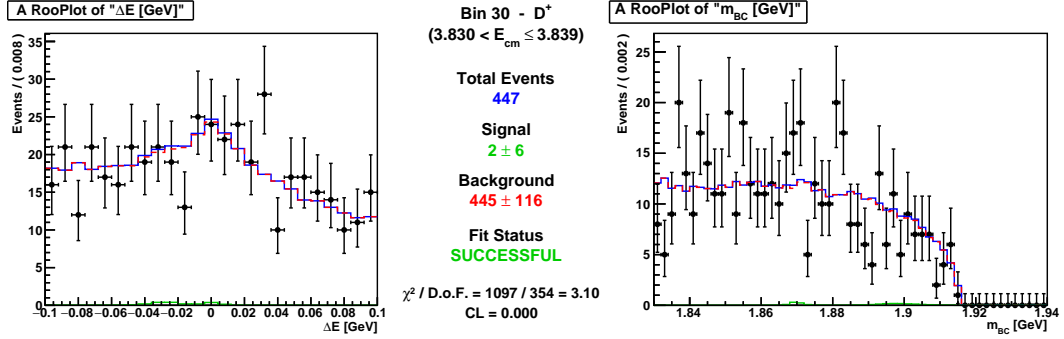
Signal Fit - D^+ Bin 30

Signal Fit - D^+ Bin 31

Signal Fit - D^+ Bin 32

Figure C.8: Signal Fitting Plots for D^+ Bins 29 - 32.

Signal Fit - D^+ Bin 33

Signal Fit - D^+ Bin 34

Figure C.9: Signal Fitting Plots for D^+ Bins 33 - 34.